LOCALIZATION OF ATOMIC EXCITATION BEYOND THE DIFFRACTION LIMIT USING ELECTROMAGNETICALLY INDUCED TRANSPARENCY

by

Jared Anthony Miles

A dissertation submitted in partial fulfillment of
the requirements for the degree of

Doctor of Philosophy

(Physics)

at the

UNIVERSITY OF WISCONSIN–MADISON

2015

Date of final oral examination: August 12, 2015

The dissertation is approved by the following members of the Final Oral Committee:

Deniz D. Yavuz, Professor, Physics

James E. Lawler, Professor, Physics

Mark Saffman, Professor, Physics

Thad G. Walker, Professor, Physics

John C. Wright, Professor, Chemistry

Dedicated to My Family and Friends

ACKNOWLEDGMENTS

I want to first thank my advisor Deniz Yavuz. He has been an amazing advisor and friend over my past 5 years in Madison. He always took time to answer my questions and listen to my ideas. He was aways very enthusiastic about all of his projects, which made working for him very fun. Thank you to my committee: Deniz, James Lawler, Mark Saffman, Thad Walker, and John Wright.

I want to thank all of the past and current members of the Yavuz group who helped me over the years: Josh Weber, Daniel Sikes, Zach Simmons, Nick Brewer, David Gold, Diptaranjan Das, Josh Karpel, Zach Buckholtz, Eli Mueller, and Ben Lemberger. Thanks to Josh Weber, Nick, and David for reading parts of my thesis and giving me good feedback. I like the current members of the group, and I think the group will be left in good hands after I leave.

I would like to thank the staff of the physics department. Specifically, I would like to thank Ann Austin, Renee Lefkow, and Aimee Lefkow. They make a lot of things run smoothly for the department.

I want to thank all of my friends I made in Madison over the past five years. I want to make sure to thank Ian Wisher, Matt Ebert, Mike Wood, James Duff and Alyssa Brewer, as well as the members in the Yavuz group I mentioned earlier. They made grad school much more enjoyable.

Finally, I want to thank my family for their support. My parents, Mauri and Susan Miles, were very supportive and were always interested in what I was doing. My sister Kelsey moved to Madison for her PhD in chemistry, and it was nice having her live in Madison.

TABLE OF CONTENTS

Page

Page

Abstract

Localization of Atomic Excitation Beyond the Diffraction Limit Using Electromagnetically Induced Transparency

Jared A. Miles

Under the supervision of Professor Deniz D. Yavuz

At the University of Wisconsin - Madison

This thesis focuses on an experimental technique to excite atoms in areas smaller than the diffraction limit. Normal optical techniques cannot accurately excite atoms in such a small region, and accurate excitation would be a useful tool for atomic quantum computers for addressing individual qubits. We use ultra cold atoms trapped in a dipole trap to excite atoms in regions smaller than the diffraction limit. The atoms are excited via the dark state of EIT, which coherently transfers the atoms through a two photon process. The localization is performed using a standing wave which utilizes the non-linear intensity dependence of EIT. The excitation is fast ($\sim$ 100 ns laser pluses) and we detect excitation of atoms in regions as small as $\lambda/13$.

Atoms are transferred are in regions smaller than the diffraction limit, where normal imaging techniques cannot be used. We use two EIT pulses to perform an autocorrelation technique to measure the transfer region. A small delay is imposed between the pulses, where the standing wave is moved.

Chapter 1

Introduction

Imaging is a fundamental problem in the physical sciences. The size that light can be resolved at or focused to is limited by its wavelength. This limit has been well known for over a century since it was discovered by Ernst Abbe in the 19^{th} century. He discovered that the smallest light can be focused to or resolved is $\sim \lambda/2$. This not only limits the ability to image objects below this limit, but also effects the ability to accurately address atoms below this limiit. This work will focus on trying to address atoms in regions that are smaller than the diffraction limit. The term "address" means exciting the atom into a different energy level.

One way to address the atoms is with a focused laser beam at an appropriate frequency that can excite the atom. If the atoms are spaced on the order of $\lambda/2$, a focused laser could not selectively address the atoms. We attempt to get around this issue by using an optical technique called electromagnetically induced transparency (EIT)[1, 2, 3, 4]. EIT uses two lasers that will transfer atoms between two ground state levels depending non-linearly on the intensity ratio of the two lasers. To spatially adjust this intensity difference over small distances ($\lambda/2$) we use one of the lasers in a standing wave configuration and the other with a constant intensity. This spatially varies the intensity with a period of $\lambda/2$, greatly changing the intensity ratio over a few nanometers. We take advantage of this non-linearity to transfer atoms in regions that are smaller than $\lambda/2$.

Due to the diffraction limit, normal imaging techniques will not be able to determine where the atoms are spatially being transferred if the atoms are in regions smaller than $\lambda/2$. For example, if atoms are accurately excited to a different ground state within a 10 nm region, and those atoms were imaged with light of wavelength 1.0 μm, the resulting imaging would show a 500 nm region. Because of this, we developed an auto-correlation technique to measure an effect of the EIT transfer

in very small regions. By seeing a correlated effect of the EIT transfer, we can infer the size of the region the atoms are transferred. We show experimental results that imply atoms are being addressed in regions that are 60 nm wide, a factor of 13 less than the wavelength of light used to produce the EIT.

An important aspect of our localization technique is the coherent nature of EIT. We want the initial energy level and excited level to be coherent with one another, which is an important concept for quantum computing experiments. By coherently exciting the atoms, it would be possible to put a single atom in a superposition of two states in an area that is below the diffraction limit. This is an advantage over other localization techniques where there is very little coherence between the two states.

Chapter 1 discusses the theory of electromagnetically induced transparency (EIT). We discuss the three energy level system and the two lasers that produce EIT. The atomic system can be numerically simulated by solving the density matrix.

Chapter 2 shows experimental evidence of EIT in our atomic system. A laser passes through atoms where is would normally be absorbed. Under EIT conditions this laser passes through the atoms without being absorbed.

Chapter 3 gives a detailed explanation of the standing wave experiment using EIT to address atoms in regions smaller than the diffraction limit. The auto correlation method we experimentally use is discussed in detail here.

Chapter 4 shows our first evidence of the localization experiment using the D_2 atomic line in ^{87}Rb. atoms are localized in regions of $\sim$100 nm, a factor of 8 less than the wavelength of light used in EIT.

Chapter 5 discusses improvements we made to the experimental set up to get better localization data. A number of factors were improved in an attempt to see better localization results. We changed our experiment to work in the D_1 atomic line in ^{87}Rb.

Chapter 6 presents the localization data using the D_1 atomic line. We address atoms in regions that are 13 times smaller than the wavelength of light used to address them.

Chapter 7 describes a technique to suppress Doppler broadening. This chapter is independent from the other chapters. We go through theoretical simulations explaining how a high power laser that stark shift the energy levels of the atom can compensate for Doppler broadening.

Chapter 2

Localization

Many experiments use focused lasers to interact with and image atoms and molecules. Several experimental set ups for quantum computing, using either trapped ions or trapped neutral atoms, use focused lasers to address individual qubits [5, 6, 7, 8, 9]. The amount of light that can be focused is limited by the Abbe diffraction limit, where the smallest spot size that light of wavelength λ can be focused to has a radius of

$$r = \frac{\lambda}{2n \sin\theta} \tag{2.1}$$

where $n \sin\theta$ is the numerical aperture of the focusing lens. At small spot sizes the light resembles an Airy disk due to diffraction. Fig. 2 is a plot of the Airy disk for 780 nm light assuming an index of refraction of 1. We use the same wavelength for work in the next chapter. Some systems can pass the light through a higher index of refraction, to achieve a numerical aperture of up to 1.5. For instance, microscopes may have a layer of oil between the object and imaging lens to increase the index of refraction. This could focus light down to $\lambda/3$ at most. This type of set up would use a microscope lens with a very short focal length positioned very close to the object. A lot of work has been done in an attempt to image even smaller areas that would otherwise be diffraction limited. In 1994 Stefan Hell and Jan Wichmann developed an important imaging technique called stimulated emission depletion (STED) microscopy to overcome this limit [10]. This important technique was recognized with the Nobel prize in chemistry, emphasizing the importance of sub diffraction imaging.

Another technique to get around the diffraction limit uses spatial varying energy shifts developed by Thomas and colleagues [11, 12]. By using a spatially varying laser intensity to cause a

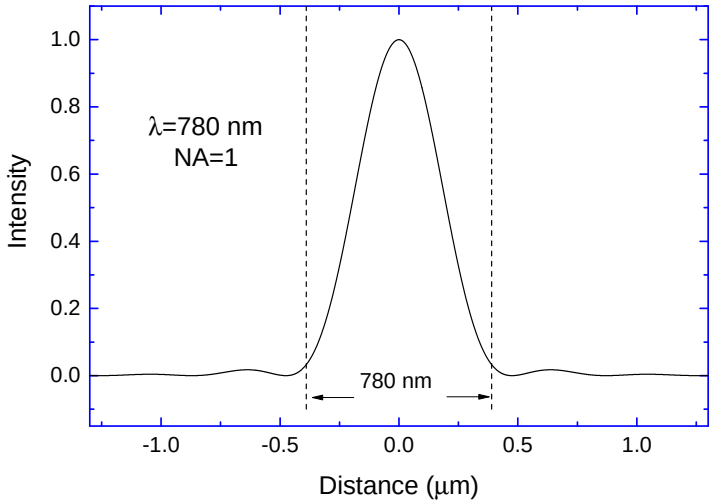

Figure 2.1 Due to diffraction, tightly focused laser light creates an Airy disk.

stark effect in the atoms, the atomic resonance changes with position. This optimizes the excitation of the atoms depending on the spatial intensity dependence of the stark shifting laser.

Previous work has been done in the near field to overcome this limit [13, 14]. The diffraction limit assumes the far field, where the light propagates as expected. It ignores near field evanescent waves which quickly decay to zero in the far field. For the output of a fiber, the near field is very close to the fiber tip ($<< \lambda$) and can usually be ignored. By placing a sample very close to the probe, researchers can accurately address atoms at the 10 nm level. This method is called near field scanning optical microscopy (NSOM) and is often used with nano-particles.

All of these techniques rely on the nonlinear response of the atom or molecule to the incident light. For quantum computing the interaction between qubits must be kept coherent. Processes like spontaneous emission destroy the coherence between the atoms and needs to be suppressed. The dark state of EIT discussed in chapter 3 coherently transfers atoms between energy levels, providing an advantage over other localization techniques. We will use the dark-state of EIT to localize the excitation of atoms to areas smaller than the diffraction limit.

Chapter 3

EIT Simulations

3.1 Introduction

The work in this thesis focuses on using the dark state of electromagnetically induced transparency (EIT) to create atomic excitation localization. EIT is a laser induced process that can cause a laser to become transparent to an otherwise absorbing medium. The dark state is a specific wave function of the atomic system that allows for this transparency. First I will discuss the idea of steady state EIT. Later I will go through issues for non steady state parameters (*i.e.* when the lasers pulses are short and the atomic system does not have time to reach steady state).

3.2 EIT Diagram

Fig. 3.1 is the energy level scheme that we use to demonstrate EIT. The set up is a lambda EIT configuration using two lower energy levels that are not coupled together (*i.e.* any atoms in one of these energy levels cannot decay into the other level). The third energy level is an excited state that is coupled to both lower states through a decay rate Γ_e. Atoms in the excited state can decay into either lower state. In general, EIT can be observed in any 3 level atomic system where 2 levels are not well coupled to each compared to the third level. For the lambda scheme we work in, EIT can occur if each of the lower two levels are coupled to the excited by separate laser beams. Fig. 3.1 shows the energy diagram and laser used for the lambda EIT configuration. The frequency of each laser is very important in relation to each energy level. The laser that couples the lowest state $|1\rangle$ to the highest state $|e\rangle$ is called the "probe" beam and has frequency ω_p. The laser that couples

$|2\rangle$ to $|e\rangle$ is called the "coupling" beam with frequency ω_c. In Fig. 3.1, the lasers are denoted with their Rabi frequencies Ω_p and Ω_c for each transition which are defined as

$$\Omega_p = \mu_{1e}\vec{E}_p/\hbar \tag{3.1}$$

$$\Omega_c = \mu_{2e}\vec{E}_c/\hbar \tag{3.2}$$

where $\vec{E}_c$ and $\vec{E}_p$ are the electric fields of the coupling and probe laser respectively. μ_{ij} is the transition dipole moment for each transition, and is dependent on the two energy levels. In this 3 level example, we assume that μ_{12} is zero, and therefore no interaction occurs between those two states. Fig. 3.1 also shows the detunings of the lasers relative to $|e\rangle$ which are defined as

$$\Delta\omega_p = (\omega_e - \omega_1) - \omega_p \tag{3.3}$$

$$\delta\omega = (\omega_2 - \omega_1) - (\omega_p - \omega_c) \tag{3.4}$$

EIT is observed when $\delta\omega$=0, when the frequency difference of the probe and coupling laser is equal to the separation of the two levels $|1\rangle$ and $|2\rangle$. The populations of the three levels are affected by the strength of each laser and the two detunings $\delta\omega$ and $\Delta\omega_p$.

3.3 Absorption

For the atomic system in Fig. 3.1, we first consider the case when Ω_c=0, that is, there is no coupling beam, and all of the atoms are initially in the lower state $|1\rangle$. For this case, we assume Ω_p is very small, and it assumed that almost all of the population remains in the lower state while the probe beam is on. The interaction of the probe laser between the lower level $|1\rangle$ and the excited state $|e\rangle$ will produce absorption, and can be calculated from the susceptibility between the two levels. The absorption plot is shown in Fig. 3.2 and its width is determined by the decay rate of the excited state, Γ_e. For These simulations Γ_e=6 MHz. The absorption is plotted against $\Delta\omega_p$. As expected, when the laser is on resonance ($\Delta\omega_p$=0) the most absorption occurs.

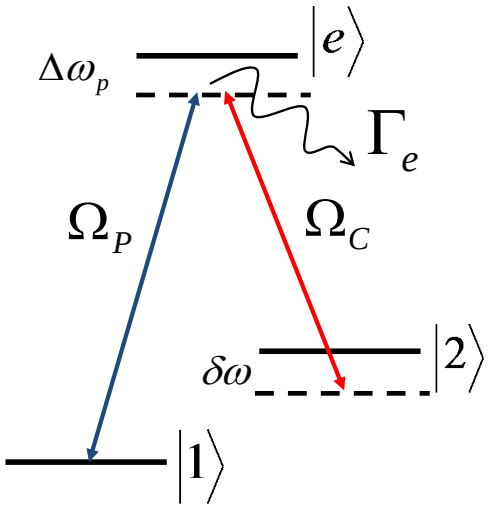

Figure 3.1 EIT lambda set up. Two lasers couple the lower levels through an excited state. The excited state decays into the lower two levels through a decay rate Γ_e. The two lower states have negligible decay rates.

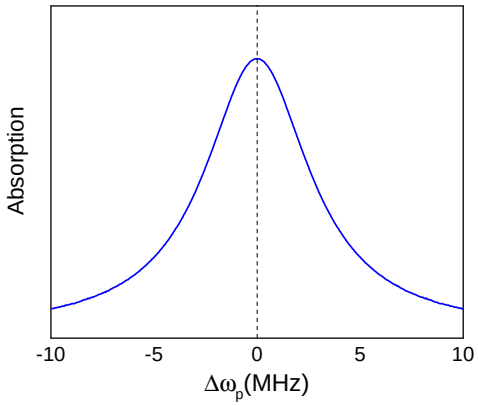

Figure 3.2 Absorption of probe beam with no coupling beam. The most absorption occurs when probe beam is on resonance with the excited state, when $\Delta\omega_p$=0.

3.4 EIT and Dark State

Now we consider the case when both laser are on. When Ω_c is turned on before Ω_p, the two energy levels with no atoms are ”dressed” before Ω_p is turned on. This laser is much stronger than

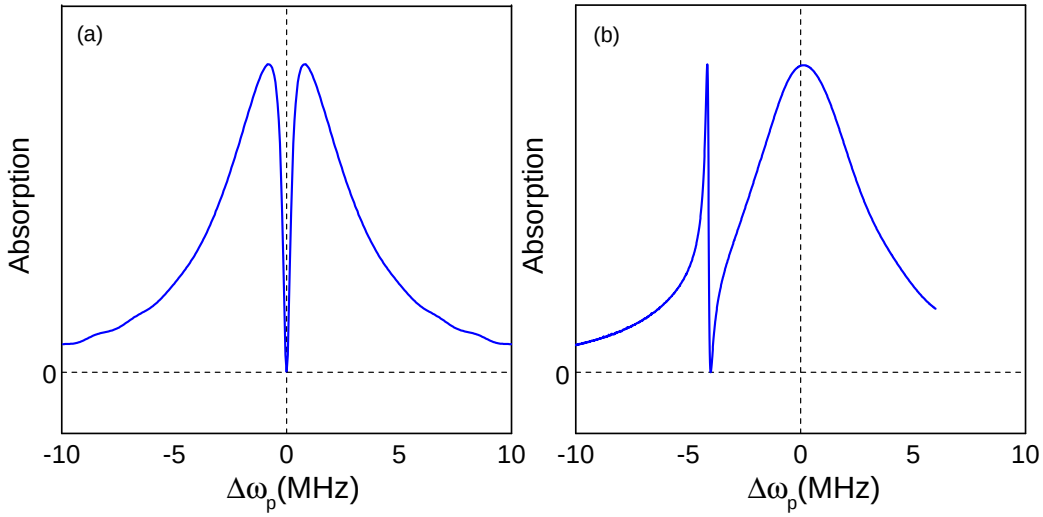

Figure 3.3 Fig. a shows transparency of the probe beam due to the presence of the coupling beam. In this case, transparency occurs when both $\Delta\omega_p$=0 and $\delta\omega$=0. Fig. b is the transparency of the probe beam assuming the coupling beam is 4 MHz off resonance with the excited state ($\omega_e - \omega_2 - \omega_c$=-4 MHz). Transparency still occurs at $\delta\omega$=0, but for this case $\Delta\omega_p$=- 4MHz. Transparency still occurs, but not on resonance with the excited state.

probe beam, but since no atoms are in either level, the atoms remain in $|1\rangle$, and the populations are unaffected. If we use the same weak probe beam used in Fig. 3.2, and monitor its absorption over $\Delta\omega_p$, we get the plot in Fig. 3.3 (a), which shows transmission (no absorption) where we would normally see peak absorption. For this plot $\Delta\omega_p$ =$\delta\omega$, and when both equal 0 the probe laser becomes transparent, and does not get absorbed. This is very different from the absorption plot in Fig. 3.2. We can also consider the case when both beams are off resonant from the excited state. Fig. 3.3 plots the aborption of the probe beam when the coupling laser is 4 MHz detuned from the excited state ($\omega_e - \omega_2 - \omega_c$=-4 MHz). When $\Delta\omega_p$=0 MHz, $\delta\omega$ equals -4 MHz, and transparency does not occur. For this case, $\Delta\omega_p$=-4 MHz corresponds to the correct probe frequency to make $\delta\omega$=0, and therefore produce transparency. This shows that the lasers to not have to be resonant with the excited state to produce transparency. As long as the condition $\delta\omega$=0 is met, transparency can occur.

Since the absorption goes to 0, there is no interaction between $|1\rangle$ and $|e\rangle$ and atoms cannot be moved to the excited state. The excited level is "dark" at this point, and all population stays in the lowet level $|1\rangle$. The previous simulations were created with Ω_c much higher than Ω_p, (Ω_c=Ω_p x100), but smaller ratios would also show zero absorption for $\delta\omega$=0. Analytically solving the 3 level atomic system assuming steady state and that $\delta\omega$=0 gives us the dark state

$$|\Psi_{dark}\rangle = \frac{\Omega_c^*}{\sqrt{\Omega_c^2 + \Omega_p^2}} |1\rangle - \frac{\Omega_p^*}{\sqrt{\Omega_c^2 + \Omega_p^2}} |2\rangle \tag{3.5}$$

where the coefficients for each lower level are determine by the Rabi frequencies. There is no contribution from the excited state, and therefore no population in $|e\rangle$. For the cases plotted earlier with $\Omega_c >> \Omega_p$ the vast majority of population remains in the initial state $|1\rangle$. The population in $|1\rangle$ and $|2\rangle$ will change depending on both Rabi frequencies. The dark state equation has a prominent role in other processes as well. It is a key process in coherent population trapping (CPT) and stimulated Raman adiabatic passage (STIRAP) [15]. Using different techniques with EIT one can obtain slow light [16, 17, 18, 19, 20] , stopped light [21, 22, 23, 24, 25, 26] and even construct large optical nonlinearities effective at the single-photon level [27, 28, 29, 30, 31, 32].

3.5 Density Matrix Simulations

Equation 3.5 assumes the system has had enough time to reach steady state. It also assume that Ω_c is turned on before Ω_p, assuring that the unpopulated levels are "dressed" before applying Ω_p. This is assuming a steady state solution, but in the lab we do the experiment with finite pulses to quickly move population between the two lower levels. We numerically simulate the populations of all 3 levels by solving the density matrix of the system. The density matrix is defined as

$$\rho_{\alpha\beta} = \langle\alpha| \rho |\beta\rangle \tag{3.6}$$

where ρ is the density operator

$$\rho = \sum_{\alpha} P_\alpha |\Psi_\alpha\rangle \langle\Psi_\alpha| \tag{3.7}$$

The atomic system can be in a combination of states, Ψ_α, each with probability P_α. One of these possible states is the dark state in equation 3.5. The diagonal terms of the density matrix are the populations of the three atomic levels, while the off diagonal elements are the coherences. For the simulations we want to know how these terms vary in time. The time derivative of ρ is

$$\frac{\partial \rho}{\partial t} = \sum_\alpha P_\alpha \left(\frac{\partial \left|\Psi_\alpha\right\rangle}{\partial t} \left\langle \Psi_\alpha \right| + \left|\Psi_\alpha\right\rangle \frac{\partial \left\langle \Psi_\alpha \right|}{\partial t} \right) \tag{3.8}$$

By substituting in the time dependent Schrodinger equation from equation 3.9, we can get the Liouville equation for the density matrix in equation 3.10.

$$\frac{\partial \Psi}{\partial t} = -\frac{i}{\hbar} H \left|\Psi\right\rangle \tag{3.9}$$

$$\frac{\partial \rho}{\partial t} = -\frac{i}{\hbar}[H, \rho] \tag{3.10}$$

H is the Hamiltonian and [H,ρ] is the commutator. For the 3 levels in Fig. 3.1, along with the coupling and probe beam, the Hamiltonian H, is

$$H = \begin{bmatrix} \hbar\omega_1 & 0 & -\mu_{1e} \cdot \vec{E_p}(t) \\ 0 & \hbar\omega_2 & -\mu_{2e} \cdot \vec{E_c} \\ -\mu_{e1} \cdot \vec{E_p^*} & -\mu_{e2} \cdot \vec{E_c^*} & \hbar\omega_e \end{bmatrix} \tag{3.11}$$

Where $\hbar\omega$ are the energies of each level and the off diagonal terms come from the interaction Hamiltonian $-\mu \cdot E$. We use this Hamiltonian to solve the density matrix in equation 3.10. The decay rate from the excited state has been neglected, but can be added with an additional term to equation 3.10 [2]. Adding this changes the density matrix to

$$\frac{\partial \rho}{\partial t} = -\frac{i}{\hbar}[H, \rho] - \frac{1}{2}\{\Gamma, \rho\} \tag{3.12}$$

where $\{\Gamma, \rho\}$=$\Gamma\rho$+$\rho\Gamma$.

To make this computation easier we perform a unitary transformation on the Hamiltonian to transform our original Hamiltonian into something easier to work with numerically. After performing this transformation, we use the rotating wave approximation to ignore fast oscillating

terms. A detailed explanation is in appendix A. This will get rid of all terms that oscillate and therefore makes the numerically integration much easier. By getting rid of the oscillating terms the transformed Hamiltonian $H_{transform}$ is

$$H_{transform} = \hbar \begin{bmatrix} 0 & 0 & -\frac{\mu_{1e}E_p}{2\hbar} \\ 0 & \delta\omega & -\frac{\mu_{2e}E_c}{2\hbar} \\ -\frac{\mu_{e1}E_p^*}{2\hbar} & -\frac{\mu_{e2}E_c^*}{2\hbar} & \Delta\omega_p \end{bmatrix} \tag{3.13}$$

where E_c and E_p are the magnitudes of the electric fields from the coupling and probe lasers. The matrix elements are calculated depending on the coupling between the levels, and is different for different atoms and transitions. A more detailed calculation showing the step between equations 3.11 and 3.13 is listed in the appendix. This Hamiltonian makes numerically calculating the Liouville equation much easier. We solve equation 3.10 using a 4th order Runge-Kutta method.

3.6 Numerical Simulations

The diagonal terms of the density matrix (ρ_{11}, ρ_{22}, and ρ_{ee}) are the populations of the three levels, while the off diagonal terms are the coherences between states. These coherences relate to the absorption and index of refraction for those transitions. The coherences produced by EIT have been used to modify the index of refraction in vapor cells [33, 34]. In the experimental measurements I will discuss later in this thesis, we will measure the populations of one the energy levels, but not the coherences. Therefore, the simulations are needed for determining the coherences between levels. We can test to make sure our numerical simulations gives us what is analytically expected by equation 3.5 by using laser pulses that are on for a sufficient time to put the system into steady state.

In the actual experiment, the values Ω_c and Ω_p will vary in time, depending on how fast we turn on and off the laser pulses. Ending the pulse before sufficient time for the dark state to be established can produce a density matrix that is very different than the analytical result. The interaction time to put the 3 level system into the dark state depends on a number of factors,

including the decay rate of the excited level, the strength of the dipole moments, and the detuning values of $\delta\omega$ and $\Delta\omega_p$. As an example, I will show the density matrix solution with three different sets of parameters. These plots are for typical parameters used in our experiments that will be discussed later. Ω_p and Ω_c are set equal to each other, at about 100 MHz, $\delta\omega$=0, and $\Delta\omega_p$=30 MHz. As long as the two photon detuning is zero the system will approach the dark state. We also assume that all of the population begins in level $|1\rangle$. Given a long enough interaction time between the atoms and the lasers, the density matrix should become

$$\rho = \begin{bmatrix} 0.5 & -0.5 & 0 \\ -0.5 & 0.5 & 0 \\ 0 & 0 & 0 \end{bmatrix}$$

where there are no off diagonal elements that couple to the un populated excited state $|e\rangle$, and the population is evenly distributed among the lower two levels. Another important feature is that ρ_{12} and ρ_{21} are non-zero, indicating that the two states are coherently coupled together by the lasers. Figure 3.4 is numerically simulated data with the same experimental parameters but with very short pulses in comparison to the Rabi frequencies, approximately 100 ns. When the beam is turned off there remains a small population in the excited state along with a population distribution between the $|1\rangle$ and $|2\rangle$ levels that is different than expected. The dotted line is figure 3.4 is where I recorded the density matrix, and is when both beams fall to half of their original value. The density matrix in this case is

$$\rho = \begin{bmatrix} 0.19 & -0.16 - 0.26i & -0.01 + 0.04i \\ -0.16 + 0.26i & 0.80 & -0.08 - 0.05i \\ -0.01 - 0.04i & -0.08 + 0.05i & 0.01 \end{bmatrix}$$

and shows large off diagonal terms. Our goal is to be in the dark state by the end of the laser pulses, so atoms are in the lower two states are coherently coupled to one another. Since there is there is no decay between the two lower states, the coherence will stay the same value even when the pulses are turned off. It is important for us to simulate the experiment to obtain the off diagonal elements for the system.

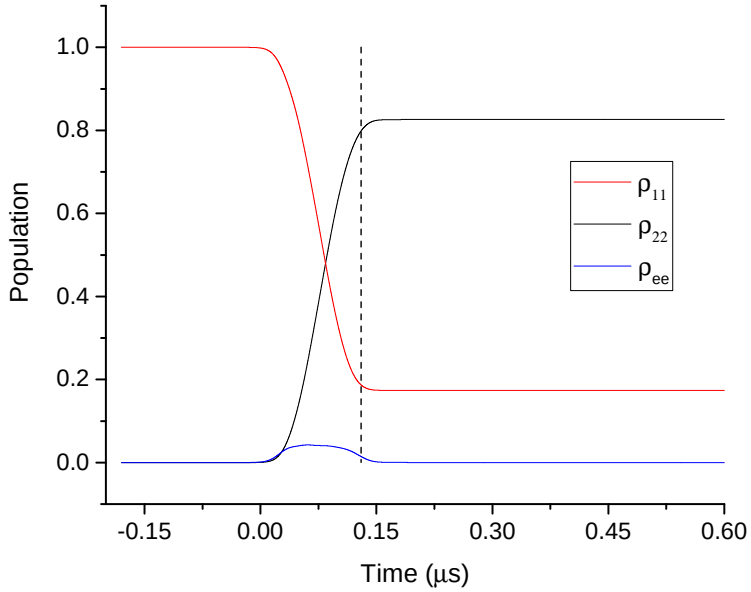

Figure 3.4 Population of the three EIT levels for 100 ns pulses with $\Omega_c = \Omega_p \sim$100 MHz. Pulses begin at Time=0 ns. The dotted line is where we record the density matrix, when Ω_p and Ω_c are at half their original value.

Experimentally we only measure the population of one of the lower states after the EIT pulses take place. The decay rate used in the above simulation was 6 MHz, which gives the excited state a lifetime of 26 ns. Shortly after the pulses are turned off, excited state population decays into one of the lower tow energy levels, and the excited state population goes to zero. We measure the atoms milliseconds after the pulses are turned off. This means that there is no good way for us to measure the excited level during the pulses. This is another reason why the simulations are important in determining what happens when the pulses are very short.

Although the two density matrices above are different, we want to put a single number to how different they really are. This will make comparisons to other simulated density matrices much easier. We compare the two matrices using the following equation

$$Tr\left(\sqrt{\sqrt{\sigma}\rho\sqrt{\sigma}}\right) \tag{3.14}$$

Where ρ is the density matrix of the dark state, σ is the simulated density matrix and Tr is the matrix trace operation. The equation is used by other groups to measure the overlap between two quantum states and is called the fidelity between the two states [9]. The fidelity can range from 0 to 1 depending on how well the states overlap with a higher value indicating better overlap. For the above two density matrices the overlap is 0.81, indicating some similarities but still far from the ideal state. By increasing the pulse length we make sure we are further in the dark state. In figure 3.5 a., the populations are plotted for 3 μs long lasers pulses. The fidelity for this case is 0.9996.

Although it is close to the analytical equation, there are small off diagonal terms that indicate the system is not perfectly in the dark state. The overlap here is .9996, and the population in $|e\rangle$ is negligible. The populations of $|1\rangle$ and $|2\rangle$ oscillate while approaching the dark state over the 3 μs pulses. These oscillations depend on both Rabi frequencies, as well as the detuning from the excited state. By doubling the Rabi frequency (experimentally quadrupling the laser intensity) we approach the dark state much faster, as shown in figure 3.5 c. The fidelity now becomes much higher at 0.99999995 (seven 9's). High fidelities are crucial for quantum computing experiments, and with higher intensity pulses the dark state can be reached quickly.

3.7 Conclusion

EIT is a very large portion of the work in this thesis. We use it transfer atoms between normally un-coupled levels using two laser pulses called the probe and coupling laser. Under certain conditions the atomic system will only exist in these two lower levels, and there will be no population in the excited levels. This state is known as the dark state. Two important factors are needed to make sure the experiment is in the dark state. The detuning $\delta\omega$ must be equal to zero, and the laser must be given enough time to reach the dark state. The simulations are important in determining the coherences between levels, since we did not experimentally measured these values.

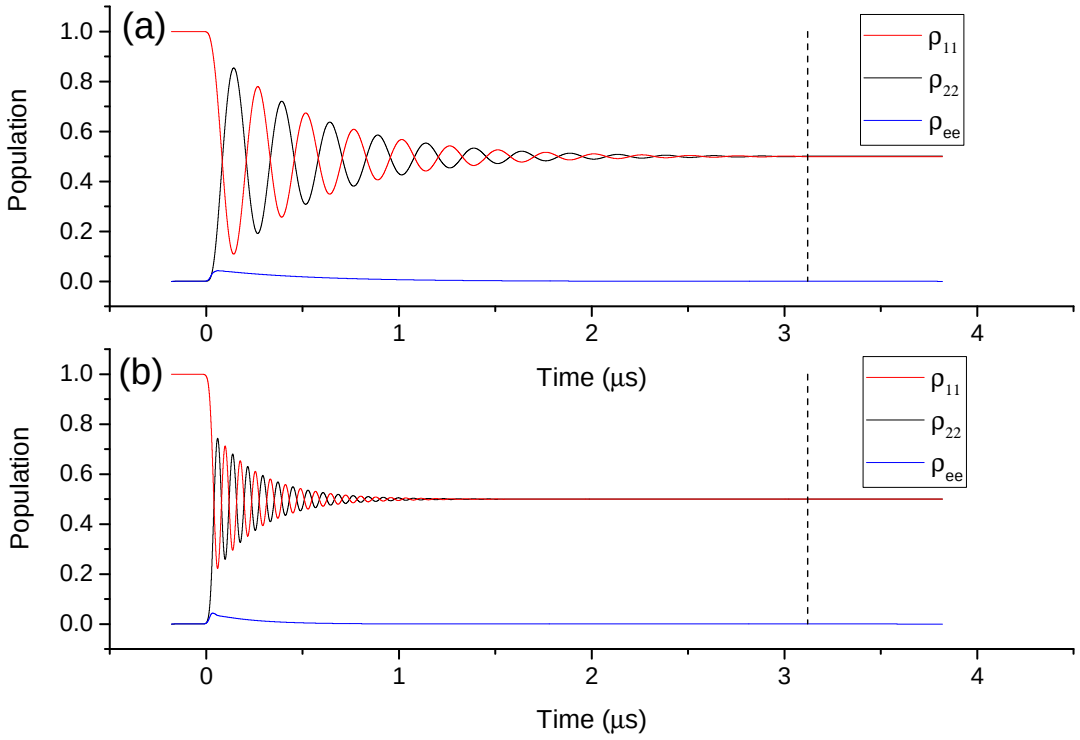

Figure 3.5 Population of the three EIT levels for 3 μs pulses. Pulses begin at Time=0 ns. The dotted line is where we record the density matrix, when Ω_p and Ω_c are at half their max value. Plot b used Rabi frequencies that were twice the values of those used in a.

Chapter 4

EIT Experiment With FORT Atoms

4.1 Introduction

Previously, our group demonstrated EIT in a magneto optical trap (MOT) using the dark state [35]. We further that work by doing the experiment with atoms in a far off resonance trap (FORT). This should be advantageous because a) the large non-uniform magnetic fields needed for a MOT are not needed for a FORT b) much lower atomic temperatures can be reached with FORT atoms and c) the large size of the MOT can cause non uniform densities. In this chapter I will discuss the experimental set up of our FORT and an EIT measurement that show transparency in a narrow window of 0.5 MHz. This demonstrates the dark state which will be later used for our localization experiment.

4.2 Experimental Set Up for MOT

A MOT must first be created before trapping atoms in a FORT. Here I will briefly describe our experimental set up for the MOT we use to trap our FORT atoms. The magneto optical trap is a very established experiment that can cool atoms to the Doppler limit (150 μK for ^{87}Rb) [36]. Using a combination of Doppler cooling and magnetic fields, atoms originally at room temperature can be trapped within an ultra-high vacuum chamber. This section will discuss the MOT apparatus used for all of the EIT experiments in this thesis. ^{87}Rb atoms are Doppler cooled in a 14 port stainless steel vacuum chamber using 3 retro reflected beams. The chamber is pumped down to 10^{-9} Torr using an ion pump. Rather than using a rubidium getter, the rubidium vapor originates from a few grams of Rb put in a valve controlled flange attached to the chamber. The magnetic

field coils that create the anti-Helmholtz field each have 250 turns each with a current of 2 A. There are also 3 pairs of shim coils that attempt to negate the Earth's magnetic field to produce a magnetic field of zero at the center of the chamber. The beams are 2 cm in diameter and have approximately 50 mW of power in the two directions perpendicular to the anti-Helmholtz coils and 25 mW in the parallel z direction. Figure 4.1 shows the chamber and three MOT beams. Figure 4.2 is a picture of the chamber.

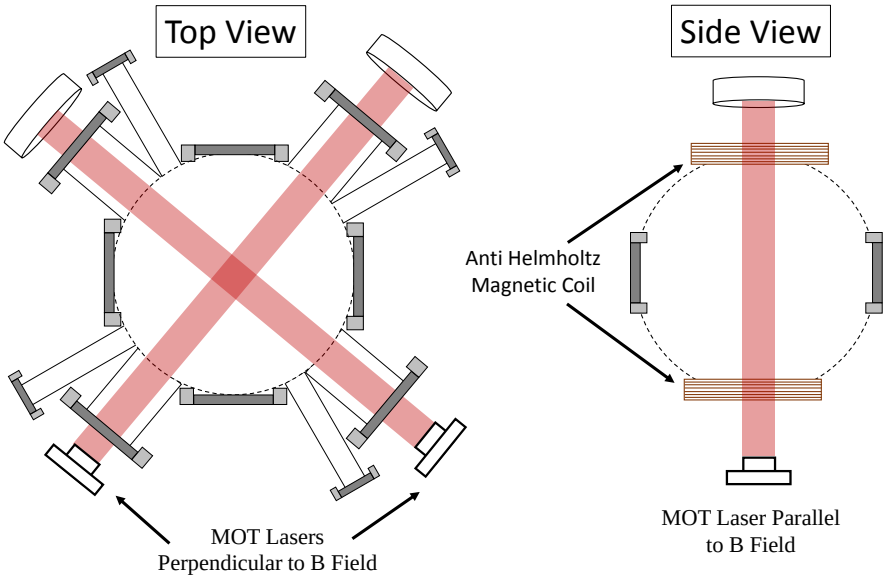

Figure 4.1 Diagram of the MOT beams for our chamber. The lasers perpendicular to the magnetic field from the anti Helmholtz configuration requires half the power as the other two beams. The repump beam is overlapped with one of the perpendicular beams and has about 3 mW of power. Each beam has a $1/e^2$ radius of 2 cm.

All 3 MOT beams originate from a 2 W Eagleyard tapered amplifier (TA) seeded by an external cavity diode laser (ECDL) at 780 nm. The ECDL is commonly used in atomic physics and uses frequency selective feedback to narrow the diode's laser linewidth [37]. We cool the atoms and do the EIT experiment using the D_2 line of ^{87}Rb. Appendix B discusses the relevant transitions in ^{87}Rb that are used in this thesis. Fig. 4.3 is the energy diagram of the hyperfine levels for D_2 line. The cooling transition for the MOT is the F=2 to F′=3 transition (F′ indicates that the F level is in the excited state of the transition). The laser is locked to a cross over transition between the F′=1

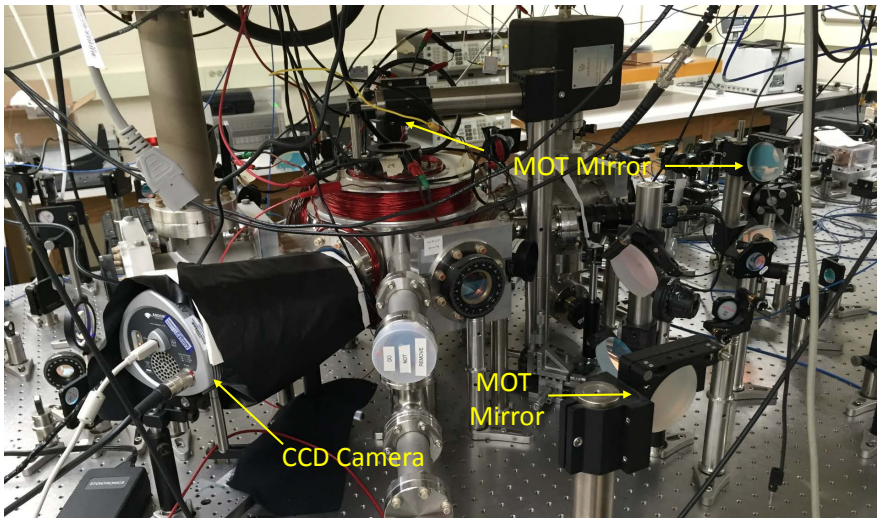

Figure 4.2 Photo of the vacuum chamber we used for all of the experiments discussed in this thesis.

and F′=3 energy levels, 212 MHz away from the cooling transition, using a saturated absorption spectroscopy technique [38]. An acoustic optical modulator (AOM) shifts the 780 nm laser to the correct frequency, 22 MHz detuned from the cooling transition. A separate ECDL is used as repumper and is on resonance with the $F = 1$ to $F = 2'$ transition. The repumper optically pumps any atom in the $F = 1$ state back to $F = 2$ so they can be cooled by the MOT beams. The repumper is overlapped with one of the MOT beams and has approximately 3 mW of power. The resulting MOT atoms have a temperature of 150 μK and has a total number of close to 1 billion. Figure 4.1 shows the set up of the 3 MOT beams in relation to the anti-Helmholtz coils. Fig. 4.5 shows the beam path of the MOT before entering the vacuum chamber. An assortment of polarizing beam cubes and wave plates split the output of the tapered amplifier into the 3 MOT beams.

4.3 Experimental Set Up for FORT

A far off resonant trap (FORT) can produce a potential well large enough to trap atoms for seconds without the use of an external magnetic field. This method of atom trapping is widely used to achieve temperatures below 1 μK and densities up to 10^{14} atoms/cm^3 [40]. Barrett et al

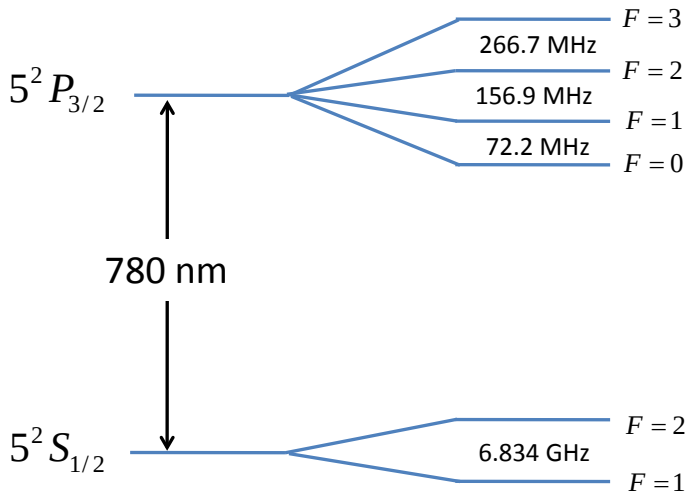

Figure 4.3 Energy diagram for the D_2 line in ^{87}Rb. Also displayed are the frequency splittings of the hyperfine energy levels. The $5^2S_{1/2}$ energy level is the ground state while $5^2P_{1/2}$ is one of several possible excited states in ^{87}Rb. The energy differences are taken from Steck's work [39]

used a FORT to produce an all optical Bose-Einstein condensate, reducing the temperature of the atoms to 375 nK [41].

The FORT uses the stark shift to create a spatially varying potential along a focused laser beam. A laser that is off resonant to the a level transition will shift the two energy levels depending on the laser intensity (I) and detuning (Δ). For a two level system where the laser is detuned to the red of the transition, the upper and lower energy levels are shifted by an amount +ΔE and -ΔE respectively. This energy difference ΔE is defined as

$$\Delta E = \frac{3\pi c^2 \Gamma}{2\omega_o^3 \Delta} I \tag{4.1}$$

where ω_o is the on resonance transition frequency and Γ is the decay rate of the upper state. By using a focused laser, the intensity, and therefore the energy shift, varies spatially across the laser. This creates a potential well with the lowest energy at the center of the focused laser. The magnitude of this energy shift will determine what temperature of atoms are trapped. Since this energy shift is small, on the order of 1 mK, atoms have to be first cooled by a MOT before being

trapped by the FORT. We trap the atoms in the FORT laser by overlapping it with the MOT atoms. Fig. 4.4 is a cartoon depicting the energy shift and creation of the potential well.

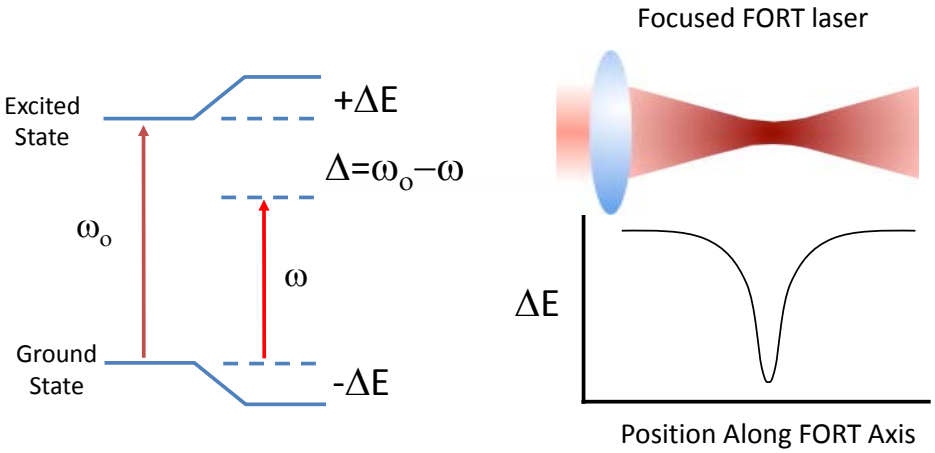

Figure 4.4 A red detuned laser causes both energy levels to shift by an amount ΔE. A focused laser produces a potential well, with the largest energy shift at the focus of the laser. Atoms become trapped at the center of the laser.

The FORT is created from a 1 W tapered amplifier (TA) at 850 nm. The output of the tapered amplifier is not completely Gaussian and does not focus well to a small spot size. We pass the output of the amplifier through a single mode polarization maintaining fiber to produce a TEM00 mode. The fiber output is focused to a $1/e^2$ radius of 10 μm with a 2 inch doublet achromat with a focal length of 20 cm. We lose power through the fiber and an optical isolator protecting the amplifier from any back reflections. The final power is approximately 150 mW.

To optimize the number of atoms in the trap, we further cool the MOT atoms through polarization gradient cooling. We detune the MOT beams further to 13Γ and reduce the MOT beam power by a factor of two while the FORT beam is on. We call this setting the cool MOT, our CMOT. A larger detuning lowers the temperature of the MOT due to the frictional forces from the polarization between a MOT beam and its reflection. This is a common technique used to cool atoms below the Doppler limit [42, 43, 44]. Colder atoms result in more atoms being captured by the dipole trap laser. We can change the detuning with a separate AOM that is also aligned to the

TA. The TA can be seeded by either laser with both beams traveling through a 50/50 beam splitter. We can't use the same AOM because the frequency difference is so large that the beam becomes unaligned to the TA. Figure 4.5 shows the double AOM set up that allows us to switch between MOT and CMOT settings.

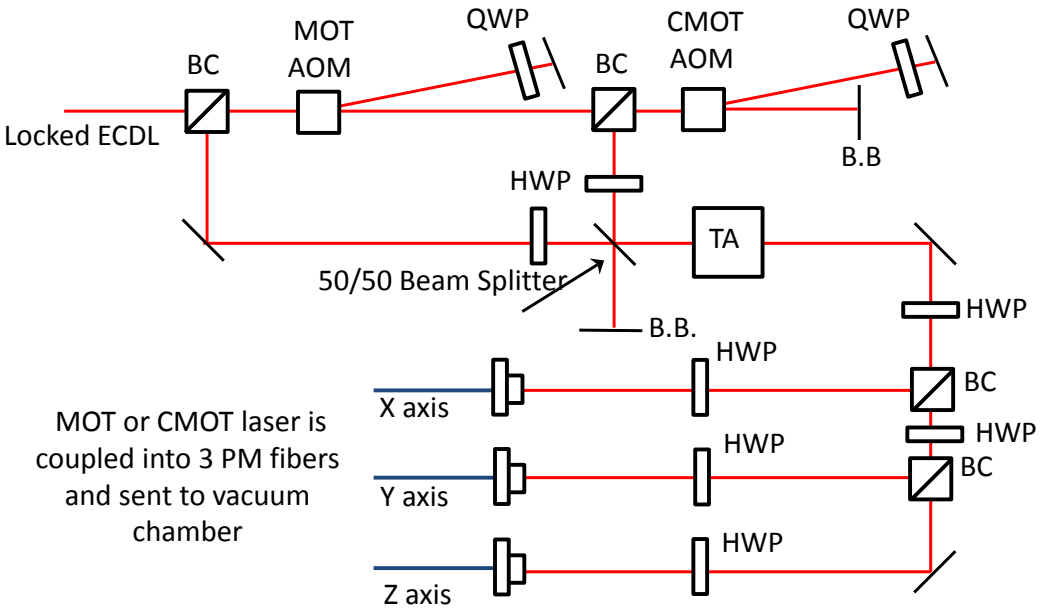

Figure 4.5 Experimental set up of MOT and CMOT lasers. One saturated absorption locked ECDL can be shifted either 190 MHz or 134 MHz to seed the 2 W Eagleyard tapered amplifier (TA). Both AOM's are used in a double passed configuration with quarter wave plates (QWP) to allow the second pass to travel through the beam cube (BC). Both beams are aligned together through a 50/50 beam splitter before entering the TA. Half wave plates (HWP) are used to optimize fiber alignment and seeding to the TA. Beam blocks (B.B.) are used to block unused laser light. The MOT beams provide 50 mW in the x and y axis and 25 mW in the z direction. In the CMOT setting, all beams provide about half their original power.

Reducing the repumper power during FORT loading also increases the number of loaded atoms [45]. We greatly reduce the power from 3 mW to about 20 μW. The MOT detuning and reduction in repump power is done for 40 ms, while the FORT beam is overlapped with the MOT. These detunings and powers were optimized to maximum the number of atoms loaded into the FORT.

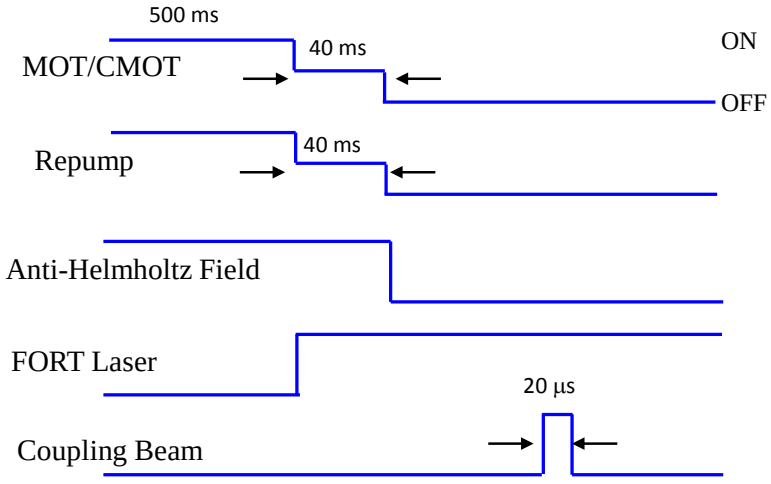

Figure 4.6 Timings of for the EIT absorption experiment. The MOT and repumper are adjusted for 40 ms to optimize loading into the FORT. During this time both beam are on but there powers are reduced. After trapping, the coupling beam (Ω_c) is turned on to pump all FORT atoms into the F=1 state. Atoms are trapped with only the FORT laser on and no magnetic field.

With the FORT beam left on, we turn off the MOT beams, repumper, and magnetic field, letting atoms not trapped in the FORT disperse throughout the chamber. Fig. 4.6 represents the timings needed to optimally trap atoms in the FORT. When the atoms are initially trapped in the FORT they can be in either the F=1 or F=2 ground state level. We optically pump atoms into the F=1 state by turning on an additional laser called the "coupling" beam. This laser will be discussed more in the next section. The atoms are distributed over the 3 m_F levels in F=1 through optical pumping. We perform a time of flight (TOF) measurement on the FORT atoms and record a temperature of $\sim$ 50 μK. We detect the atoms through a fluorescence measurement and trap approximately 100,000 atoms. Appendix C discusses the fluorescence measurement in more detail. We study the dark state of EIT with these resulting cold FORT atoms.

The FORT atoms should result in better EIT data for multiple reasons. Unlike the MOT atoms, no magnetic field is needed to keep the atoms trapped. We turn off the magnetic field 50 ms before the EIT experiment to assure that no remnants of the anti-Helmholtz magnetic field remain. The

size of the FORT is also an advantage. With the MOT atoms covering a large area, 2-3 mm, the density may not be uniform, affecting the absorption of the probe beam, and therefore affecting the EIT results. Also, the imaging of the atoms will be more uniform with the FORT atoms. Fig. 4.7 has pictures of both the MOT and FORT atoms taken with the CCD camera. The FORT covers a much smaller area, reducing inconsistencies with the atomic density.

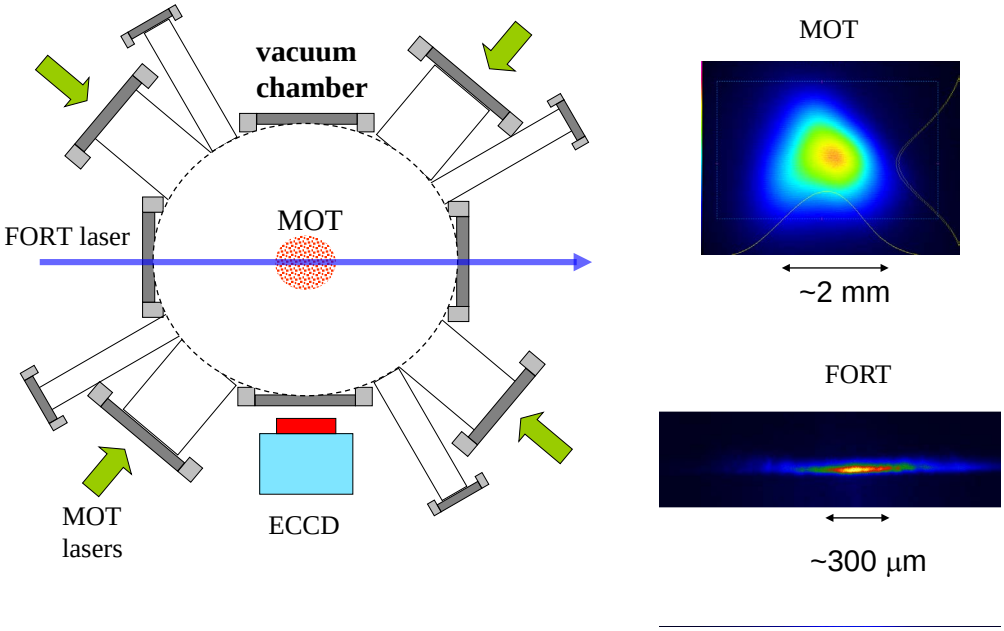

Figure 4.7 Picture of MOT and FORT taken with ECCD camera.

4.4 EIT Lasers

We perform the EIT experiment using the $F = 1 \rightarrow F' = 2$ and $F = 2 \rightarrow F' = 2$ transitions in the D_2 line as shown in figure 4.8. The probe laser is denoted by Ω_p and the coupling laser is Ω_c. The transitions are separated by 6.834 GHz, and we use one seed laser locked to the $F = 2 \rightarrow F' = 3$ transition to create both the coupling and probe beams. By using the same seed laser for each beam, we are assured that the coherence between the two beams remains consistent. We use a similar set up used by Unks *et al.* [46]. The seed laser is a 90 mW Thorlabs single mode diode laser in an ECDL configuration. We lock the laser to the desired transition with a saturated

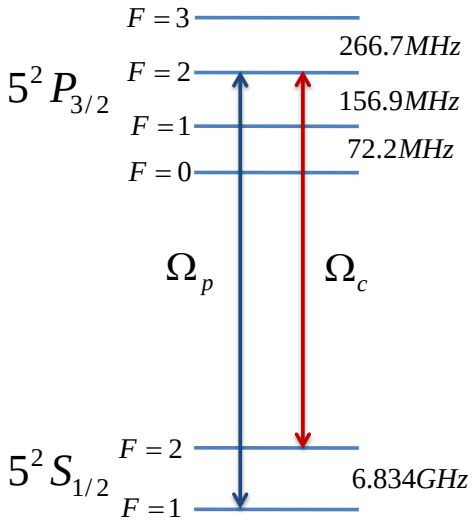

Figure 4.8 D_2 ^{87}Rb energy level diagram. Ω_c and Ω_p are the coupling and probe beams used to create the dark state. The two lasers are separated by 6.834 GHz, the frequency difference between the two ground states.

absorption set up resulting in a linewidth of ∼1 MHz. After locking to the correct transition, we have about 25 mW of laser power. We send a small portion through a 2 W Eagleyard tapered amplifier and then through an AOM set up to get the coupling beam frequency to be resonant with the $F = 2 \rightarrow F' = 2$ transition. The probe laser needs to be shifted 6.834 GHz to meet the $\delta\omega$=0 requirement discussed in section 3.4 and has to be passed through 2 high frequency AOMs. Unfortunately, these AOMs have much lower diffraction efficiencies (about 10%) than the lower frequency (∼200 MHz) AOMs. We also need to limit the power through the high frequency AOM, as to not damage them. Each AOM has a center frequency of 1.7 GHz. We use a double pass set up for the AOM to get approximately 1 mW of power shifted by 3.4 GHz. This is amplified by a 1 Watt Eagleyard tapered amplifier before passing through another high frequency AOM. Although 1 mW is a fraction of the power usually used to seed the amplifiers, the housing that hold the tapered amplifier were specially made and optimized for this wavelength (780 nm). After both high frequency AOMs the beam is shifted by 6.8 GHz and a final AOM set up is used to put the probe on resonance with the $F = 1 \rightarrow F = 2'$ transition. Figure 4.9 is a diagram of the

experimental set up used to create both beams. Figure 4.10 is a photograph of the set up that we used to create the coupling and probe beam. After being shifted to the correct frequency, the beam passes through a fiber to ensure a Gaussian beam before going through the chamber. Using this set up the lasers have a relative frequency stability at the Hz level relative to one another [46].

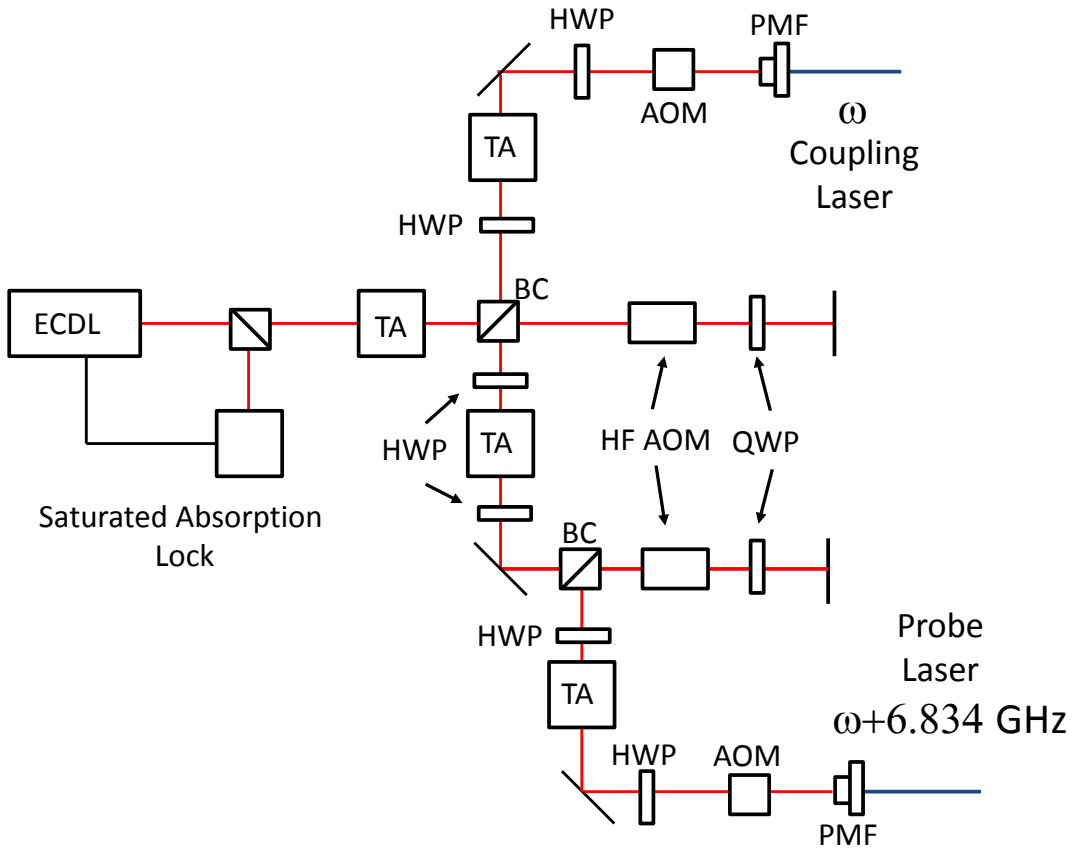

Figure 4.9 Experimental set up to shift a portion of the seed laser 6.834 GHz. The external cavity diode laser (ECDL) is locked to a ^{87}Rb transition through a saturated absorption lock set up. An initial tapered amplifier (TA) provides enough power to seed the coupling laser TA and pass through the first high frequency acoustic optical modulator (HF AOM). Each HF AOM is in a double pass configuration using a beam cube (BC) and quarter wave plate (QWP). Other AOM fix each laser to the exact wanted frequency. Half wave plates (HWP) adjust the linearly polarized seed laser to optimize coupling to the TAs. Both lasers go to polarization maintaining fibers to produce a good TEM00 output mode before being sent into the chamber.

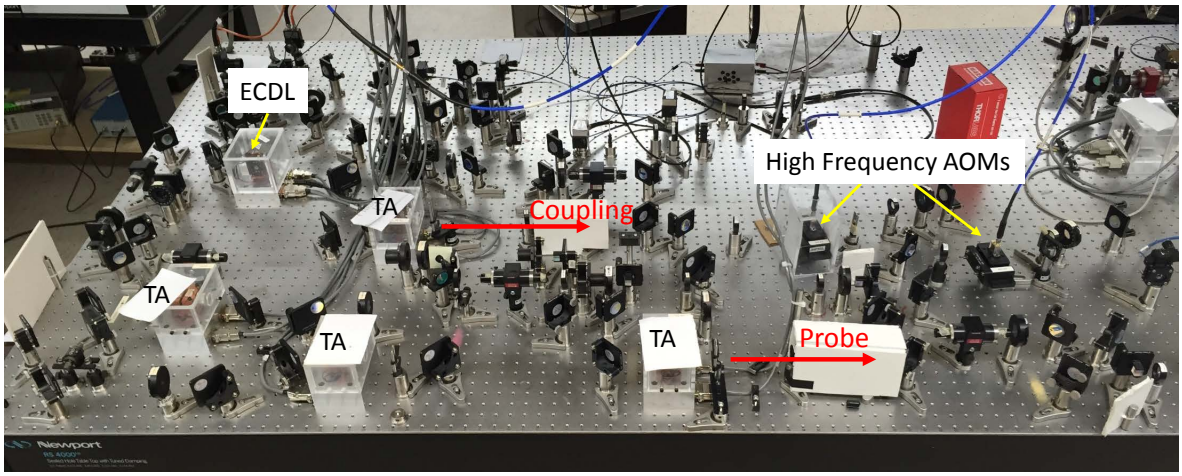

Figure 4.10 Photograph of the experimental set up used to create the 6.834 GHz separation. The probe and coupling beams are created from the same ECDL. Four tapered amplifiers (TA) and two high frequency AOMs are needed to produce two lasers that are 6.8 GHz apart. Additional AOMs (not pictured here) were used to shift the beams to the exact frequency needed for the experiment. This set up was used for all of the EIT lasers in this thesis.

The low frequency AOMs have an efficiency of up to 70% and can quickly diffract an input beam in less than 10 ns. The diffraction efficiency is dependent on the RF power with 1 W producing the most diffraction. We use these AOMs not only to accurately shift the laser to the correct frequency, but also to quickly turn on and off the beams. Any diffracted light is physically displaced from its original beam path, which lets us turn the beam on and off by varying the RF power to the AOM. The laser is diffracted to a different position depending on the RF frequency applied on the AOM. To minimize the motion of the shifted light with changing frequencies we often use a double pass set up [47]. With this type of set up our laser remains well aligned to the fibers over frequency ranges up to ± 10 MHz.

4.5 EIT Absorption Set Up

Now that we have the FORT atoms and the two EIT lasers, Ω_c and Ω_p, we can experimentally study the dark state. Our goal is to see an absorption plot like Fig. 3.3 a., showing no absorption

of Ω_p when $\Delta\omega_p$=0 and $\delta\omega$=0. A difficult part of this experiment was measuring absorption with such a small number of atoms. Since the FORT only trapped around 100,000 atoms, a very low laser power (on the order 100 pW) was needed to see any absorption. The probe travels along the FORT beam path in a counter propagating set up. All of the lenses in the beam path work equally well for 850 nm and 780 nm light. The probe is split from the FORT beam path with a long pass dichroic beam splitter centered at 800 nm. This allows the 850 nm FORT beam to pass through the filter while the probe beam is reflected from it and directed onto a photodiode. The probe laser is focused on to the FORT atoms in attempt to better overlap the beam with the atoms.

We monitor the probe beam before and after passing through the FORT with a photodiode to measure any absorption. The photodiodes are connected to a Stanford Research Systems preamplifier to record the photodiode signal. A high gain is needed to detect such a small signal, but a high gain comes at the cost of a lower bandwidth. We are limited on the length of the pulses since we need to turn the FORT laser off to prevent any unwanted signal from reaching the photodiode. By turning the FORT laser off, the atoms slowly begin to drift away from where they were trapped. We use pulses approximately 200 μs long. In this time the atoms do not move a large amount, and it is a long enough time that we can get the gain we need to measure the photodiode signal.

The coupling beam is not recorded during the absorption measurement and was much easier to set up. To see no absorption, Ω_c must be much larger than Ω_p, and we set the power of the coupling beam to 150 μW. The coupling beam is overlapped with the FORT atoms using a collimated beam with a $1/e^2$ radius of 0.6 mm, much larger than the region of FORT atoms.

The coupling and probe beam are linearly polarized orthogonal to one another. By setting the quantization axis along the direction of the probe beam, the two orthogonal polarizations allow EIT to couple parallel ground state m_F levels through a σ^+ or σ^- transition. Figure 4.11 shows the coupling that occurs between the 3 possible channels for m $\rightarrow$ m$'_F$=m$_F$+1 transitions. Similar transitions occur for the m$_F$ $\rightarrow$ m$'_F$-1 transitions. Appendix I explains the polarization in more detail.

We also attempt to minimize distortion of the laser frequency by shaping the 200 μs probe pulse into a Gaussian pulse in time. Merely switching the AOM on and off would produce a square

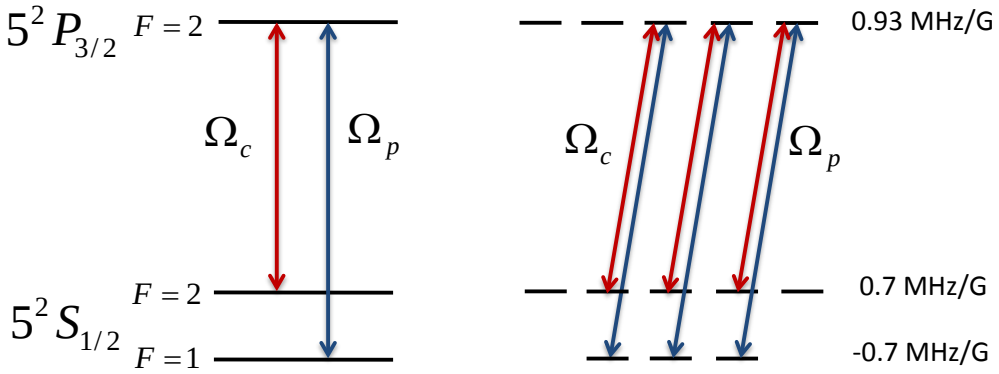

Figure 4.11 The two linearly polarized coupling and probe beam allows EIT to occur between 3 parallel m_F level channels. Pictured on the right are the $m_F \rightarrow m'_F$+1 levels. The $m_F \rightarrow m'_F$ -1 transition are also allowed. Each hyperfine level can have its degeneracy lifted by an external magnetic field. This splits the F=1 ground state m_F levels by $m_F \times$-0.7 MHz/Gauss.

pulse, with rise times of about 20 ns. Using a Fourier transform, the resulting frequency space would have unwanted frequencies. By switching to a Gaussian pulse shape, any measurement in frequency would act more Gaussian, eliminating any unwanted frequencies. We use an arbitrary waveform generator to slowly change the probe over 200 μs. The Gaussian waveform goes to a Hittite integrated circuit that can quickly attenuate an RF signal up to 8 GHz. We attenuate the RF signal that is applied to the AOM that turns the probe beam on and off.

4.6 EIT Results

We scan over the frequency of the probe while recording its photodiode signal before and after it passes through the FORT atoms. With no coupling beam, we observed see a normal absorption plot with up to 50% absorption. An RF generator scans the probe beam over 30 MHz using the double pass AOM set up mentioned earlier. Because of the double pass set up, the alignment through the fiber remains relatively unaffected by the change in frequency.

The coupling beam is turned on before the probe to ensure that the atoms reach the dark state when the probe beam is turned on. This is the counter intuitive nature of the EIT scheme, where

the coupling beam dresses the un-populated states before turning on the probe. Fig. 4.12 plots the absorption of the probe as we change its frequency. Note the large increase in transmission when the probe beam is on resonance, which shows the transparency created through the dark state. We scan the probe over 30 MHz and observe transparency when the probe is on resonance ($\Delta\omega_p$=0).

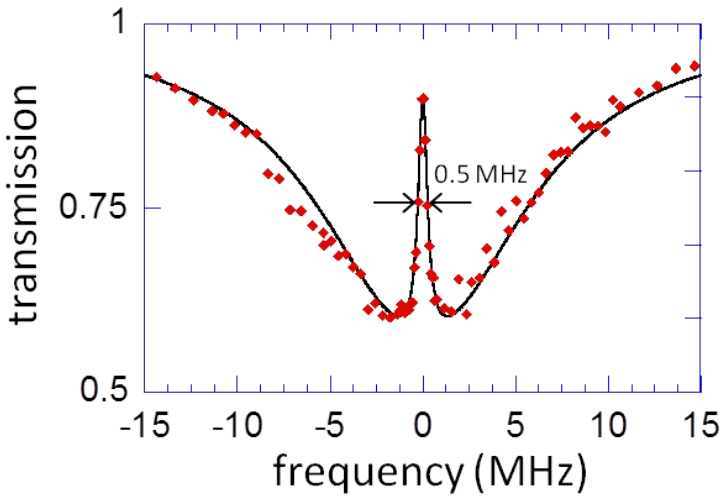

Figure 4.12 Scanning the probe power over probe detuning ($\Delta\omega_p$). The probe beam was very weak, on the level of picowatts while the coupling power was 150μW. The shim coils were optimized to reduce Zeeman splitting. The transparency window was 0.5 MHz. The solid black line is a simulation using experimental parameters.

The transmission approaches 90% and has a width of about 0.5 MHz. This width is dependent on the decay rate of the excited state as well as the intensities of the probe and coupling beam. Larger coupling power tends to broaden out the transmission window as expected. Ideally the transmission would be 100 %, but the multiple m_F levels can interact differently with the probe and coupling laser because of the different dipole matrix elements. If the magnetic field were zero, then the levels should be degenerate and peak transparency should happen for all three m levels at the same probe frequency. The shims coils do not produce an absolute zero magnetic field where the FORT atoms are trapped and therefore the m levels are slightly separated be the Zeeman effect. We can see this splitting by scanning the probe over a small frequency range around the probe resonance.

4.7 Magnetic Field Splitting

The EIT absorption plot in Fig. 4.12 was taken with the shim optimized to reduce the magnetic field at the FORT as well to produce a narrow feature. The plots in this section show multiple peaks in the transparency window around $\Delta\omega$=0. The multiple peaks occur from the 3 different possible channels that EIT can occur through from the three initial m levels. Each hyperfine level (F) can be split by an external magnetic field into 2F+1 m levels. Figure 4.11 shows the m levels from each splitting and the strength that an external field has on that hyperfine level. Once the degeneracy of the hyperfine levels is lifted by an external field, the energy level diagram becomes more complicated and is pictured in Fig. 4.13. For our experimental set up the coupling beam has a fixed frequency and the probe frequency is changed, effectively changing $\Delta\omega_p$ and $\delta\omega$. Fig. 4.13 shows that for a fixed coupling beam frequency EIT would occur at multiple probe frequencies depending on the initial m_F level (*i.e.*, the probe beam has to be different to satisfy the $\delta\omega = 0$ condition).

Figure 4.14 are absorption scans around $\Delta\omega_p$=0 for different magnetic fields and coupling powers. The red plot in Figure 4.14 a. shows two different transmission peaks around $\Delta\omega_p$=0, approximately 500 kHz apart. Both scans in Figure 4.14 a. were taken with the same low probe power as the data in figure 4.11, but at 250 μW coupling power instead of 150 μW. The magnetic field was adjusted by changing the current of the shim coils. The B field that was parallel to the propagation of the probe and coupling beams had the most effect on the separation of the peaks. We adjusted the shim coils to try and minimize the separation and plot the result in green in Fig. 4.14. Adjusting the shim field by around 0.3 Gauss greatly reduced the splitting.

Figure 4.14 b. shows the effect of changing Ω_c on the width of the transmission peaks. The frequency window where transparency occurs depends on $\Delta\omega_p$ and $\delta\omega$. The width of this window for small probe powers is $(\Omega_c)^2/(4\Gamma)$. By decreasing the probe power to 150 μW, thus decreasing Ω_c, we observe a smaller transmission window. With narrower features, we still find evidence of the magnetic splitting discussed earlier. We tried optimizing the magnetic field to completely get ride of the splitting, but our set up at the time was not sensitive enough to accurately control the 3

shims to completely negate the magnetic field, and this was not the main focus of the experiment at the time. The small frequency difference between the peaks indicates a magnetic field along the path of the probe beam of about 0.1 Gauss, less than that of the Earth's field, which is in the range of 0.3 to 0.6 Gauss. The splitting could be resolved with more optimization of the 3 shim fields.

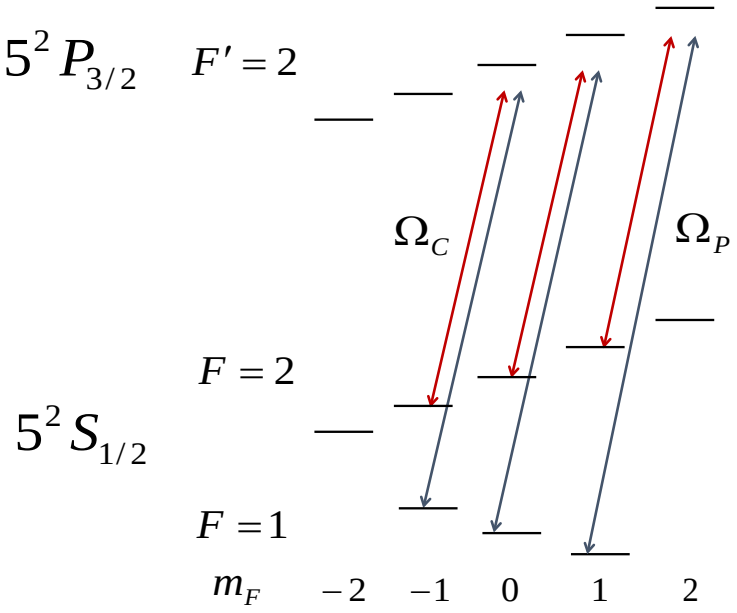

Figure 4.13 D_2 energy levels in the presence of a magnetic field. The F=1 level splits opposite of the F=2 and F′ =2 levels in the low field assumption. The coupling beam is on resonance with the m_F=0 to m_F=0 transition. The splitting causes EIT to occur ($\delta\omega$=0) at different probe frequency depending on the initial m_F level.

4.8 Conclusions

EIT was demonstrated with atoms in a red detuned dipole trap using the D_2 line in ^{87}Rb. Absorption of a weak probe beam over varying detunings showed transparency when both the coupling and probe beam were on the 2 photon resonance of 6.834 GHz, the separation of the two ground state hyperfine levels. The transparency window of 0.5 MHz was limited by the non-zero magnetic field at the center of the trap. This transparency showed that our experimental set up can

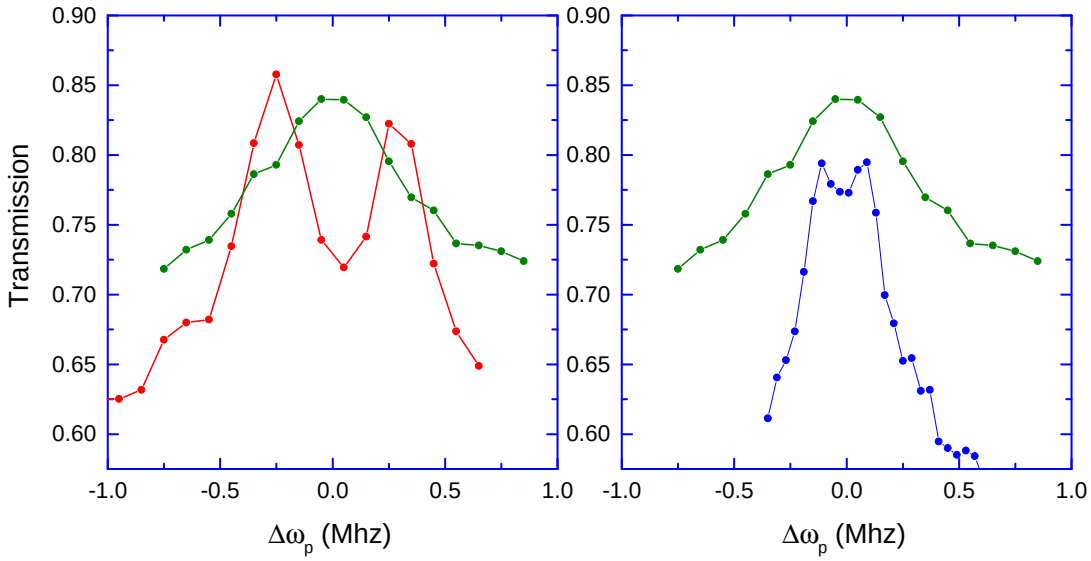

Figure 4.14 Plotted on the left is the transmission peak for 250 μW coupling power. Green was plotted with shims at 2.6 A, while the red plot had shim currents at 5 A. The B field was produced parallel to the probe beam. Plotted on the right is the same green plot, and in blue EIT data at a reduced power of 150 μW. The lower power resulted in a 0.5 MHz transparency window similar to that seen in Fig. 4.12.

put the atomic system into the dark state, which is crucial for the localization work in the following chapters. The data is a large improvement over our past EIT data obtained with MOT atoms [35].

Chapter 5

EIT Standing Wave

5.1 Introduction

Exciting atoms to different energy levels is often done with focused lasers, but this is normally limited to features no smaller than $\lambda/2$ for lasers traveling through a vacuum. In a typical lab setting, the numerical aperture of the focusing lens rarely approaches one, with commercial aspheric lenses from Thorlabs going to NA=0.61 for a short focal length of 3.2 cm. For our experimental setup, the atoms are 15 cm from the walls of the chamber, which greatly limits our max value for NA, and therefore limits the spot size of a focused laser. To get around this, we use the dark state of EIT to localize the excitation of atoms that would otherwise be impossible with a focused laser.

Chapter 4 showed experimental evidence that our laser system could produce EIT in FORT atoms via the dark state. Now I will go into detail how using the dark state can address atoms in areas smaller than allowed by the diffraction limit. As explained in chapter 2, there have been many research groups working to image or address atoms in areas smaller than the diffraction limit (λ/2). The dark state has advantages over other localization techniques due to the absence of spontaneous emission. It has been suggested by other groups that the dark state can be utilized to excite atoms at the nanometer level. Agarwal and colleagues were the first to propose a scheme that utilized EIT [48]. The idea was expanded on by our group [49] and Lukin [50]. Lukin also proposed that the coherent nature of this excitation could be utilized in quantum computing. Investigations of the interaction time of the EIT lasers, along with the population redistribution between hyperfine levels, have been performed by Elliot *et al* [51].

One method to achieve localization with EIT is to use a spatially varying standing wave as the coupling beam [48, 50]. Standing waves have been utilized to establish laser intensities varying by $\lambda/2$ and have been used to trap single atoms [52]. As explained further in section 3.4, excitation occurs in EIT depending on the ratio of Ω_p and Ω_c. By creating a standing wave with variations in Ω_c, the population transfer will change depending on the position of the atom. This region can be made very small to create population transfer in sub diffraction limited areas.

5.2 Previous Work in Yavuz Lab and Limitations

The first localization experimental work in the Yavuz lab was done by Proite *et al* in a ^{87}Rb filled MOT. They used a coupling beam standing wave with a spatial period of about 600 μm [35]. Atoms were transferred between the F=1 and F=2 ground states in areas around the nodes of the standing wave, localizing the transfer to 150 μm areas. We extend the idea of the experiment to the nanometer scale by using a standing wave with a smaller spatial period. With lasers at λ =780 nm, we create a standing wave with two counter propagating waves, making a spatial period of $\lambda/2$. We use atoms trapped in a FORT since our localization technique will require 1) much colder atoms so the atoms do not move once being localized and 2) more homogeneously spread atoms so that the entire atomic population is uniform. Initially all atoms are in the lowest ground state, F=1, and we try to identify where atoms are transferred to F=2 in the FORT after 1 EIT pulse sequence. Since these areas are smaller than the diffraction limit, standard imaging techniques cannot be used to image where the atoms are being transferred. This is an importance difference compared to the previous work with a larger period standing wave. In Proite's work, the 150 μm areas of localization were resolved by an electron-multiplying CCD camera. A fluorescence measurement was performed on the transferred atoms, and the resulting emission was recorded on the camera. If the atoms were in areas below the diffraction limit, the emission would not be resolvable.

5.3 Auto Correlation Experiment

Since we cannot use standard imaging techniques to resolve the areas of transfer, we use an auto correlation technique using two EIT pulse sequences. For this thesis the term "EIT pulse sequence" refers to the probe and coupling beams both being turned on to transfer atoms. The basic idea is that by making a change in our two EIT pulse sequences we can cause a measurable change in the atoms. Fig. 5.1 is cartoon of the timings used for this technique. This change can be accurately measured and be used to discover what happened during one EIT pulse sequence. Similar correlation techniques are used for measuring the pulse widths of ultra-fast lasers in nonlinear crystals [53].

We do the localization experiment with ^{87} Rb atoms trapped in a FORT laser and evaporatively cooled to low temperatures. The atoms must be cold so that they move very little during the experiment. The resulting cold atoms are captured in small line along the focus of FORT laser. Before turning on the EIT lasers, all atoms are initially pumped into the F=1 level. The FORT laser is also turned off, but since the atoms are cold, the atoms move very little during the auto correlation experiment. We first perform one EIT pulse sequence with a coupling beam standing wave that varies as $\Omega_c \sin(2\pi x/\lambda)$ and a constant probe beam. During the two pulses, atoms are transferred to F=2 depending on the local values of Ω_c and Ω_p. Since Ω_c spatially varies, so will the population of F=2. Using the work from chapter 3, we can define the populations in F=2 as

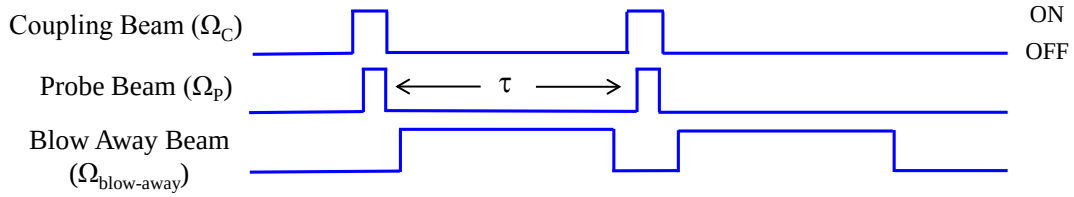

Figure 5.1 Timings for the auto correlation experiment. The term EIT pulse sequence refers to the times when both the coupling and probe beams are on. Two EIT pulse sequences separated by a time τ will determine what happens during one EIT pulse sequence. Detailed information is provided in the text.

$$\langle F = 2|\Psi_{dark}\rangle = \frac{|\Omega_p|^2}{\Omega_c^2 \sin^2(2\pi x/\lambda) + \Omega_p^2} \tag{5.1}$$

Equation 5.1 is plotted along with the intensity of the standing wave in Fig. 5.2. It shows the probability that the atoms will be in F=2 is highest when the intensity of the coupling beam is at its lowest.

After performing one EIT pulse sequence, there are small areas within the FORT where atoms are transferred to the F=2 energy level. Figure 5.3 is a cartoon that shows what atoms along the standing wave are transferred to F=2. If we were to try and image the F=2 atoms through a fluorescence measurement, the small areas would not be resolved. These areas are in regions that are less than λ/2 in length, and thus would be diffraction limited with a standard imaging technique. However, we do have a technique to measure the atoms in F=2. The atoms in F=2 are heated by a separate laser called the blow away beam, $\Omega_{blow-away}$, which does not interact with the cold F=1 atoms. After being heated, the only cold atoms remaining in the FORT are in the F=1 level. Due to the heating, the F=2 atoms have a higher average velocity, and would eventually leave the FORT area. This does not happen, since there is not enough time for the atoms to leave the FORT area before the second EIT pulse.

Before the second EIT pulse sequence, the standing wave is moved relative to its initial position by an amount δx. This is done by adjusting the frequency between the two coupling beams by an amount, δf, moving the standing wave toward the higher frequency laser by an amount

$$\delta x = \delta f \tau (\lambda/2). \tag{5.2}$$

The time τ is the time between the two EIT pulse sequences. It is also in this time that $\Omega_{blow-away}$ is heating the F=2 the atoms. δf needs to be very accurate in order to move δx at levels below the diffraction limit (*i.e.*, we have to accurately move the standing wave a few nanometers). For τ = 1μs (similar to values used in the experimental data), δf needs to be accurate at the kHz level, which we easily achieve using Hewlett Packard RF signal generators.

For the second EIT pulse sequence, we ignore the F=2 atoms because of the heating, and only focus on the remaining cold atoms. This pulse happens at a time τ after the first pulse, and although

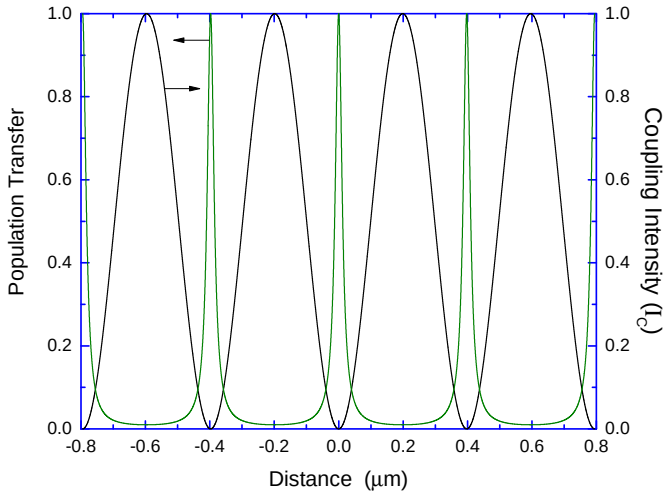

Figure 5.2 Plotted on the left axis is the population transfer to F=2 calculated from equation 5.1. The population is plotted against distance, which is the variable x from equation 5.1. The probe beam is at a constant power. The intensity of the coupling beam is plotted on the right axis. The largest population transfer occurs when the intensity is near zero.

the F=2 atoms are heated, they are still close to their initial position in the FORT and have not left the FORT area before the second EIT pulse sequence arrives. When the second EIT pulse sequence is turned on, the standing wave has been shifted by δx, changing the position of the nodes relative to the first EIT pulse, and therefore changing where the atoms are transferred to F=2. Fig. 5.3 shows atoms near the nodes of the standing wave during the second EIT pulse sequence being transferred to F=2 when δx=$\lambda/4$. $\Omega_{blow-away}$ is turned on again after the second EIT pulse sequence, heating atoms that are in F=2. After $\Omega_{blow-away}$ is turned on for the second time, the FORT laser is turned on, re-trapping the cold F=1 atoms, while the heated F=2 atoms are unable to be trapped due to their temperature. With the cold F=1 atoms trapped in the FORT, we wait for an adequate amount of time (approximately 30 ms) until the hot F=2 atoms travel away from the center of the FORT. After this entire sequence of events, the total number of F=1 atoms is recorded and plotted against δx. Fig. 5.3 shows a cartoon of the atoms before we image them. The small areas with no atoms exist because the F=2 atoms have been blown away from the original group of FORT atoms. These regions are in areas smaller than the diffraction limit, so we would be unable to directly image

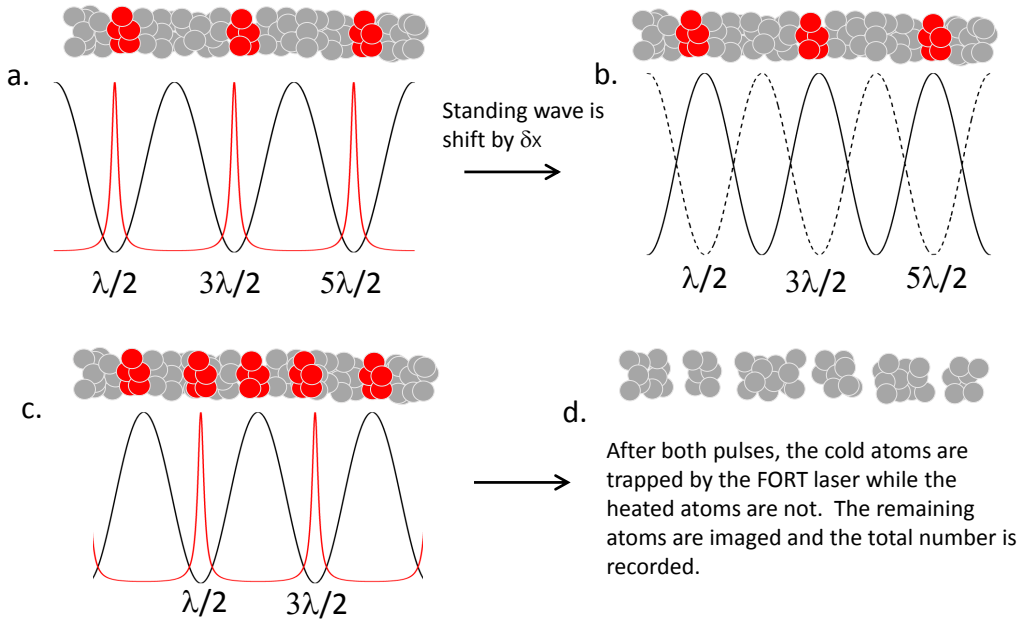

Figure 5.3 Cartoon of the auto correlation technique. a.) 1 EIT pulse is performed with the standing wave, transferring atoms at the nodes. Red atoms are in F=2 while gray atoms are in F=1. b.) Standing wave is shifted by δx, during this time atoms in F=2 are heated by $\Omega_{blow-away}$. c.) The EIT beams are turned on again, but now the transfer may occur at a different areas in the atoms, depending on δx. In this case δx=λ/4 and a large amount of transfer occurs. d.) The remaining cold atoms are trapped again with the FORT laser. They are then imaged and recorded vs δx. Heated atoms are too hot to be trapped in the FORT laser.

them. The remaining F=1 atoms are imaged by a ECCD camera with a fluorescence measurement. A detailed explanation of this measurement is in appendix C. This population is plotted against δx and is the auto correlation data used to calculate what happens during 1 EIT pulse sequence. Fig. 5.4 is a cartoon of the data for varying values of δx. Each data point represents the autocorrelation experiment at different values of δx. For the case δx=0 the second EIT pulse would transfer very few atoms, since the atoms affected by the second EIT pulse would have already been heated by the first EIT sequence. For δx=λ/4, the nodes would be moved to positions with cold atoms, and the second EIT pulse sequence would transfer these cold atoms into F=2. The data is periodic with the period of the standing wave. Peak values are seen at multiples of $n\lambda/2$ where n is an integer

and λ is the wavelength of the EIT lasers. A minimum signal is seen at $(n + 1/2)\lambda/2$. The data in fig. 5.4 is dependent on where the transfer in each EIT pulse sequence occurs.

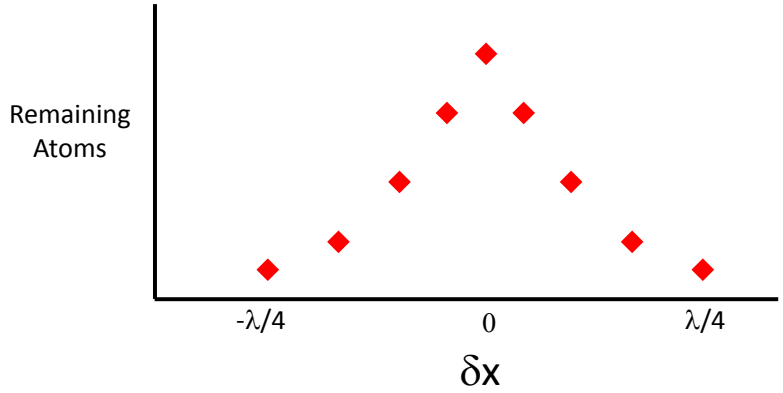

Figure 5.4 Representation of the total number of atoms remaining in the FORT for different values of δx. The most atoms are recorded when δx is close to zero. When δx is half the period of the standing wave, $\pm\lambda$/4, more atoms are transferred and blown away after the two EIT pulses sequences, and therefore the total number of atoms is the lowest.

5.4 Finding the Effects of One EIT Pulse Sequence

The resulting autocorrelation data is dependent on the effect of one EIT pulse sequence. We attempt to simulate the autocorrelation to find out what is happening during one EIT pulses sequence. One important aspect of our autocorrelation experiment is the atomic motion between the two EIT pulses. During the time τ, atoms need to move very little so that the motion of the cold atoms does not blur out any features created by the transferred F=2 atoms. We use FORT atoms to achieve cold temperatures, and we perform the experiment in a few microseconds. We simulate the effect of one EIT pulse using the atomic motion and autocorrelation data. The simulations are created by solving the density matrix equations. We perform a convolution of the simulated transfer from one EIT pulse sequence with the effect so of the thermal motion of the atoms in the time between pulses. We then take that result and do a convolution with the effect of the second EIT pulse sequence. The resulting simulation should be the same as the experimental correlation data. If the simulation matches the experimental data, then we can infer what happens during one

EIT pulse sequence. The simulations show transfer occurring in areas smaller than the diffraction limit. A more in depth explanation of the simulation is in Appendix H.

5.5 Conclusions

We use an autocorrelation technique to determine the effects of atomic transfer using EIT. The transfer occurs in regions smaller than the diffraction limit, which makes a direct optical measurement impossible. By correlating the effects of two EIT pulses sequences, we can infer the size of the small regions in which atoms are transffered.

Chapter 6

D_2 line Experiment

6.1 Introduction

Extending our EIT work from chapter 4, we first perform the autocorrelation experiment with FORT atoms using the D_2 line in ^{87}Rb. I will go through our first efforts in seeing localization, including some early experimental set ups that were sub-optimal. Our first results will show proof of the autocorrelation technique discussed in chapter 5. After optimizing certain parameters we show transfer into the F=2 state in regions of 100 nm, a factor of $\sim$8 less than the wavelength of the two EIT lasers.

6.2 Experimental Parameters

The standing wave is created from two coupling beams, each having a $1/e^2$ beam width of 0.6 mm. The beams are overlapped with each by passing each beam through the other beam's fiber launch. This makes sure that the two beams are well aligned to one another. The probe beam has a $1/e^2$ beam width of 1.1 mm and is overlapped with the FORT atoms. Although the same energy levels are used as the EIT experiment in section 4.4, the setup is different with the addition of a second coupling beam and the blow away beam ($\Omega_{blow-away}$). The relvent evergy levels for this experiment are pictured in Fig. 6.1. A diagram of the setup is in displayed in Fig. 6.2. We split the coupling beam using a polarizing beam cube into two AOM's, so we have independent control over each coupling beam. The probe and coupling beam frequencies are set 6.834 GHz away from each other using the high frequency AOM set up discussed in section 4.4. The FORT atoms are produced by the same 850 nm laser.

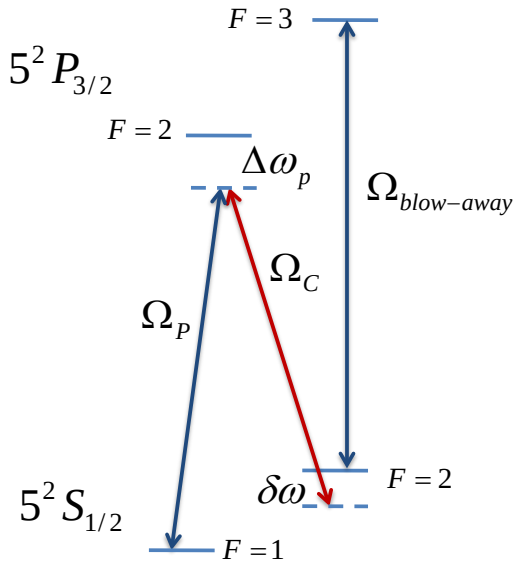

Figure 6.1 Three level scheme for EIT. Both the probe and coupling beam are detuned by a small amount $\Delta\omega_p$ from the excited F=2 level. $\delta\omega$ is the two photon detuning. $\Omega_{blow-away}$ is resonant with a cycling transition where the decay channel F=3 $\rightarrow$ F=1 is forbidden. The atoms are continually pumped between the levels, heating them in the process.

6.3 First Autocorrelation Data

Fig. 6.3 shows our first evidence of a standing wave using the autocorrelation experiment discussed in chapter 5. The probe and coupling beams were each 10 MHz detuned from their respective transitions. The probe power was kept constant at 14 mW while two 5 mW counter propagating coupling beams formed the standing wave. The resulting standing wave ranges in power from 0 mW to 25 mW. We used 0 mW as the node of the standing wave since the most transfer should occur when Ω_c is at a minimum, as discussed in section 5.3. The timing for this setup is in figure 6.4. To change δx, we decided to keep a fixed frequency between the two coupling beams at δ_f=830 kHz and vary τ, the time between the two EIT pulse sequences. The blow away beam was kept constant at 1 μs. We had found 1 μs sufficiently heated the majority of the atoms but later increased this time to 1.5 μs to more accurately heat the atoms. Fig. 6.3 shows oscillations in the remaining FORT atoms with a period of around 1.2 μs. This relates well to δf, with a predicted

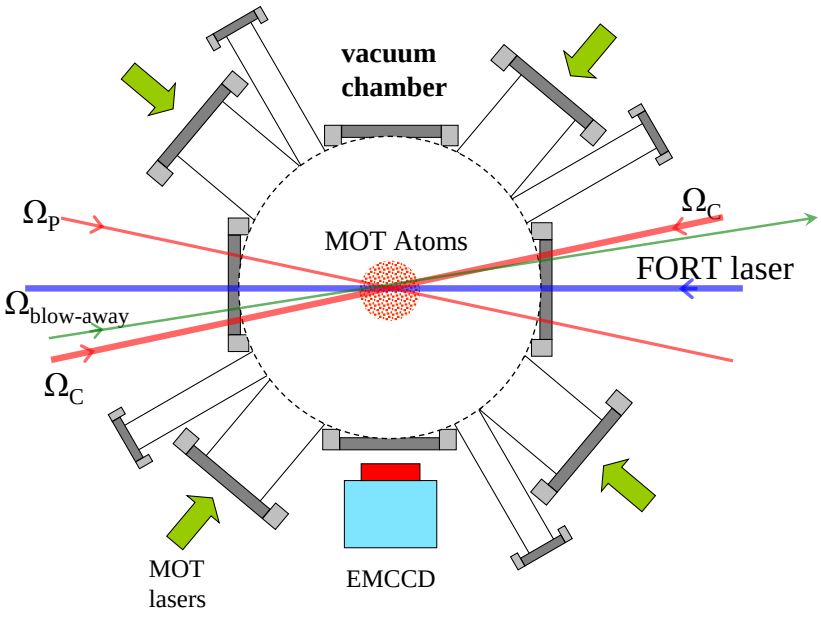

Figure 6.2 850 nm FORT laser traps atoms from the MOT. The two coupling beams are independently controlled and overlapped with one another to produce a standing wave with a period of 390 nm (λ/2). In green is $\Omega_{blow-away}$, heating the atoms in between the two EIT pulse sequences.

period of exactly 1.205 μs. A peak value in population was measured at $\delta x = n\lambda/2$, when the standing wave was in the same position for both EIT pulse sequences. These experiments were done with probe and coupling beam pulses at 100 ns in length. Our preliminary data was not optimized to start at peak overlap between the two EIT pulses yet it does show evidence of the standing wave at the appropriate time scales. This was our first evidence of the autocorrelation experiment working and in the following sections I will discuss improvements to the experimental procedure.

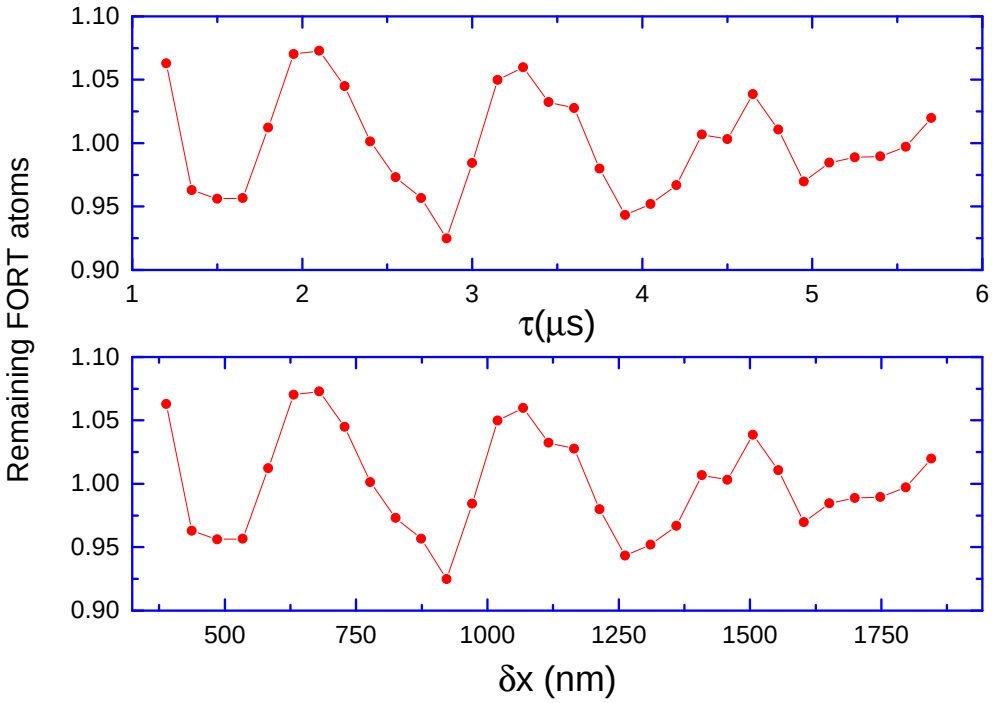

Figure 6.3 First data of autocorrelation experiment. Remaining F=1 atoms are plotted over the time between EIT pulse sequences (τ). δx is calculated using the using δf=830kHz, the frequency difference of the two coupling beams. As expected, the plots show maxima around δx=nλ/2 and mimima around δx=(n-1/2)λ/2.

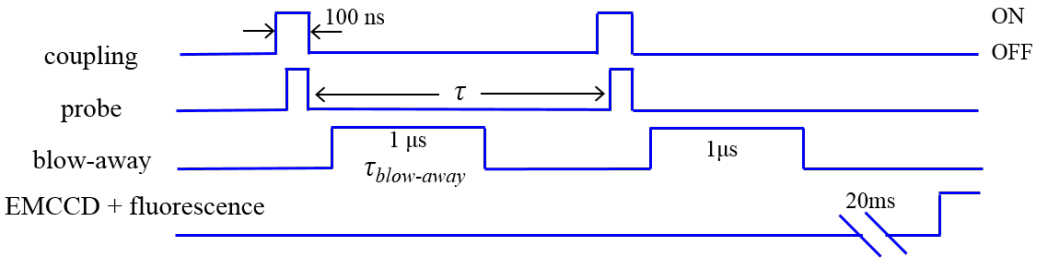

Figure 6.4 Timings for localization by varying time

6.4 Data Acquisition

This section will discuss how we measured the F=1 population after the two EIT pulse sequences. The FORT population after the autocorrelation measurement is recorded with a florescence measurement. The cycling transition used was the same used for $\Omega_{blow-away}$. We tuned the MOT beams on resonance to F=2 to F′=3 transition to image the atoms for 1 ms. The atoms first needed to be pumped into F=2 by the MOT repumper, and then were imaged by the now on resonance MOT beams. We tried to maximize the FORT signal by using the 3 retro reflected beams, but this also caused some unwanted background signal on the camera. Figure 6.5 is an example of the FORT data taken with the MOT beams. We expect the most atoms to be at the center of the FORT, coinciding with the highest intensity but we also observe fluctuations in brightness across the entire FORT. The fluctuations are caused by interference of the 3 retro reflected MOT beams as we image the atoms. We address these problem later in our work in the D_1 line of ^{87}Rb.

Also plotted in Fig. 6.5 are the FORT atoms after the autocorrelation experiment is performed. The blow away beam is loosely focused over the FORT atoms and propagates perpendicular to the camera. Any atoms heated by $\Omega_{blow-away}$ slowly travel away from the FORT, separating themselves from the cold F=1 atoms. The image shows a cloud of atoms off center from the FORT, propagating in the direction of the blow-away beam. These are the atoms that were transferred to F=2 during the two EIT pulse sequences. The blow-away beam does not uniformly heat all of the atoms, giving them a spread of velocities as they leave the imaging area. We take data at the center of the FORT where it is the brightest, and therefore should have the highest atom number. The data was taken by averaging over multiple pixels of the ECCD where the FORT signal was the greatest. If $\Omega_{blow-away}$ does not sufficiently heat the atoms, the camera may image the unwanted F=2 atoms. To prevent this we set the pulse time of $\Omega_{blow-away}$ to 1.5 μs in the next iteration of the experiment. The heated atoms also need time to travel away from the cold F=1 atoms in the FORT. We find that waiting 30 ms provides enough time for the heated atoms to travel away from the FORT.

The measurement procedure is a very destructive process. The once cold F=1 atoms are now heated and the resulting image gives us one data point. This process is repeated about 100 times

for the same experimental parameters in order to reduce fluctuations in FORT loading. The entire process to create the MOT, trap the atom in a FORT, perform EIT pulses, and take a measurement, takes about 1 second. Therefore, each data point for one δx value takes a few minutes to acquire. This can result in the data acquisition time for the experiment to approach an hour. In this amount of time, we have to worry about fluctuations of laser power from all of the EIT lasers as well as the lasers that produce the MOT and FORT atoms.

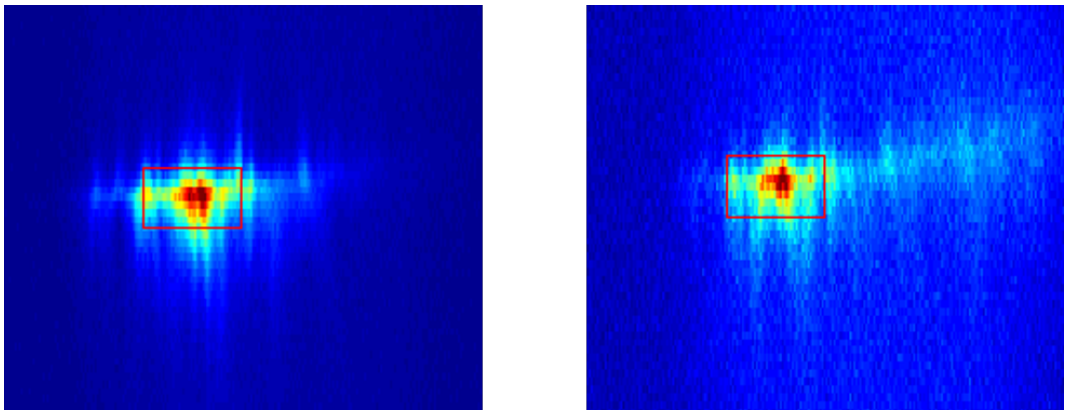

Figure 6.5 Pictures of both FORTS with and without the blow away beam. (right) Atoms heated by $\Omega_{blow-away}$ are leaving the FORT but can remain in view of the camera if not enough time is allowed after re trapping atoms.

6.5 Atomic Temperature and Changing δx

Varying δx by changing τ can create unwanted problems in the autocorrelation data. The atomic temperature of the atoms causes them to spread out during the time of the experiment. Increasing τ increases the distance the atoms move, possibly blurring any narrow features that were created from the first EIT pulse. We can measure the atomic temperature using a time of flight measurement [54]. The FORT laser is abruptly switched off, letting the atoms disperse radially from their initial position. For our first data, the atomic temperature was close to 8.5 μK, resulting in an average velocity of 40 nm/μs. At larger values of τ the atoms, on average, would travel the length of one standing wave period, completely washing out any features. We solve this by fixing τ to be equal to $\tau_{blow-away}$, and move δf to change δx. Changing the frequency can also

blur out features. For δ_f=830 kHz, used for the data in Fig. 6.3, the standing wave moves 1 period (390 nm) in 1.2 μs. This corresponds to 16.25 nm during the 50 ns probe pulse. The benefit of changing δf is that we expect a peak signal when δf (and therefore δx) is zero. At this peak signal we also know that standing wave is not moving, and not producing any blurring features.

We decrease the atomic temperature in order to see the small features produced by the autocorrelation experiment. We use a time of flight measurement to measure an atomic temperature and use evaporative cooling to achieve the lowest temperatures [55]. To evaporatively cool the atoms we set up the FORT AOM after the TA, thus completely turning the trapping laser off, eliminating any amplified spontaneous emission (ASE) that could otherwise be coupled to the fiber. We measure the spread of the atoms by imaging them for a short time, 100 μs, up to 4 ms after the FORT is turned off. We fit a Gaussian to the spread of the atoms and plot the 1/e radius against the time of flight. Figure 6.6 shows two TOF measurements for the max and low temperature recorded with this FORT. At max power, with no evaporative cooling, the temperature is approximately 49.5 μK, giving the atoms an average velocity of 68.8 nm/μs. We evaporatively cool the atoms to 5.6 μK (v=23.2 nm/μs) over 50 ms. At the time, our set up restricted the lifetime of the FORT, and cooling for longer would adversely affect the total atom number. Improvements to the lifetime is discussed more in section 7.4.

6.6 Determining Max Transfer to F=2

We did this experiment trying to optimize the amount of atoms that were transferred to F=2 through EIT. The most transfer happened when the lasers were on resonance with the excited state, but when we performed the autocorrelation experiment described in chapter 5, we didn't see the data oscillate with changing δx. At the time, the experiment worked best when we were off resonance to the red of the excited state. We optimized parameters with the EIT lasers off resonance from the excited state to get the most transfer to F=2.

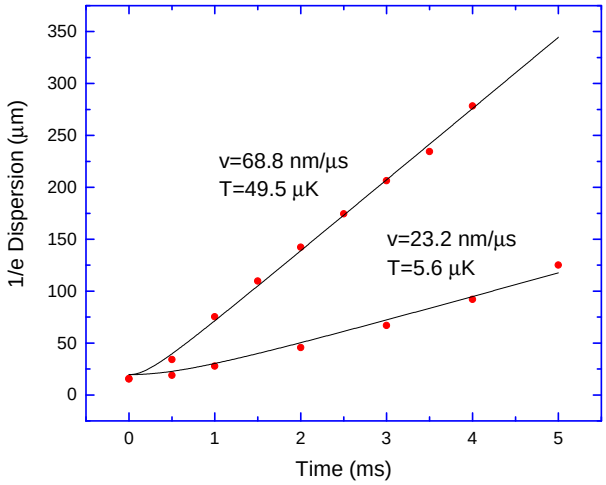

Figure 6.6 Time of flight (TOF) measurement with and without evaporative cooling. For a FORT power of 100 mW the measured temperature is 49.5μK. Evaporative cooling to a lower power, about 10 mW, reduced the temperature to 5.6 μK.

6.6.1 Transfer Curve

Before performing the autocorrelation experiment, we take a closer look at the effects of 1 EIT pulse with no standing wave. We use similar parameters from section 6.3, using a probe beam size of 1.1 mm and coupling beam size of 0.6 mm. The coupling beam has a pulse width FWHM of 100 ns with 20 ns rise times. The probe is 50 ns with 20 ns rise times. We use a larger coupling beam pulse to make sure the coupling beam is on before the probe beam, to assure that we are in the dark state. To get the similar rise times we make sure to focus the laser through the final AOM with similar focal length lenses. The rise times are checked with an oscilloscope. We first test the result of transfer to F′=2 with one coupling beam at varying powers for a fixed probe power. The detuning is changed to 35 MHz to avoid single photon processes. We also experimentally found that this produced a larger difference in remaining FORT atoms between δx=0 and δx=$\lambda/4$ when performing the autocorrelation experiment. To get a large transfer to F=2 the coupling beam was position 25 MHz away from resonance. Although this made $\delta\omega$=-10 MHz, we found this produced the most transfer. We also found that we could get a large amount of transfer to F=2 by using 5

mW of probe power. Figure 6.7 shows that for these parameters the maximum amount of transfer occurs at around 3 mW of coupling power. For lower coupling powers, the Rabi frequency is small, and transfer would require longer pulses. We kept the probe pulse at 50 ns to emphasize the speed of EIT. In general, the transfer curve shows that more atoms remain in the F=1 ground state as the coupling power is increased. This follows the analytical solution for the population in F=1 from the dark state in equation 3.5, where the population in F=1 is

$$\langle F = 1|\Psi_{dark}\rangle = \frac{|\Omega_c|^2}{\Omega_c^2 + \Omega_p^2} \tag{6.1}$$

For the standing wave experiment, we want the most transfer to occur at the nodes, where the coupling power is small. Since the most transfer occurs at a non zero power we create a standing wave that is offset from 0 by using two different coupling beam powers. The minimum of this standing wave will be at 3 mW of coupling power, so that the nodes coincides with the most transfer to F=2. A detailed discussion of creating the standing wave is discussed in appendix D.

6.6.2 Two Photon Detuning

Here we go through a more thorough check of the detuning parameters. The single photon detuning is set by the probe beam with no coupling beam present. The beam is greatly reduced in the power, and the interaction time is increased to about 2 μs. By reducing the power we avoid any stark shifts with other energy levels in the $5^2P_{3/2}$ manifold. When the probe is overlapped with the atoms and is on resonance to the F=1 $\rightarrow$ F$'$=2 transition, we see a large amount of transfer. Since the beam is low power, atoms are not transferred off resonance. This way we can accurately set the probe beam to 35 MHz away from its resonant frequency. When the single photon detuning of the coupling beam is also set at 35 MHz, corresponding to a $\delta\omega$=0, we should get large amount of transfer to F=2. Fig. 6.8 shows that experimentally we see the most transfer occurs around $\delta\omega$=-10 MHz. In the density matrix equations from section 3.5 we used only the three EIT levels. The simulations predict the most transfer occurs at $\delta\omega$=0, but the simulations neglect other energy levels from the D_2 line. To get a more accurate simulation, we needed to consider contributions from the other excited hyperfine levels. The probe sits 35 MHz detuned from F=2, but that beam

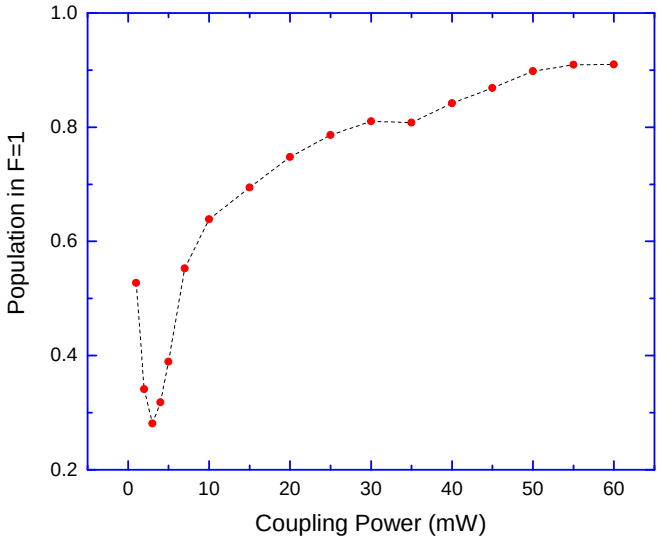

Figure 6.7 Population in F=1 after 1 EIT pulse plotted against different coupling powers. The probe beam is 35 MHz detuned from resonance. The coupling beam is set at a frequency that optimizes transfer to F=2, approximately 25 MHz detuned from resonance. At coupling powers lower than 3 mW, the transfer does not follow the analytical equation 6.1. Ω_c is low at these values, and would require more time to reach the dark state. This data was taken with only 1 coupling beam, there was no standing wave.

is simultaneously interacting with the three other hyperfine levels, the closest being F=1 only 121 MHz away. Although the simulations correctly predict any type of stark shift caused by the EIT beams for the 3 EIT energy levels, the simulations neglect any contributions from the other 3 hyperfine levels. The stark shifts created from these levels create the 10 MHz shift and vary with changing coupling and probe intensity. For this reason, we optimize the coupling frequency and power to see the most transfer to F=2. We experimentally found that 3 mW of coupling power, 5 mW probe, and $\delta\omega$=-10 MHz created the most transfer.

6.7 STIRAP

We perform a stimulated Raman adiabatic passage (STIRAP) measurement to simulate the autocorrelation experiment. STIRAP is a technique using two coherent laser pulses to transfer

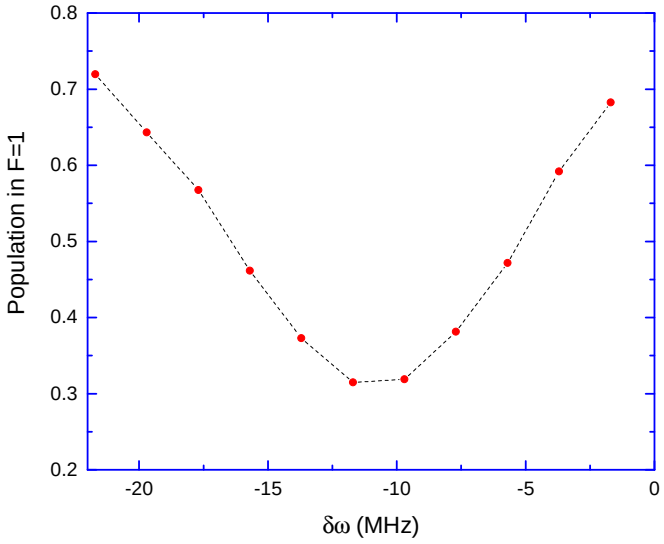

Figure 6.8 Population in F=1 after 1 EIT pulse sequence for a fixed coupling power 3 mW and probe power 5 mW over $\delta\omega$. The large deviation from the ideal case is created by stark shifts from other levels near F′=2.

atoms between state without spontaneous emission [56]. We perform it for the off resonance case and probe powers listed earlier while at 3 mW coupling power, where the max transfer to F=2 takes place. STIRAP data was also taken with only one coupling beam, and no standing wave. The STIRAP data in figure 6.9 emphasizes that the process requires both lasers, and is much easier to see when the single photon detuning is far away from resonance. Showing that the set up is two photon process makes a good argument that the process is coherent, and the transfer does not occur from spontaneous emission from the excited state F=2′ into F=2. In this plot, the population transfer is the amount of atoms transferred into F=2 and the time delay is measured relative to when the coupling beam ends in comparison to the probe beam. At 0 ns the coupling beam turns off at the exact same time as the probe, and is where the optimal amount of transfer should take place. At -200 ns, the coupling beam turns off 200 ns before the probe, making it so there is no overlap between the two beams. This prevents any two photon process to occur and any transfer to F=2 occurs through spontaneous emission from the F′=2 excited state. Since the probe is 35 MHz away from resonance and is only 50 ns in pulse width, very little pumping to the F=2 state

occurs. At 200 ns, the coupling beam is turned on after the probe beam ends, and some of the atoms transferred to F=2 are pumped back to F=1 by the coupling beam. In either case the amount that is transferred from single photon processes is very small compared to the two photon process when the beams are overlapped. This emphasizes that the dark state is responsible for the transfer and that it is a coherent process.

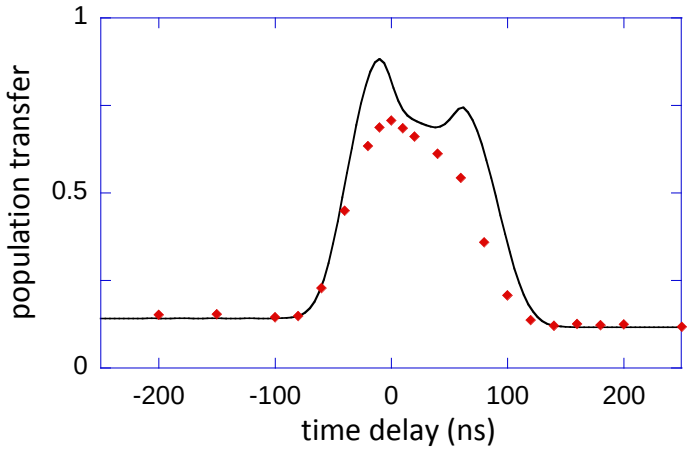

Figure 6.9 STIRAP measurement of Population in F=2 for 3 mW coupling power and 5 mW probe power plotted against the time the coupling beam is turned off relative to the probe beam. A delay of 0 ns corresponds to both EIT beams ending at the time. For negative times, the coupling beam was turned off before the probe beam. The coupling had a pulse width of 100 ns while the probe had a pulse width of 50 ns.

The black line in Fig. 6.9 is a simulation including experimental parameters with one fitting parameter. The simulation best matched the experimental data when the intensities of the probe and both coupling beams are decreased by about 20%. One likely explanation for the error is a misalignment of the coupling beams to the FORT atoms. For the simulation we assume atoms are initially distributed evenly along the three F=1 m_F levels. The simulation is an average of simulations using each channel individually. Each simulation only contained the three EIT levels needed for one channel. A more detailed and much more time consuming method would be to construct a 13x13 Hamiltonian considering each of the 13 individual m_F levels used in the hyperfine levels. Since the simulations reasonably followed the experimental data, we used the parameters for the

STIRAP data, along with the small correction factor for the intensities, to simulate the autocorrelation plots. It is important to note that changing Ω_c, which happens with the standing wave, the STIRAP data would change.

6.8 Autocorrelation Data

Now that we have the frequencies and powers set for both EIT beams, as well as a good simulation for one EIT pulse, we perform the autocorrelation experiment that is detailed in chapter 5. Fig. 6.10 shows experimental data for standing waves varying from 3 mW to 14 mW in (a) and 3 mW to 30 mW in (b) while the probe is at 5 mW. 3 mW was picked as the node of the standing wave to correspond with the most transfer to F=2. Appendix D describes how we chose the laser powers to create the appropriate standing wave. We construct the standing wave using two laser δx is changed by adjusting the frequency difference between the two beams. The two EIT pulse sequences are separated by 1.5 μs. The data in Fig 6.10 is plotted against δx but experimentally each point was taken when δf was changed by 50 kHz. At the larger δx values the frequency difference approaches $\pm$1 MHz, changing the two photon detuning from -10 MHz to -9 MHz or -11 MHz. From the two photon detuning plot in Fig. 6.8, this amount of detuning has a small effect on the transfer. Each data point was accumulated over 100 times.

As expected, both plots in 6.10 are periodic with the standing wave period at $\lambda/2$=390 nm. For the lower power case in (a), the data resembles a sine wave while the plot in (b) shows slightly narrower features around δx= -390 nm, 0 nm and 390 nm (-λ, 0 and λ). The minimum points occurred around -180 nm and 180 nm (-λ/4 and λ/4), as expected. We measure the FWHM of the data around δx=0 for both plots and get 182 nm for the 3 mW to 14 mW case and 129 nm for 3 mW to 30 mW. The simulations are plotted along with each of the experimental data and quantitatively follow the features of each plot. This autocorrelation simulation takes into account the 5.6 μK temperature we calculated earlier. The observed feature of 129 nm in Fig 6.10 indicates that the features produced from one EIT pulse must be narrower than $\lambda/4$. A more detailed explanation of how we simulated the autocorrelation data is found in appendix H.

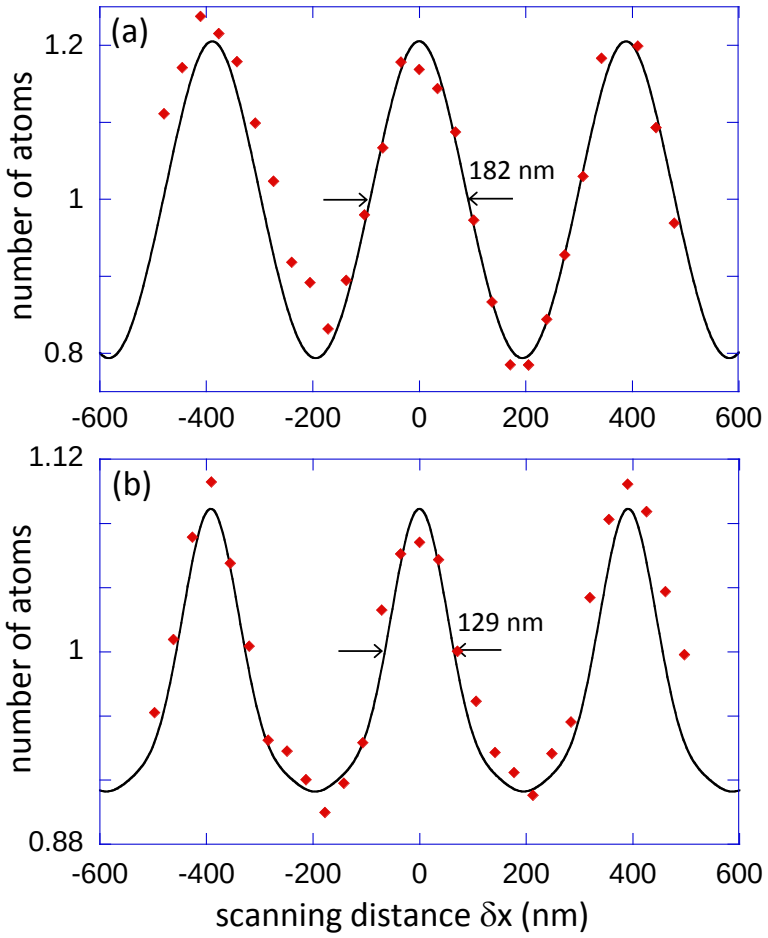

Figure 6.10 The data is the remaining atoms left in the FORT after two consecutive EIT pulse sequences. Atoms that are transferred to F=2 via the EIT pulses are heated and leave the FORT. The remaining number of atoms are plotted against the δx. The probe power was kept constant at 5 mW for both plots. The coupling power changes from 3 mW to 14 mW in (a) and 3 mW to 30 mW in (b). The solid black line is a numerical simulation of the density matrix at each point along the standing wave. The temperature of the atoms were taken into account in the simulations.

6.9 Single EIT Pulse Sequence Simulation Data

The effect of one EIT pulse sequence that was used in the simulation of plot (b) in figure 6.10 is plotted in figure 6.11. The data shows transfer in an area with a FWHM of 100 nm, a factor of 8 smaller than the wavelength of the coupling and probe beams. The simulation was performed by

numerically solving the density matrix with experimental parameters and the small misalignment term used in section 6.7. It is important to note that this plot is a simulation and is plotted over two periods of the standing wave after one simulated EIT pulse sequence. This distance is different than the one used for the autocorrelation plots. The autocorrelation data is plotted against δx, the distance the standing wave moves between EIT pulse sequences. The smaller features in 6.11 are produced because we are not completely overlapped with the dark state over all the powers in the standing wave. These small features also appeared in the STIRAP data in Fig. 6.9. These small features would be completely washed out in the autocorrelation data for the parameters we worked with in the D2 line. When the simulation plot is correlated with a velocity distribution representing the atomic temperature, the small features become blurred out and could not be resolved. The data in Fig. 6.11, along with the atomic temperature, produced the simulations in Fig. 6.10. The 100 nm area creates a larger feature after being correlated with a temperature distribution. This correlation is correlated with an identical EIT pulse (representing the second EIT pulse) and further broadens out any features in Fig. 6.11. This broadens the 100 nm feature into 129 nm. We cannot take an image of the narrow features because of their diffraction limited size. Appendix H has more information about the simulation.

6.10 Dark State Overlap

The simulation in Fig. 6.11 shows odd behavior compared to the analytical dark state case. The analytical case would be a smoother plot that wouldn't have small variations like Fig. 6.11. The oscillations are a result of the system no being completely in the dark state. As discussed in section 3.6, if the lasers are not on for a sufficient amount of time, the populations of F=1 and F=2 may be different than that of equation 3.5. Although the process is coherent, as proved by the STIRAP data, the system may not be completely in the dark state. Increasing the pulse time would get rid of the small oscillations in the simulations, but the autocorrelation experiment requires very fast pulses. The overlap with dark state will be looked at closer in the next iteration of the experiment in chapter 8.

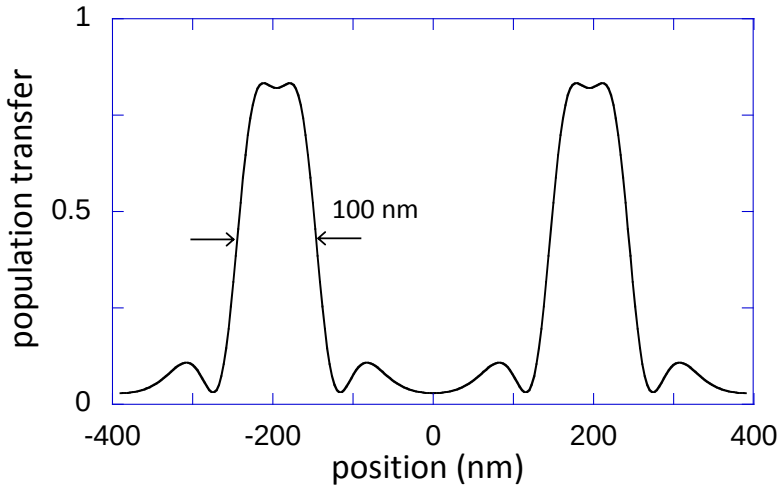

Figure 6.11 The inferred population transfer from F=1 to F′=2 in one EIT pulse sequence over two periods of the standing wave. The coupling beam power varied between 3 mW and 30 mW with 3 mW at the node of the standing wave. In this plot, 0 nm corresponds to a standing wave node. This plot produced the simulated autocorrelation data in Fig. 6.10. The 100 nm feature is approximately a factor of 8 less than the 780 nm light used in the EIT beams.

6.11 Improvements

The autocorrelation data in Fig. 6.10 was very encouraging. As expected, increasing the max standing wave intensity resulted in a narrow feature. The simulations predict that we get even narrower features as we increases the standing wave amplitude. Experimentally we did not see any further narrowing, but there were limitations with the set up. The atomic temperature of 5.5 μK put a limit on what features we can infer from the autocorrelation data. At this temperature our TOF measurement showed the atoms would travel about 40 nm over course of both EIT pulses. To measure widths at this level we would need to cool the atoms much lower, to about 1 μK. The multiple levels in the $5^2P_{3/2}$ manifold may have also contributed to the problem. Our experiment was performed 35 MHz to the red of F′=2, which at the same time is only 122 MHz to the blue of F′=1. One effect from this was the stark shift due to these other energy levels which effected the two photon detuning between the probe and coupling beams. We address these problems in the next chapter. I would also like to note that we tried the experiment on resonance and detuned to

the blue of the excited F′=2 state, but could not get the autocorrelation experiment to work. EIT would still be present when using only one coupling beam, but there were no oscillations in the data for the autocorrelation experiment.

6.12 Conclusion

We performed an autocorrelation experiment on the D_2 line and showed transfer between ground states of ^{87}Rb in regions of width of 100 nm, a factor of 8 less than the wavelength of light used to perform the transfer. The atoms moved in the 100 nm regions were moved using the dark state of EIT, and not through spontaneous emission. The 100 nm is inferred from a simulation using experimental parameters and numerically solving the density matrix equation. Because of the small size, a direct imaging measurement of the atoms was not possible.

Chapter 7

D_1 line improvements

7.1 Introduction

We attempt to improve the localization experiment by using the D_1 line in ^{87}Rb. The two hyperfine levels in the $5^2P_{1/2}$ energy level should better follow simulations compared to the four closely spaced hyperfine levels in the $5^2P_{3/2}$ level. We also attempt to get lower FORT temperatures with a 50 W diode pumped solid state (DPSS) laser at 1064 nm. Although the power is more than sufficient for dipole trapping, the poor mode quality presented problems when we tried to focus it to a small spot size.

7.2 D_1 energy levels

A key advantage of the D_1 line are the widely spread hyperfine levels of the excited state. We will use the same EIT configuration utilizing the F=2 excited state in the D_1 energy diagram in Fig. 7.1. The closest energy level is the F=1 level, 816.7 MHz away from F=2. Since we perform the localization experiment with 100 ns pulsed lasers, there will be a negligible effect from the F=1 level during the experiment. This should make our three level simulations much more accurate. The F=1 excited level is also far enough away that we can ignore the small stark shifts produced by this level. The transition dipole matrix elements are slightly different for the D_1 line, and each σ^+ and σ^- transition has different values compared to the D_2 line. This will change the Rabi frequencies for the coupling and probe lasers. Tables 7.1 and 7.2 shows the corresponding matrix elements for the both transitions assuming a σ^+ transition. This data was taken was from Steck's work [39] [57]. Another advantage of the D_1 line are the weaker landau g factors for the excited

state. Any stray magnetic field will shift the m_F levels of the excited state by a smaller amount than compared to the D_2 line.

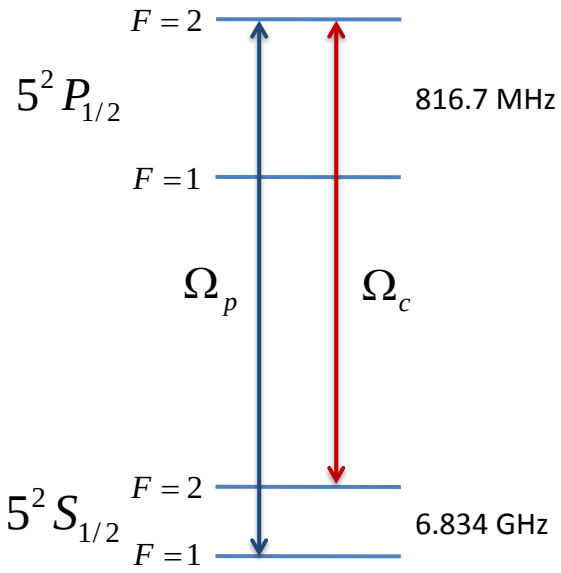

Figure 7.1 Energy diagram using the D_1 line of ^{87}Rb. We perform experiments using the F=2′ excited state, 816.7 MHz away from the closest transition. The wavelength of light that couples these two levels is 795 nm.

Laser locking was slightly more difficult. For the closely space D_2 lines, the saturated absorption lines produce large cross over transitions to lock to. Locking to the F′=1, F′=2 crossover becomes difficult when the two levels are 816.7 MHz apart. The vapor pressure in the cell is increased by wrapping it in heat tape. The increased density gives a strong enough signal to lock to.

The D_2 tapered amplifiers could provide up to 1 Watt of power with only 2 mW of seed power. These tapered amplifier did not perform well at the D_1 line wavelength of 795 nm, and were replaced with M2K amplifiers.

	m_F= -1	m_F= 0	m_F= 1
F=2	$\sqrt{\frac{1}{8}}$	$\sqrt{\frac{1}{8}}$	$\sqrt{\frac{1}{12}}$
F=1	$\sqrt{\frac{1}{24}}$	$\sqrt{\frac{1}{8}}$	$\sqrt{\frac{1}{4}}$

Table 7.1 Dipole matrix elements for σ^+ transitions in the D_2 line of ^{87}Rb (F,$m_f \rightarrow$ F′=2,m'_f=m_f+1) expressed as multiples of the dipole matrix element for the $5^2S_{1/2} \rightarrow 5^2P_{3/2}$ transition ($\langle J = 1/2||er||J' = 3/2\rangle$=3.584$\times 10^{-29}C\cdot$ m)

	m_F= -1	m_F= 0	m_F= 1
F=2	$\sqrt{\frac{1}{4}}$	$\sqrt{\frac{1}{4}}$	$\sqrt{\frac{1}{6}}$
F=1	$\sqrt{\frac{1}{12}}$	$\sqrt{\frac{1}{4}}$	$\sqrt{\frac{1}{2}}$

Table 7.2 Dipole matrix elements for σ^+ transisitions D_1 line of ^{87}Rb (F,$m_f \rightarrow$ F′=2,m'_f=m_f+1) expressed as multiples of the dipole matrix element for the $5^2S_{1/2} \rightarrow 5^2P_{1/2}$ transition ($\langle J = 1/2||er||J' = 1/2\rangle$=2.537$\times 10^{-29}C\cdot$ m)

7.3 DPSS Laser System

We changed our dipole trap laser to a wavelength of 1064 nm to reduce the amount of heating from the FORT. Although the dipole trap laser is far off resonance from any transition, there is still a small chance that a photon will be absorbed by the atom. This would heat the atom by a very small amount, and if to many photons are scattered the atom will leave the FORT. The rate at which this occurs is called the scattering rate, and for a far off resonant laser the rate is

$$\Gamma_{scatter} = \frac{3\pi c^2 \Gamma^2}{2\omega_o^3 \Delta^2} I = \frac{\Gamma}{\Delta \hbar} U_{dip} \tag{7.1}$$

The scattering rate varies proportional to $1/\Delta^2$, so it's advantageous to use a laser that is very off resonance from the transition in the atom. For the conditions in the D_2 line experiment the initial FORT depth was 0.5 mK. This creates a scattering rate of 15 Hz. By increasing the FORT detuning to 1064 nm, we reduce the scattering, which in turn gives us longer lifetimes. If we assume the same FORT depth, the scattering reduces to about 4 Hz. Keeping this rate small allows us to evaporatively cool the atoms for longer. For higher scattering rates the atoms are heated faster, and have a greater chance of leaving the FORT.

We purchased a 1064 nm DPSS laser module to replace our 850 nm FORT laser. This module could output up to 50 W of power. Although the power of the laser was impressive, the laser was very multi-mode due to its configuration. The module was placed in a low finesse cavity with mirrors of reflection $\sim 99\%$ and 80%. The low finesse allowed us to operate the laser without any type of locking, but the poor quality of the laser output gave us problems. The laser output was very multi-mode, making it very difficult to couple any usable amount of power through a single mode fiber. Some attempts were made to improve mode quality. Placing a Brewster cut window within the cavity reduced the mode in one direction, but many longitudinal modes were still visible. The polarization was also random, and approximately half the power was lost going through a polarizing beam cube, to make sure we only used one polarization for the FORT. The focus was greatly affected by the multi-mode nature. We could not easily expand the beam through a telescoping lens set up, and instead we let the beam propagate approximately for about 2 meters

before loosely expanding it by a factor of 2. We measured the focused beam size to be about 50μm $\times$ 50μm, a factor of 5 larger than the 850 nm laser. Because the beam couldn't be tightly focused, the resulting FORT depth was $\sim 0.5m$K, similar to the FORT depth used with the 850 nm dipole trap. We did trap more atoms though, since the FORT area was much larger. Overall, this laser was not worth the time and effort I put into it.

7.4 FORT Lifetime With 1064 nm Laser

We expected a longer lifetime using the the 1064 nm laser with the reduced scattering rate, but saw similar lifetimes as the 850 nm laser at around 800 ms. We found that the ASE from the MOT beams when the TA is not seeded would heat the atoms over millisecond timescales. We put a switch to physically block the ASE when the MOT beams are not in use. Fig. 7.2 shows the lifetime of the FORT with and without this switch. We improved the lifetime by over 200 ms which allowed us to evaporatively cool longer while not losing as many atoms. After this improvement our lifetime became limited by the background collisions in the vacuum chamber. Atoms that were not trapped in the FORT are still at room temperature within the chamber. These "hot" atoms can collide with the ultra cold FORT atoms, ejecting it from the FORT. The measured decay rate of $\sim$1 s^{-1} for our chamber pressure of 3×10^{-9} Torr relates well to previous work [58].

7.5 Imaging the FORT and Temperature Measurement

For experimental data in chapter 6, we imaged the resulting atoms using the large MOT beams tuned to on resonance with the cycling transition. We used the retro reflected beams on resonance with the cycling transition to fluorescence any atoms in the F=2 state. Appendix C discusses this fluorescence measurement in more detail. During the imaging we would also use the repumper so we could continually fluoresce atoms for up to a 1 ms. With this set up we attempted to use the binning feature of the camera in an attempt to increase the signal to noise ratio. This binning feature reduces the background count on the pixels of the camera where the signal is very low. Unfortunately the background would increase along with the signal, and the binning feature did

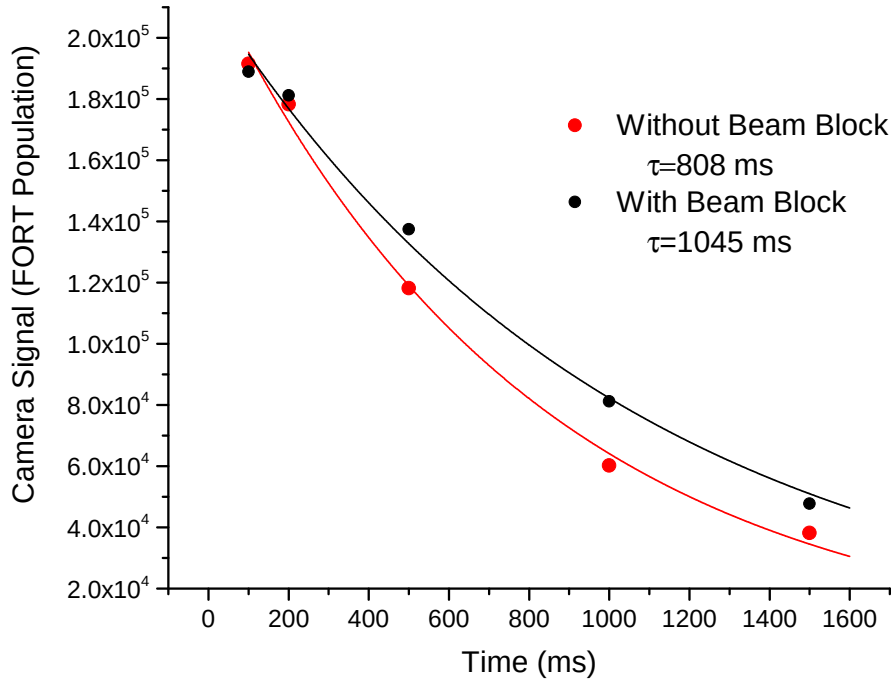

Figure 7.2 Lifetime measurement with and without a physical shutter to block ASE from the MOT TA. The data was fit with an exponential decay. The lifetime was improved by blocking the ASE from the tapered amplifier while the FORT remained on. The population was measured at different times after the trapping of the FORT atoms was complete. While the atoms remained in the FORT, some atoms were ejected from the trap due to collisions with uncooled atoms in the chamber.

not help us. We discovered that the retro reflected beams were so large, $1/e^2$ diameter of 2 cm, that light was scattering off parts of the chamber producing a large background signal. To remedy this, we used $\Omega_{blow-away}$ to image the atoms. This beam was much smaller than the MOT beams,about 1 mm in diameter, and did not affect the background.

Using the smaller blow away beam, we used a binning feature of 70x4 pixels to take our imaging data. Each pixel on this camera is 8 μm $\times$ 8μm, making the area we take data 560 μm$\times$32μm. Since the beam was not retro reflected in all three dimensions, the atoms would quickly heat up and leave the imaging area in the propagation direction of $\Omega_{blow-away}$. We reduced the imaging time to 200 μs to image the atoms faster so they would not have time to leave the

imaging area. Figure 7.3 shows the signal recorded from the FORT with and without the binning feature for only a few thousand atoms. Without the binning feature, the FORT signal is only 5% brighter than the background signal. Binning changes the way the camera records the data, increasing the signal to noise ratio. In the binning case, the FORT signal is 6 times stronger than the background, making it much easier to record changes in atom number. A trade off to getting a better signal to noise ratio is a loss in the spatial resolution. Spatial resolution is needed to accurately perform a time of flight measurement to obtain the temperature on the atoms.

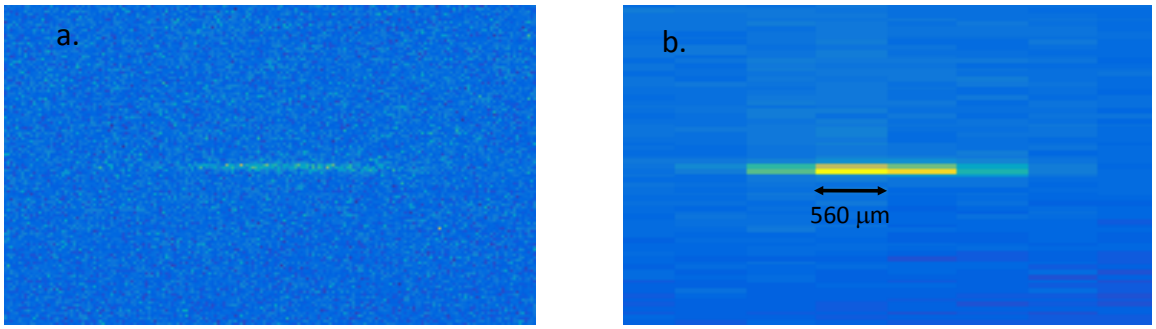

Figure 7.3 Atoms from the FORT are detected through a fluorescence measurement. a) With no camera binning the signal and background are similar intensities with a signal to noise ratio equal to ∼1.05. b) With camera binning the signal to noise is greatly improved with the signal a factor of 6 greater than the background. Spatial resolution is lost when the camera pixels are binned, but the signal to noise ratio is much better.

Because of the higher lifetimes, we evaporatively cooled for 200 ms, 150 ms longer than the cooling with the 850 nm FORT laser, to get colder atomic temperatures in the FORT. With no binning feature, we could record time of flight measurements showing temperature of 3.2 μK relating to an average atomic speed of 17.5 nm/μs. This data is plotted in Fig. 7.5. For the time of flight measurement, the binning needed to be kept to a minimum to resolve how far the atoms traveled over time. Lower temperatures were possible by decreasing the final power of the dipole trap, but time of flight measurements were difficult to perform because of the lower resolution in position on the camera. For this reason, our lowest recorded temperature of 3.2 μK was an upper bound of the temperatures in the FORT.

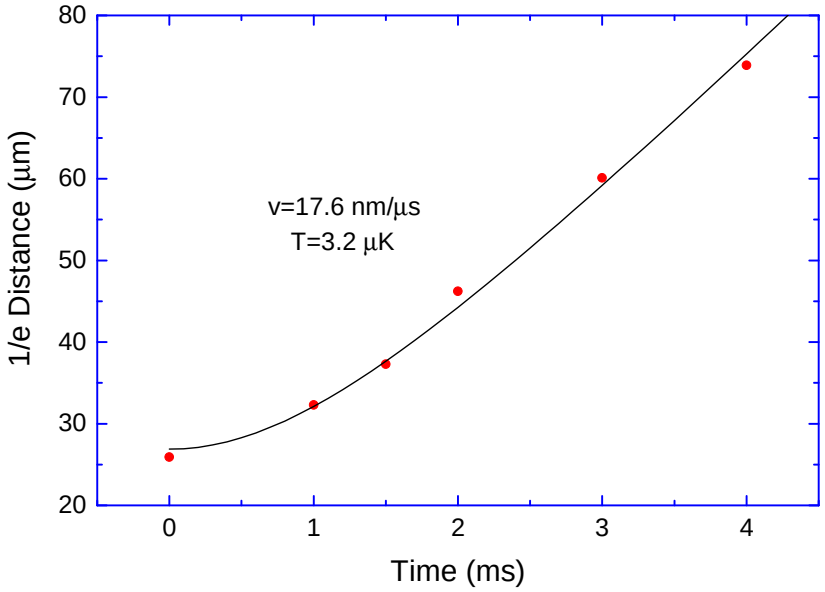

Figure 7.4 Time of flight (TOF) measurement for FORT atoms trapped with the DPSS laser system. The velocity is the most probably velocity assuming a Maxwell-Distribution.

7.6 Conclusions

Improvements were made to the autocorrelation experiment in an attempt to resolve smaller features. Using the ^{87}Rb D_1 line should eliminate the EIT beams interacting with unwanted transitions. A high power 1064 nm dipole trap laser helps achieve colder atomic temperatures. Changing our imaging of the FORT fluorescence will greatly aid in our signal to noise ratio.

Chapter 8

D_1 line Experiment

8.1 Introduction

We perform the autocorrelation experiment using the D_1 line of ^{87}Rb. We produce features that show excitation into the F=2 state in regions of 60 nm, a factor of 13 smaller than the light used to produce the transfer. We take a closer look at the overlap with the dark state over all points of the standing wave. The excitation is fast (150 ns laser pulses) and the overlap with the dark state can be made higher than 94% over all points of the standing wave.

8.2 Off Resonance

8.2.1 Experimental Set Up

Fig. 8.1 depicts the energy levels we used for EIT and the autocorrelation experiment. Ω_c and Ω_p are both positioned off resonance by $\Delta\omega_p$=30 MHz, slightly different than the 35 MHz off resonance for the D_2 line. We set $\delta\omega$=0 which gave us the best EIT transfer, as expected by the simulations. This was in contrast to the localization experiment in the D_2 line, where the stark shifts from other energy levels affected the two photon detuning. The experiment is performed with coupling and probe beams with pulse widths of approximately 150 ns and 100 ns. We doubled the probe pulse width in an attempt to be closer overlapped with the dark state. The beams have a collimated $1/e^2$ beam size of 0.8 mm (coupling) and 1.3 mm (probe). These sizes are large compared to the size of the FORT. We increased the size of the coupling beams to make it easier to align to the FORT atoms. The probe had a fixed power of 3.5 mW. Before performing the localization experiment, we experimentally determine what percentage of atoms transfer to

F=2 after one EIT pulse sequence using only one coupling beam. After the EIT pulse sequence, the blow away beam, $\Omega_{blow-away}$, heats the F=2 leaving only F=1 atoms in the FORT. We plot the percentage of atoms in F=1 over varying coupling powers in figure 8.2. At low coupling intensities, the atoms do not have time to reach the dark state, coinciding with very low atomic transfer to F=2, similar to the D_2 line. The probe does not transfer atoms by itself because of the short interaction time and 30 MHz detuning in respect to the excited state. Ideally, the population in F=1 would follow the analytical case where

$$\langle F = 1|\Psi_{dark}\rangle = \frac{|\Omega_c|^2}{\Omega_c^2 + \Omega_p^2} \tag{8.1}$$

Equation 8.1 would be the population for F=1 for the experimental values of Ω_p and Ω_c assuming steady state. Because of the fast pulses we cannot assume that the populations will exactly follow this analytical solution. We plot the population in F=1 from the analytical solution to the dark state alongside the experimental data in Fig. 8.2.

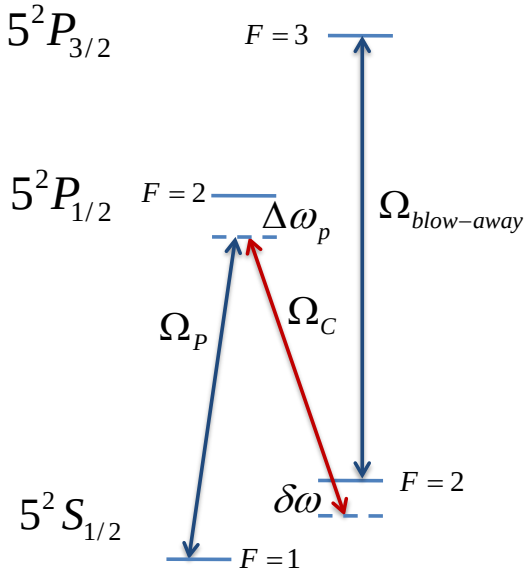

Figure 8.1 Energy diagram for autocorrelation experiment using EIT in the D_1 line of ^{87}Rb. The blow away beam still uses the excited F=3 level of the D_2 line to heat the atoms between the two EIT pulse sequences.

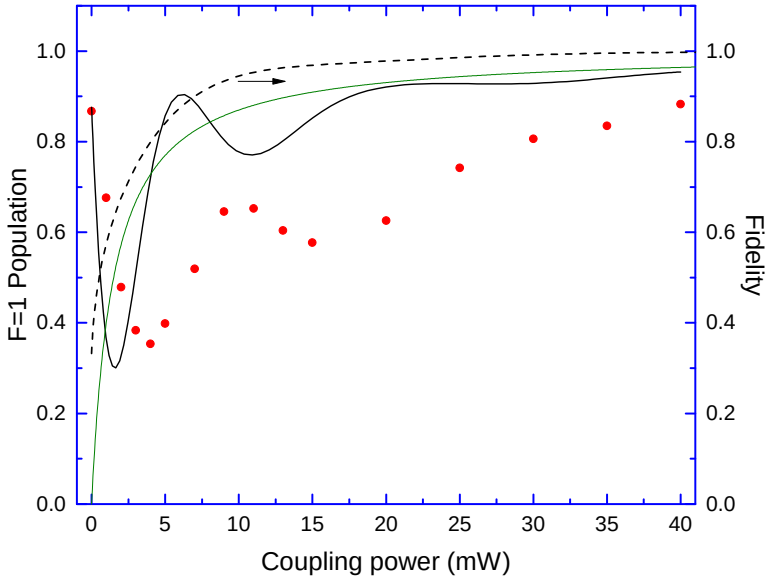

Figure 8.2 Experimental population remaining in F=1 after 1 EIT pulse plotted with respect to coupling beam power. The solid black line is a numerical simulation using experimental parameters. The green line is the population in F=1 using equation 8.1, the analytical dark state solution, with experimental numbers for Ω_p and Ω_c. The dotted line is the fidelity between the simulation and analytical simulations.

Figure 8.3 shows the timing of the experiment. The procedure begins with the MOT being loaded for 350 ms. The 1064 nm FORT beam is turned on for 50 ms while the MOT beams are simultaneously detuned and attenuated. During this time the MOT repumper beam is also attenuated to maximize loading into the FORT. At 400 ms the repumper and MOT beams are turned off as well the magnetic field gradient coils. The FORT atoms are evaporatively cooled for 200 ms and the resulting temperature is approximately 1 μK. The two counter propagating coupling beams are turned on before the probe beam and have pulse widths of 150 ns. The probe beam is turned on for the last 100 ns to overlap with the coupling beam. Next, the blow away beam is turned on for 1.5 μs to heat the F=2 atoms. The cycle is repeated again and the atoms remain in the trap for 30 ms. This gives the heated F=2 atoms time to travel away from the FORT area so none of these atoms are imaged on the camera. The remaining atoms are imaged and the resulting

signal is our autocorrelation plot. For the data in this chapter we changed our data acquisition procedure. This is explained further in appendix E.

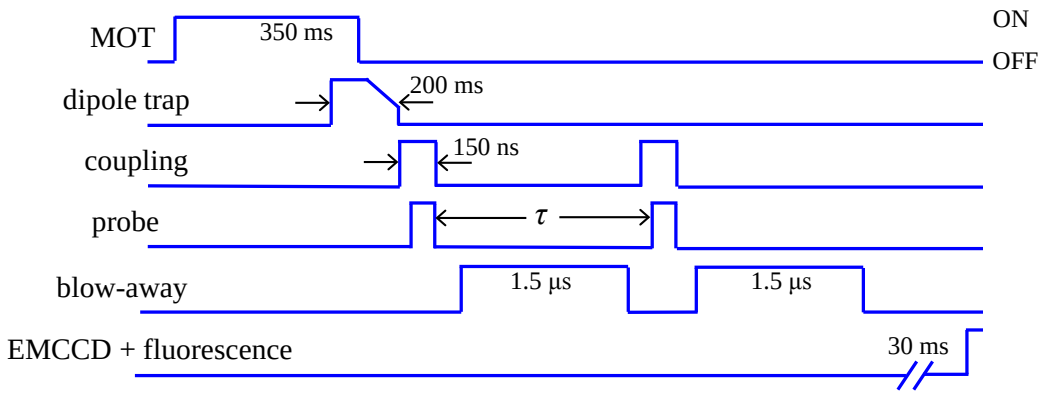

Figure 8.3 Timing of the autocorrelation experiment protocol. After evaporatively cooling the FORT atoms for 200 ms, the first EIT pulse is turned on, transferring atoms to F=2 depending on $\Omega_c(x)$. The blow-away beam heats any atoms that are transferred to F=2. The procedure is repeated with another EIT pulse, after which the remaining F=1 atoms are imaged with a laser induced fluorescence measurement.

8.2.2 Simulations

To simulate the D_1 data we decide to use the transfer curve instead of the STIRAP data. This should be a more thorough simulation because of the various values of Ω_c in the standing wave. We simulate the experimental data by numerically solving the density matrix equations for each parallel m level EIT in the F=1 ground state. We then average over the three possible channels assuming the atoms are initially evenly disturbed across the three F=1 m_F levels. Keeping the probe power constant, we simulate different coupling beam powers and plot them along with the experimental data in Fig. 8.2. Comparing the two plots shows a large difference between the simulated and experimental data. The simulations predict that the population in F=1 should be at a minimum at about half the power used in the experiment. This factor of two seemed to be the case regardless of coupling power. One explanation could be a misalignment of the coupling beam to the FORT atoms, where only a fraction of the measured coupling beam power is overlapping with the FORT atoms. A similar aspect between the experimental and simulated transfer curves is that both

do not perfectly follow the analytical solution to the dark state. Both plots oscillate with increasing coupling power unlike the analytical solution, indicating that our experimental parameters do not perfectly put the atomic system into the dark state. The simulation predicts the population in F=1 should decrease with increasing coupling power between 5 and 10 mW. Experimentally, we saw a similar effect, but at larger powers, between 10 and 20 mW. This was interesting since we did not see such fluctuations from the D_2 line.

The dotted line in figure 8.2 is the fidelity between the simulation and the dark state given by $Tr\left(\sqrt{\sqrt{\sigma}\rho\sqrt{\sigma}}\right)$ [9] where σ is the density matrix of the dark state from equation 3.5 and ρ is the simulated density matrix based on our experimental values. We use the simulations to recreate the experimental localization data so we have information on the fidelity. Experimentally, we only measure the remaining population in F=1 and have no information on the off diagonal elements of the density matrix.

8.2.3 Autocorrelation Experimental Results

We found some interesting things using 0 mW as the node of the standing wave. This was different from the previous work, where we picked a minimum value to coincide with the most transfer to F=2. By using the odd nature of the transfer curve at low powers (*i.e.*, the transfer oscillating with increasing coupling power), we saw interesting features when performing the autocorrelation data.

Figures 8.4(a) and 8.4(b) shows experimental autocorrelation data taken with coupling beam standing waves of 0 to 10 mW and 0 to 20 mW. In this range of power, as seen in figure 8.2, the transfer to F=2 greatly changes with coupling power. This data is scanned over approximately two periods of the coupling beam standing wave and the pattern begins to repeat itself, as expected, when δx = $\lambda/2$. At δx=0 the standing wave has not moved between EIT pulses and few atoms should be transferred to F=2 during the second pulse. Therefore, a maximum in total number of atoms is expected. We observe this in both experimental plots. The traces show features with full-width-half-maximum (FWHM) sizes as small as 70 nm.

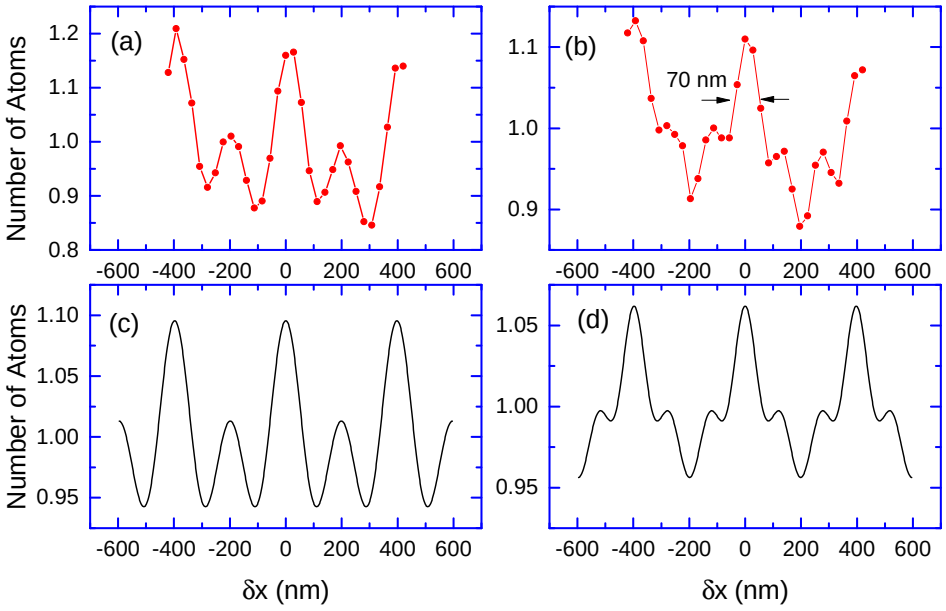

Figure 8.4 The number of atoms remaining in the FORT as a function of the scanning distance of the standing wave δx. The coupling power of the standing waves varies from (a) 0 to 10 mW, and (b) 0 to 20 mW. The data is periodic with a period of half of the wavelength used to create the standing wave, $\lambda/2$=397.5 nm, and the max data points coincide with δx=0. (c) and (d) show the numerical simulations of the density matrix using the power of the standing wave as the only adjustable parameter. The plots (c) and (d) were created with the simulated data in figure 8.5.

Because the simulation and experimental data in figure 8.2 do not perfectly fit one another, we choose a range of coupling powers from the simulation data in an attempt to recreate the experimental localization data. For the 0 to 10 mW case, we simulate a coupling beam standing wave ranging from 0 to 3 mW. Figure 8.5(a) shows the effect of one EIT pulse over one period of the 0 to 3 mW standing wave. The population in F=2 is plotted against a single period of the coupling beam standing wave (λ/2) where 0 nm is the position of the node of the standing wave while the peak intensities are at -198.75 nm and 198.75 nm (-λ/4 and λ/4). This position is not related to δx. As noted earlier each coupling beam has a wavelength of λ=795 nm, thus creating a standing wave with period $\lambda/2$=397.5 nm.

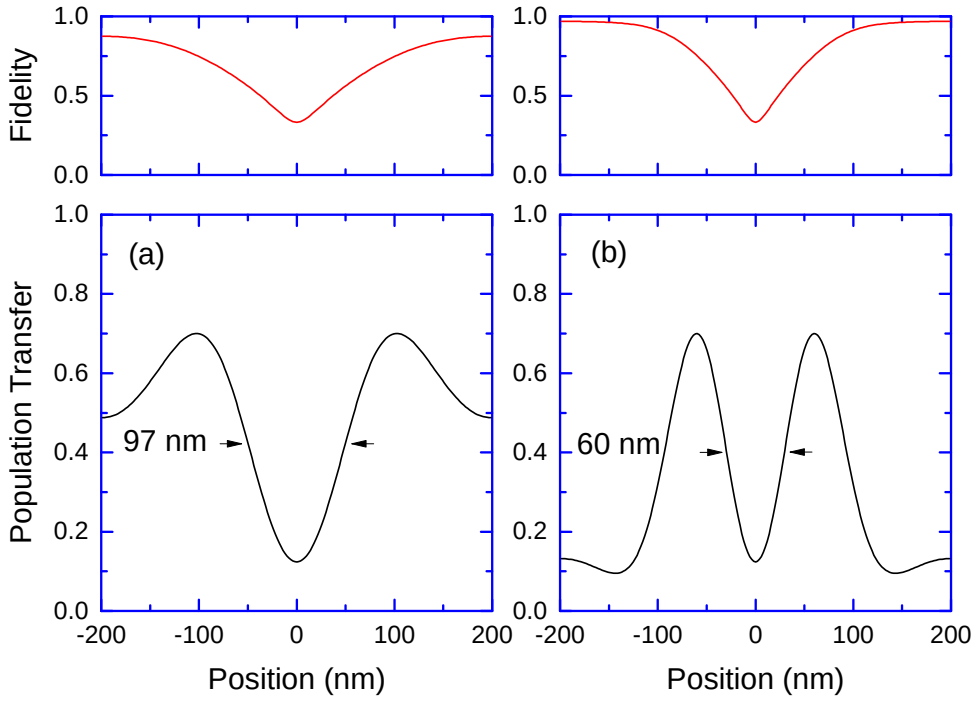

Figure 8.5 The simulated transfer to F=2 from a coupling beam standing wave with powers ranging from 0 to 3 mW in (a), and 0 to 7.5 mW in (b) plotted over one period of the standing wave. Position 0 nm corresponds to the minimum of the standing wave. These simulations produce the autocorrelation plots that agree well with the experimental data in Fig. 8.4. (b) shows a feature around 0 nm with a width of 60 nm or $\lambda/13$, a factor of 6.6 better than the diffraction limit. Plotted in red is the fidelity for the different coupling powers for different positions along the standing wave. At the nodes, the fidelity drops to 0.33 since the coupling power approaches 0.

The simulated autocorrelation data is plotted as a solid black lines in 8.4(b) and 8.4(d) and will be discussed in depth. For the 0 to 10 mW experimental data, we find the that a 0 to 3 mW simulation best matches the experimental data. The plot in figure 8.5(a) is the result of the first EIT pulse in the autocorrelation protocol over one period of the standing wave. This plot is convoluted with a Gaussian curve which simulates the diffusion of atoms during the time τ between the two EIT pulses. The resulting feature is convoluted with a second identical EIT pulse to simulate the entire autocorrelation experiment over one standing wave period. This autocorrelation simulation is plotted as a solid black line in figure 8.4(c) and 8.4(d) over multiple periods to show the repetitivity

of the experiment. The procedure was repeated for the experimental data in figure 8.4(b) with a simulated standing wave ranging from 0 to 7.5 mW plotted in figure 8.5(d). Interestingly, the main discrepancy between the experimental and simulated data is the contrast, where the simulations predict a lower contrast than the experimental data.

More importantly, both plots show very similar features that oscillate with δx. Because the autocorrelation simulations mimic the experimentally measured features, we use the single EIT pulse in figures 8.5 to conclude what underlying experimental features were created from a single EIT pulse. For the 0 to 3 mW experimental case, the middle feature of Fig. 8.5(a) has a width of 97 nm or λ/8, a factor of 4 better than the diffraction limit. The 0 to 7.5 mW plot [Fig. 8.5(b)] has a width of 60 nm or $\lambda/13.3$, a factor of 6.6 better than the diffraction limit. In these cases the measured feature is a result of atoms being transferred to F=2 in precise areas near the node of the standing wave. The middle feature are atoms left in F=1 after one EIT pulse. These results show that our experiment is sensitive enough to measure very small areas within the FORT. This result gives us a limit to what features we can see at the atomic temperatures and gives us confidence that the features are not blurring out do the motion of the standing wave during the EIT pulse.

The top plots in Fig. 8.5 shows the simulated fidelity of the system compared to the dark state. The fidelity drops to a low of 0.33 when the coupling power is at its lowest, ("0" on the horizontal axis of the plots in Fig. 8.5) at the node of the standing wave. Such low fidelities would be detrimental to quantum computing experiments since near the nodes of the standing wave the coherence has not been established. We next attempt the experiment on resonance ($\Delta\omega_p$=0) in an attempt to localize the atoms while staying in the dark state.

8.2.4 Effects of Zeeman Splitting

Because the low power off resonance data creates such distinct features, it was a good test to see if the autocorrelation experiment was working properly. One test in particular was to change the shim current, therefore changing the B field interacting with the FORT atoms, and seeing what effect that had on the experiment. The B field will raise the degeneracy of the hyperfine levels, and splitting the m_F levels by a small amount. Although the shim coils should be set up so the B field

is zero, there will probably be some small B field splitting the hyperfine levels. This was seen in section 4.7, where the best we could to suppress any stray B field still resulted in the energy levels being split by a few hundred kHz. I found that changing the B field in the direction along the probe and coupling beam made a noticeable difference in the autocorrelation data. I am convinced that the position of the atoms did not change, since there was no movement detected on the camera when any of the three shim coils were changed. The camera was sensitive to 8 μm, and any motion less than that would be negligible compared to the large sizes of the EIT beams.

The following plots in figure 8.6 shows four autocorrelation data sets for increasing shim current. The coupling beam standing wave ranged from 0 to 20 mW, with similar experimental conditions that were used to produce the data in Fig. 8.4(b). The largest number of atoms were trapped at a shim current of 4 A, while larger or smaller shim current affected the loading rate and resulted in less atoms. On average, operating at 4 A gave us approximately twice the total number of atoms. Instead of plotting the exact number of atoms in each plot, we normalize them to see how much they change over δx. There seemed to be a range of currents where the experiment worked as expected, but at 2.5 A and 5 A, the contrast was greatly reduced, and the features were much different. The features in the 4 A plot match the simulations the best, but I can't seem find a good reason that the small B field would change the features. A change of 1 A on the shims result in a magnetic field change on the order of 0.1 Gauss, meaning the m_F levels are split about 100 kHz. In the simulations, a change that small in the detuning has little effect on any of the autocorrelation data. The data was taken off resonance by 30 MHz, making any small frequency shift negligible. Maybe if the atoms were redistributed among the m_F levels between EIT pulses, but this would have to happen in time τ, only 1.5 μs. Worrying about the m_F levels prompted us to try and pump all of the population into the F=1 m_F=0 level, to avoid any problems with the B field splitting. This should also make our simulations more comparable to the data, since the atoms would only be in one m level, rather than spread between the three.

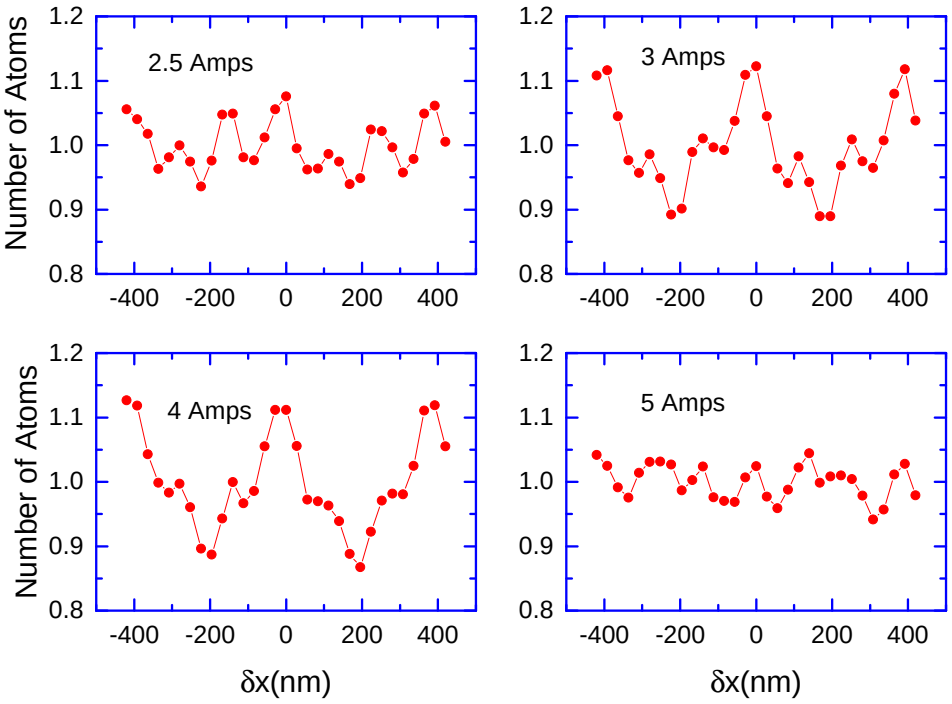

Figure 8.6 Autocorrelation data was taken for four different magnetic fields approximately parallel to the propagation of the probe beam. The data would change with the B field, possibly caused by the splitting of the energy levels.

8.2.5 m_F Level Pumping

An additional magnetic field along the path of the EIT beams splits the ground state $m_F = \pm 1$ levels approximately ∓ 3 MHz away from resonance. We use a Helmholtz configuration to produce a magnetic field up to 5 Gauss. For our configuration this requires two 50 turn coils with 15 A of current. Fig 8.7 shows the top view of our chamber and location of the Helmholtz coil. The F=2 m_F ground levels are split opposite the F=1 m_F levels, resulting in a two photon detuning ($\delta\omega$) of 6 MHz. An additional laser polarized along the magnetic field pumps the atoms from the m_F=± 1 levels into the m_F=0 level via the F′=2 excited level. The pumping laser is on resonance with the m_F=0 level, but since the $m_F \pm 1$ levels are only 6 MHz apart, the one laser can interact with either level. Figure 8.7 shows the pumping laser, $\Omega_{pumping}$, propagating perpendicular to the dipole trap

laser. We used a Glan Taylor to only allow horizontally polarized light through the chamber. We make sure not to shine the laser into the CCD camera, which is also aligned perpendicular to the B field. If any laser is hitting the camera sensor, the detector becomes saturated, and remnants of the signal would remain even when the beam is turned off. After pumping we perform the autocorrelation experiment after waiting only a few milliseconds, and remnants of the laser would remain on the camera signal. The side view of the chamber in fig 8.7 shows the configuration we use for $\Omega_{pumping}$, and how we keep the electric field oscillating along the direction of the B field. We roughly tested how effective the pumping was by looking at the transfer from one EIT pulse over different coupling frequency. More information can be found in appendix G. The magnetic field is left on while performing the EIT pulses and is uniform across the atoms.

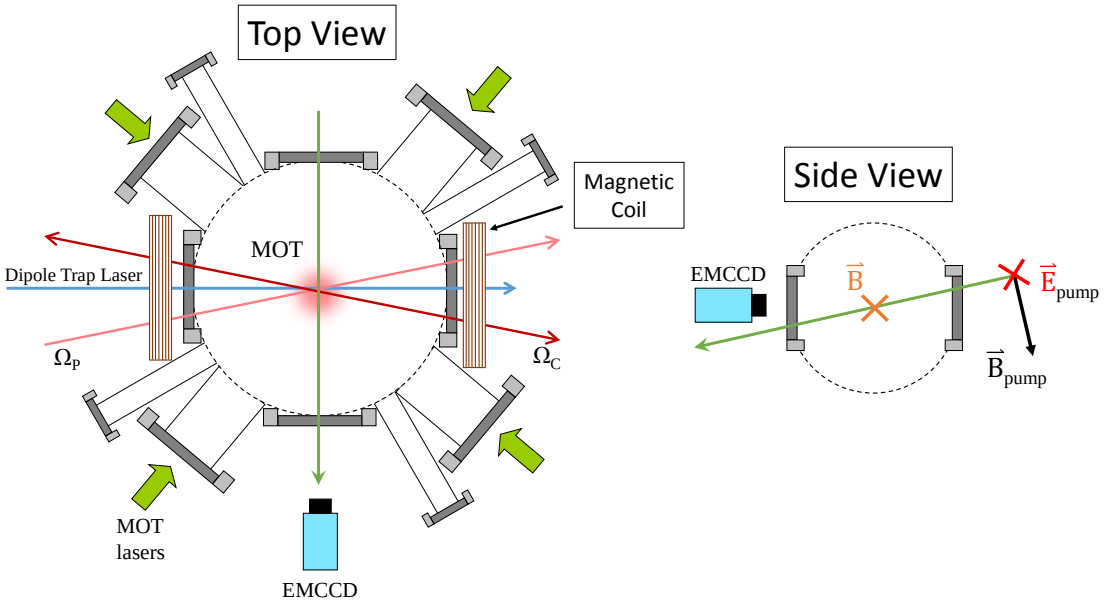

Figure 8.7 An additional pumping beam pumps atoms into the F=1 m_F=0 level via the F=1→F′=1 transition. Since the electric field is parallel to the B field, the transition F=1 m_F=0→F′=1 m_F=0 is forbidden.

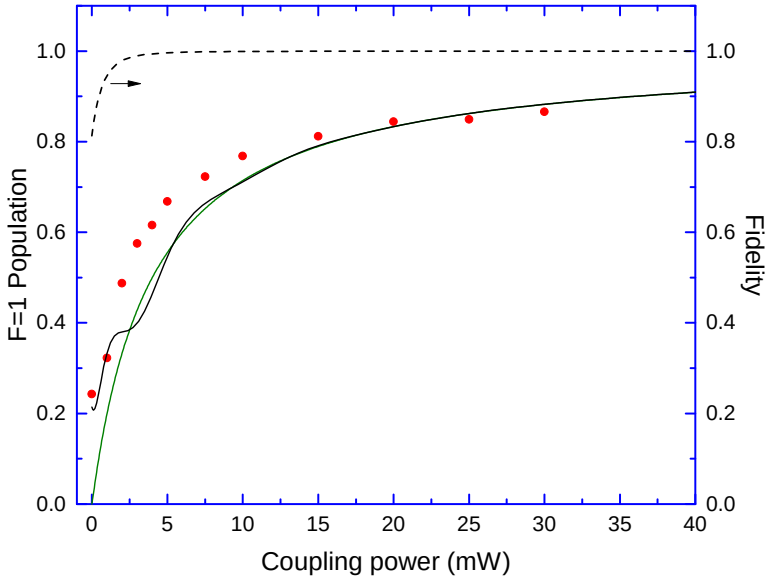

Figure 8.8 Population remaining in F=1 after one EIT pulse sequence as the coupling power is varied. The data is taken using a single coupling beam and with lasers on resonance with the excited F′=2 energy level. The solid black line is a simulation of the F=1 population using exact experimental parameters. The green line is the analytical population calculated from equation 8.1. The fidelity between the simulation and analytical curves is plotted as a dashed black line.

8.3 On Resonance Experimental Data

We now move on to explore our autocorrelation experiment when both the coupling and probe beams are on resonance with the $F' = 2$ level. Being on resonance greatly increases the atomic interaction with the probe and coupling beams and reduces the non-adiabatic corrections to the dark state. In this experiment the probe size was decreased to a $1/e^2$ radius of 0.8 mm and its power increased to 4 mW to raise the overall intensity of the probe beam. By increasing the corresponding Rabi frequency we hoped to establish the dark state quicker. The pulse width for both the coupling and probe beam were kept the same, although the rise times were increased by a factor of 2 to about 40 ns. We found that increasing the rise times of the coupling and probe powers in the simulations made the system approach the dark state faster. To avoid complications

from the three parallel m_F-level channels, we pump the atoms into the F=1 m_F=0 level using the method in section 8.2.5 and further discussed in appendix G.

8.3.1 Transfer Curver On Resonance

In Fig. 8.8, we plot the population remaining in F=1 m_F=0 as the power of the coupling laser is increased. Also plotted are the numerical simulations in black and the ideal analytical dark state solution from equation 8.1. In contrast to figure 8.2, the experimental, numerical, and analytical data show good agreement with one another. The dashed line in 8.8 is the fidelity between the numerical and analytical results and are much higher than those calculated for the off resonance case.

8.3.2 Autocorrelation Data

For the experimental on resonance autocorrelation data we chose the coupling beam powers so the minimum standing wave power was 1 mW. This assures that there is good overlap with the dark state over all points in the standing wave. The two coupling beams are set at different powers to ensure the minimum standing wave power is 1 mW. The autocorrelation data is plotted in figure 8.9 and shows data for four different ranges of the standing wave: (a) 1 mW to 10 mW (b) 1 mW to 20 mW (c) 1 mW to 40 mW and (d) 1 mW to 80 mW. The solid black lines are numerical simulations of the density matrix created from exact experimental parameters with all atoms starting in the m_F=0 F=1 ground state. Unlike the off resonance data in figure 8.4, the on resonance simulation data in figure 8.9 shows very good agreement with the contrast of the simulated data. The features created in the autocorrelation plots are not as pronounced as the off resonance plots in 8.4 because of the better overlap with the dark state (*i.e.*, the smooth nature of the transfer curve in Fig. 8.8).

Figure 8.10 shows the population transfer from one EIT pulse used to create each of the autocorrelation simulations in Fig. 8.4. These plots depict how the atoms are transferred to F=2 after one EIT pulse over one period of the coupling beam standing wave. Also plotted in Fig. 8.10 is the fidelity along one period the standing wave. As the intensity of the standing wave increases the atoms are transferred to F=2 in a smaller region. For coupling power ranging from 1 to 80 mW,

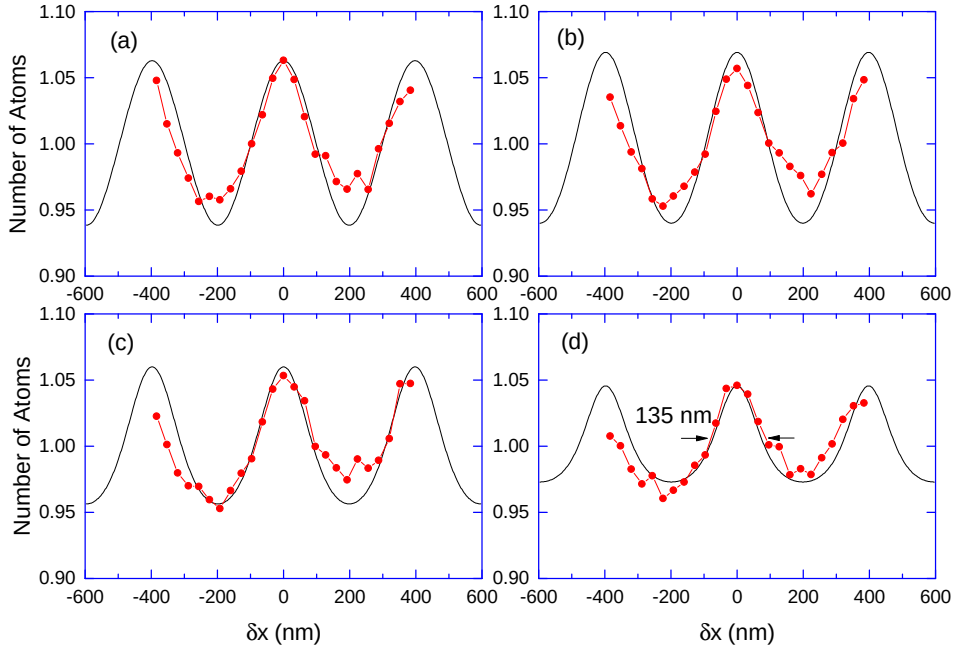

Figure 8.9 Experimental autocorrelation data for four different ranges of standing wave power: (a) 1 mW to 10 mW (b) 1 mW to 20 mW (c) 1 mW to 40 mW and (d) 1 mW to 80 mW. The black lines are numerical simulations of the density matrix using exact experimental parameters. Each simulated plot was created using the autocorrelation protocol in appendix H using the data in Fig. 8.10

.

figure 8.10(d) shows that the transfer is localized to a region with a width of 70 nm, a factor of 11.3 times smaller than the wavelength of the coupling and probe beams. This transfer was performed with a fidelity of over 0.94 over all points of the standing wave, much higher than the fidelity of the off resonance data in figure 8.5.

8.4 Uncertainty Limit

This section will discuss a fundamental limit to the size of localization that we can measure using our autocorrelation technique. The technique relies on very cold atoms over a time scale of about 1.5 μs, the time between EIT pulses. It is important that the atoms move very little over

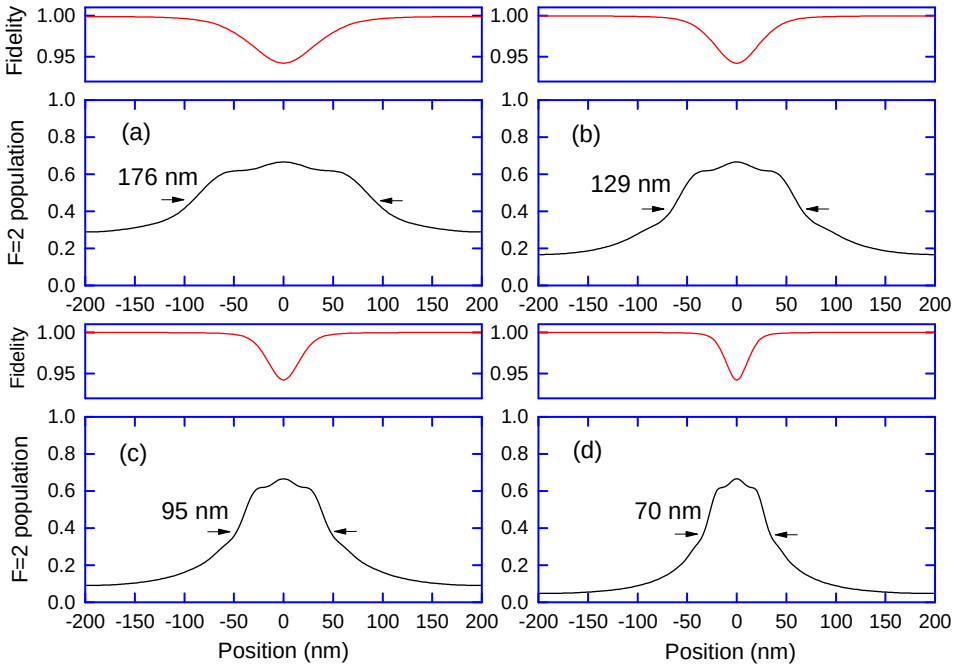

Figure 8.10 Population transfer to F=2 as a function of position in the standing wave for the same power ranges as Fig. 8.9 :(a) 1 mW to 10 mW (b) 1 mW to 20 mW (c) 1 mW to 40 mW and (d) 1 mW to 80 mW. Each plot is simulated using one EIT pulse and is plotted over one period of the standing wave. On the horizontal axis,"0" is the position where the standing wave minimum occurs. These simulations create the autocorrelation plots in Fig. 8.9. Figure (d) shows transfer to a region with FWHM of 70 nm, which is a factor of 11.3 times smaller than the wavelength of the probe and coupling beams. The top plots in red are the fidelity across the standing wave for each case. The minimum fidelity is 0.94, with increasing fidelity for area further from the standing wave node.

this period so they are in the same position for the each EIT pulse. After performing the first EIT pulse the atoms are in a superposition of F=1 and F=2. When we heat the atoms with $\Omega_{blow-away}$ we are making a measurement on the atoms in F=2, and this collapses the wave function. Once this happens, the atoms in F=1 are also measured, and their probability distribution can be very small. By performing this measurement, the momentum, and therefore velocity, will be subject to the uncertainty limit. If this imposes a very large momentum spread on the atoms, they will move

too much before the second EIT pulse, blurring out any features created by the first pulse. At first glance, it may seem like we our violating the uncertainty principle if we use the simple equation

$$\sigma_x \sigma_p \geq \hbar/2 \tag{8.2}$$

In our previous simulated and experimental data, we used values representing the FWHM for each feature. Equation 8.2 uses σ, a factor of 2.355 smaller than the FWHM. This gives our narrowest measured FWHM data of 60 nm a σ_x=25.48 nm. Given σ_x, we calculate that σ_v=14.34 nm/μs, larger than the velocity spread we used in our simulations, 12 nm/μs. If this were true, that would mean that we are not observing the uncertainty principle in our experiment.

Equation 8.2 assumes both functions are Gaussian, which is the not the case for our experiment. To more accurately calculate the uncertainty in velocity, we take a Fourier transform of the position wave function. Following the work of Agarwal [48], we model the momentum distribution over two periods of the standing wave using

$$\mathscr{P}_2(p) = |\langle p, F=2|\Psi_{dark}\rangle|^2 = \left| \int_{-\pi}^{\pi} \sqrt{\rho_{22}(x)} e^{ipx} dx \right|^2 \tag{8.3}$$

where $\rho_{22}(x)$ is the population of F=2 along the standing wave. For a Gaussian distribution the above equation yields the familiar uncertainty principle in equation 8.2. For simplicity, we used $\rho_{22}(x)$ from the analytical solution to the dark state,

$$\rho_{22}(x) = \frac{1}{1 + \frac{|\Omega_c|^2}{|\Omega_p|^2} \sin^2(\pi x/795nm)} \tag{8.4}$$

Fig. 8.11 is a plot of $\rho_{22}(x)$ with a FWHM of 60 nm. Using this in equation 8.3 we find the momentum distribution and plot the velocity distribution in Fig. 8.12.

Figure 8.12 shows velocities that begin to appear away from the center velocity. Along side the calculated velocity spread we plotted the velocity spread that we used for the atoms, a Maxwell Boltzmann distribution function with the most probably velocity v_p =12 nm/μs. More information about the velocity of the atoms is discussed in appendix H.2. I was not concerned with the magnitude of equation 8.3, only the relative spread in velocity. Fig. 8.12 shows that our velocity

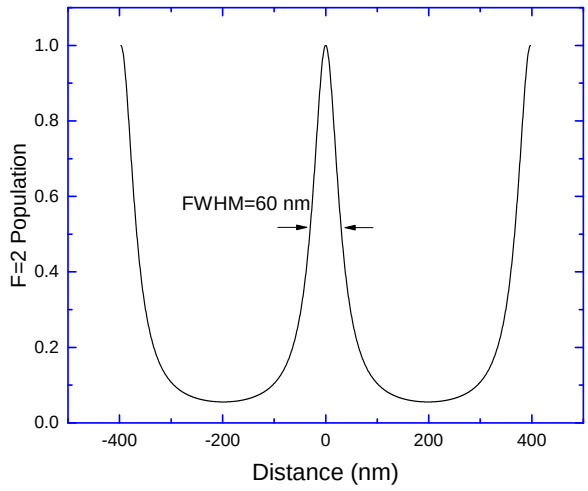

Figure 8.11 $\rho_{22}(x)$ plotted against the position of the standing wave. The values of Ω_c and Ω_p were chosen so that the middle features has a FWHM of 60 nm.

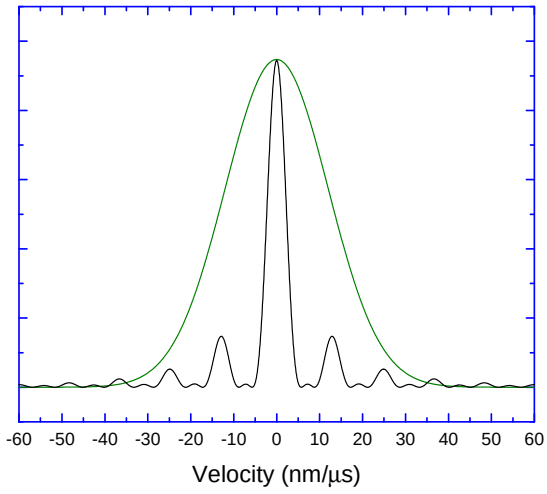

Figure 8.12 The black line is the velocity uncertainty calculated from equation 8.3 using the $\rho_{22}(x)$ values from Fig. 8.11. The green line is a Maxwell-Boltzmann distribution with a most probable velocity of v_p=12 nm/μs. Since the velocity uncertainty lies within the Maxwell-Boltzmann distribution we are confident that we not uncertainty limit at 60 nm.

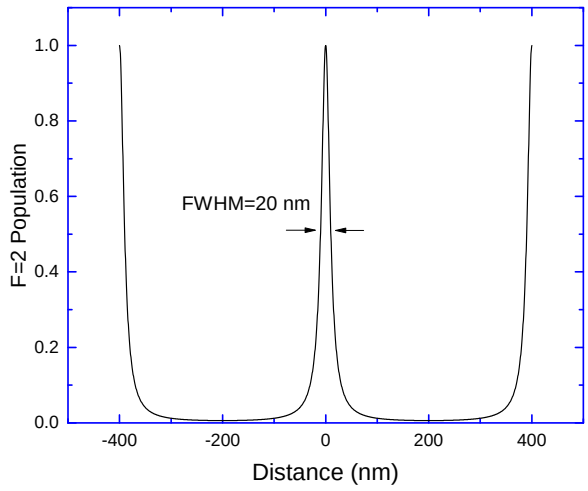

Figure 8.13 $\rho_{22}(x)$ plotted against the position of the standing wave. The values of Ω_c and Ω_p were chosen so that the middle features has a FWHM of 20 nm.

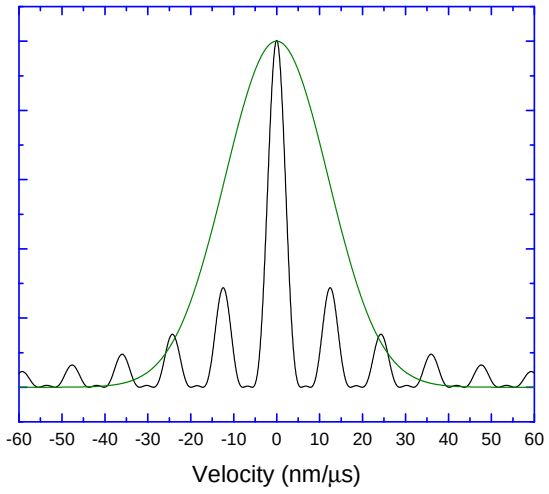

Figure 8.14 The black line is the velocity uncertainty calculated from equation 8.3 using the $\rho_{22}(x)$ values from Fig. 8.13. The green line is a Maxwell-Boltzmann distribution with a most probable velocity of v_p=12 nm/μs. The velocity uncertainty because extend further than the Maxwell-Boltzmann distribution. Features smaller than 20 nm would not observed because the induced velocity spread would be too large.

of 12 nm/μs does not violate the momentum spread imposed on the atoms due to the uncertainty principle. The velocity distribution we use is much larger than the induced momentum spread.

Since our experiment is dependent on the blow away beam and the time τ to heat the atoms, our set up is uncertainty limited. We wanted to get an idea of the lowest feature that would be possible to see using our current set up. At 20 nm, the features created by equation 8.2 begin to expand further than the initial temperature of the atoms. Figure 8.13 is a plot of $\rho_{22}(x)$ with a FHWM of 20 nm. The velocity spread for this case is plotted in Fig. 8.14. Components of the velocity begin to appear at higher velocities than the distribution we used in the simulations. At this point the atoms have spread too much during τ, and will begin to blur out features that were made by the first EIT pulse. At features smaller than 20 nm, the spread increases, making it difficult to properly detect smaller regions. This would be the case even if the atoms were initially at 0 K. For all of our simulations we ignore the momentum spread induced by the uncertainty limit. I only integrate over two periods in the Fourier transform, but it gives a good general idea of the momentum spread for increasingly narrow transfer. The uncertainty limit sets the smallest feature size at 20 nm. For future experiments, demonstrating features smaller than this would require a substantially different protocol.

8.5 Conclusion

We experimentally transferred atoms between the hyperfine levels of ^{87}Rb atoms within a spatial period of 70 nm. This width was a factor of 11.3 times smaller than the wavelength of light used to perform the transfer. For this case, the overlap with the dark state was over 0.94 for all points along the standing wave. We also inferred features as small as 60 nm, but for this case the overlap with the dark state was poor.

Chapter 9

Suppression of Inhomogeneous Broadening

9.1 Introduction

This chapter is independent of the localization work discussed in the rest of this thesis. The majority of this chapter is a summary of our paper [59], while section 9.4 provides some additional information. The main idea of the work is to eliminate the effects of Doppler broadening using stark shifts. When atoms are heated, their velocities cause Doppler shifts in respect to an incoming laser beam. The atomic resonance of the atoms with respect to the laser changes with the velocity of the atoms, effecting the susceptibility of the atomic medium. This is a problem since it would be better if all the atoms would react the exact same way to an incident laser.

9.2 Theory of Line Suppression with Stark Shifts

Fig. 9.1 is the energy level scheme we use to suppress Doppler broadening. A weak probe beam (E_p) is on resonance with the ground state ($|1\rangle$) and state $|2\rangle$ within atoms at different velocities. Due to the atomic motion, this transition is Doppler broadened and we try to suppress this broadening with an additional laser. The stark shifting laser (E_s) will stark shift the ground state with respect to the energy levels $|3\rangle$ and $|4\rangle$. If we correctly stark shift the ground state to counteract the Doppler shift, the Doppler width should be reduced. The Rabi frequencies of the stark shift laser are $\Omega_{13} = E_s\mu_{13}/\hbar$ and $\Omega_{14} = E_s\mu_{14}/\hbar$, where μ_{13} and μ_{14} are the dipole matrix elements of each transition. The stark shift of $|1\rangle$ is equal to

$$\delta_{stark-shift} = \frac{|\ \Omega_{13}\ |^2}{4\Delta_{13}} + \frac{|\ \Omega_{14}\ |^2}{4\Delta_{14}} \tag{9.1}$$

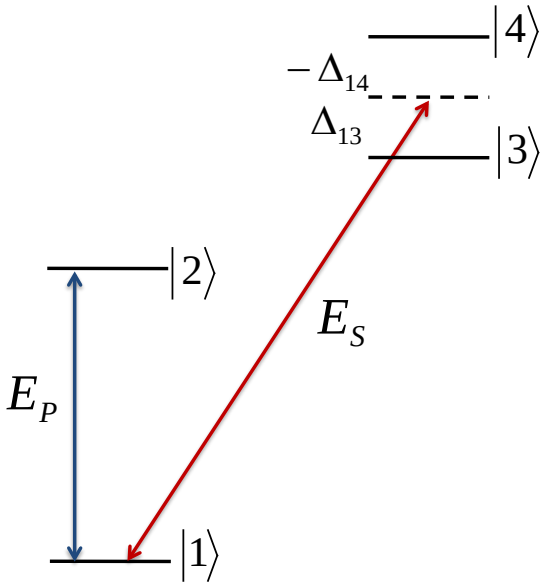

Figure 9.1 Energy level scheme for suppressing Doppler broadening of the $|1\rangle \rightarrow |2\rangle$ transition. All atoms are initially in the $|1\rangle$ state and assumes that the population varies very little while the probe (E_P) and Stark-shift (E_S) lasers are on. Any motion of the atoms will cause the frequencies of E_P and E_S to be Doppler shifted, changing the detunings Δ_{14} and Δ_{13}. With appropriately chosen conditions, E_S will Stark shift the ground state to compensate for the Doppler shift of E_P.

where the detunings are $\Delta_{13} = \omega_s - (\omega_3 - \omega_1)$ and $\Delta_{14} = \omega_s - (\omega_4 - \omega_1)$. We choose the frequency of the stark shifting laser so that for an atom at rest Δ_{14}=-Δ_{13}. We also assume that the matrix elements for both transitions are equal to one another. For an atom moving at velocity v in the direction of the probe beam, the frequency of the probe beam is Doppler shifted by $k_p v$, where k_p=ω_p/c. We want to correct this shift by using $\delta_{stark-shift}$. We assume the stark shift laser is propagating along the same direction as the probe beam. This Doppler shift will also change the detunings used in $\delta_{stark-shift}$ by an amount $k_s v$. By setting the Doppler shift and $\delta_{stark-shift}$ equal to each other, we arrive at the following condition

$$\frac{k_p}{k_s} = \frac{|\,\Omega_{14}\,|^2}{2\Delta_{14}^2} \tag{9.2}$$

Equation 9.2 is derived assuming that the majority of the population stays in $|1\rangle$. For this to work, $k_s \neq k_p$, or a large amount of the atomic population would be moved from $|1\rangle$. We

numerically solve the density matrix of the four level scheme to find the best parameters that suppress the Doppler broadening.

9.3 Numerical Parameters

We solve the density matrix using the following parameters. The three upper levels can all decay to the ground state $|1\rangle$ but are forbidden to decay into one another. This sets Γ_2=Γ_3=$\Gamma_4 \equiv \Gamma$, where we set Γ=$2\pi\times5$ MHz. The probe laser needs to be weak so that a majority of the population remains in $|1\rangle$, so Ω_p=$\Gamma/100$. The Stark shift laser had to be a much stronger laser power, to accurately stark shift the levels. We found that Ω_{14}=810Γ gave us the best line suppression for the other parameters we used. The stark laser detunings are Δ_{13}=1000Γ and Δ_{14}=-1000Γ. We also choose k_s=$4k_p$, making the wavelength of the stark shifting laser 4 times less than the probe beam. We introduce Doppler broadening into the simulations assuming a Doppler width of $\Delta\omega_{doppler} = 2\pi \times 250MHz$, much larger than the homogeneous line width of Γ=$2\pi\times5$ MHz. Using these parameters we plot the Doppler-averaged line shape, $|\langle\rho_{12}\rangle_{Doppler}|$, in Fig. 9.2. With no stark beam, the coherence is non-zero over a broad range of frequencies because of the Doppler broadening. The max coherence in this case is 1.25×10^{-4}. With the stark beam on, the coherence increases to 4.1×10^{-3}, only a factor of 2.5 lower than the peak coherence if no Doppler broadening was present.

9.4 Experimental Set Up

The numbers we used gave us the best suppression in the density matrix simulations. What I will go through now is an experimental set that is similar to some of these parameters. First we need to find an atomic system that matches the frequency conditions. Mainly, we look for transition that satisfy k_s=$4k_p$. We first looked at alkali earth metals such as ^{87}Rb. Although there are strong transitions at 780 nm and 795 nm, there are not many transitions in the ultraviolet that couple to the ground state. Any transition that does has a very weak matrix element, greatly reducing the

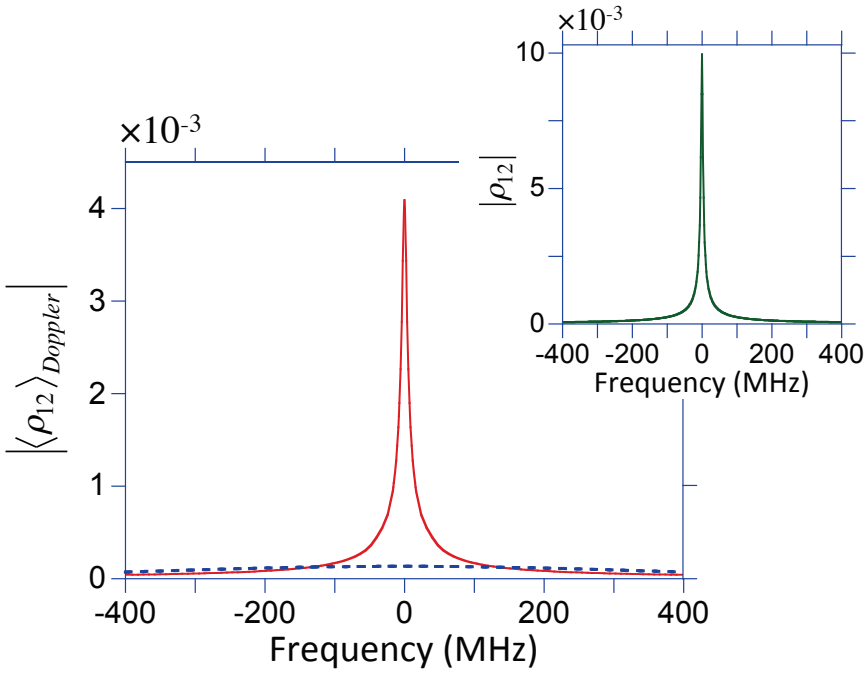

Figure 9.2 Doppler-averaged coherence between levels $|1\rangle$ and $|2\rangle$ as the frequency of the probe laser is scanned across resonance with (solid red line) and without (dashed blue line) the stark shift laser. With no stark shift laser, the coherence is Doppler broadened with a peak of 1.25×10^{-4}. With the Stark shift laser, the width of the coherence is closer to its homogeneous width with a peak coherence of 4.1×10^{-3}. For comparison, the inset shows the homogeneous line width with no Doppler broadening and no Stark shift laser. The peak coherence for this case is 1×10^{-2}.

Rabi frequency. If the matrix element is very weak, the stark shifting laser power would have to be prohibitively large for the suppression to occur.

9.4.1 Metastable Helium

The lower state $|1\rangle$ has been assumed to be a ground state, but as long the level has a very slow decay rate in comparison to the other levels, the experiment will still work. I started looking at metastable atoms and I think that metastable helium atoms would work well to show line suppression. Metastables are in an excited state, but are forbidden to decay into the ground state, resulting in very long lifetimes.

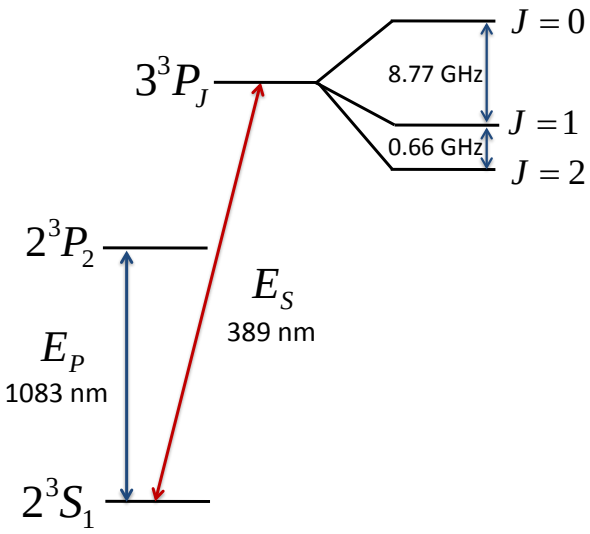

Figure 9.3 Energy level scheme of Helium that could be used for line suppression. The 2^3S_1 level is a metastable level that couples very well to different excited state. The two lasers give k_S=2.78k_P, which is enough to see some line suppression. The excited P triplet has energy levels approaching 10 GHz apart, similar to what was used in the simulations. More work is needed to pick the exact 4 levels to use since each level pictured here also has hyperfine levels that can further complicate the energy diagram.

Fig. 9.3 is the energy diagram with the helium energy levels that could be used to demonstrate line suppression. The lowest level is the 1s2s $^3S_1$ metastable state. This level has a lifetime of 8000 seconds, much larger than the decay rates of the other three levels [60]. The excited state $|2\rangle$ is the 1s2p $^3P_2$, making the laser wavelength that is resonant between $|1\rangle$ and $|2\rangle$ equal to 1083 nm. States $|3\rangle$ and $|4\rangle$ can be two levels within the triplet P level of the 1s3p energy level. Each fine level is split into hyperfine levels that can have similar energy differences to the fine structure splitting. The stark shift laser would be 389 nm to couple these two levels to the metastable state. This sets k_s=2.78k_p, and although is not the ideal multiple of 4, should be enough to see some line suppression. For the simulations we used Δ_{41}=2$\pi\times$ 5GHz and Δ_{31}=-2$\pi\times$ 5GHz, meaning the two excited states are 10 GHz away from each other. The excited state helium levels are separated by 8.77 GHz, close to what was used in the numerical simulations. Some work will still need to be

done in deciding what levels to use, since each fine structure energy level can be split into multiple hyperfine levels, which adds another level of complexity to the experiment [61].

More importantly, the stark shift energy levels have large decay rates, and therefore will have large dipole matrix elements. The decay rates are very similar to one another, around Γ=2$\pi\times$1.6 MHz. Less than what was used in the simulations but they are all very similar. The dipole matrix element is dependent on the decay rate, and needs to be relatively high so that Ω_{14} and Ω_{13} can be large without needing very high intensity lasers.

9.4.2 Previous Work

Previous groups have utilized the long lived excited state to create MOT's with metastable Helium, using either the 389 nm or 1083 nm laser as the MOT beams [62, 63, 64]. This is encouraging since we will need both lasers to be fairly stable to see line suppression. Other work has been done in metastable helium that will make our line suppression experiment easier. Similar to Rb, we can use a saturated absorption lock technique to stabilize the 389 nm laser to be accurately detuned from the energy levels $|3\rangle$ and $|4\rangle$. A second harmonic generation (SHG) set up using 778 nm light should be able to get enough ultra violet light to see the line suppression. What's really nice about this is that our work in the D_2 line of ^{87}Rb was at 780 nm, so we have the appropriate equipment to get approximately 2 Watts of optical power at 780 nm. Koelemeij et. al. have produced 1 Watt of 389 nm light from a SHG cavity using 2 W of 789 nm [65]. They lock the output to an RF discharge cell and achieve a locked laser width of 15-25 MHz. Although larger than the natural linewidth of the transition, this should still work fine for our proposed experiment since this laser is several GHz away from any transition.

9.5 Conclusion

We propose a technique to suppress Doppler broadening using the Stark shift. For appropriate conditions, the Stark shift can correct for the Doppler broadening, greatly increasing the coherence. The exact conditions for this occur strongly depends on the energy levels of the atoms. The helium

metastable state has the appropriate levels that suppression should occur, but more work still needs to be done before constructing an experimental set up.

REFERENCES

[1] Stephen E. Harris. Electromagnetically Induced Transparency. *Physics Today*, 50(7):36, 1997.

[2] Marlan Orvil Scully and Muhammad Suhail Zubairy. *Quantum optics*. Cambridge University Press, Cambridge, England, 1997.

[3] O Kocharovskaya. Amplification and lasing without inversion, 1992.

[4] Michael Fleischhauer, Atac Imamoglu, and Jonathan Marangos. Electromagnetically induced transparency: Optics in coherent media. *Reviews of Modern Physics*, 77(2):633–673, July 2005.

[5] T. Wilk, A. Gaëtan, C. Evellin, J. Wolters, Y. Miroshnychenko, P. Grangier, and A. Browaeys. Entanglement of two individual neutral atoms using rydberg blockade. *Physical Review Letters*, 104(1), 2010.

[6] L. Isenhower, E. Urban, X. L. Zhang, A. T. Gill, T. Henage, T. A. Johnson, T. G. Walker, and M. Saffman. Demonstration of a neutral atom controlled-nOT quantum gate. *Physical Review Letters*, 104(1), 2010.

[7] C. Monroe, D. Meekhof, B. King, W. Itano, and D. Wineland. Demonstration of a Fundamental Quantum Logic Gate, 1995.

[8] J. Cirac and P. Zoller. Quantum Computations with Cold Trapped Ions, 1995.

[9] Michael A. Nielsen and Isaac L. Chuang. *Quantum Computation and Quantum Information: 10th Anniversary Edition*. 2011.

[10] Stefan W Hell. Far-Field Optical Nanoscopy. *Science*, 316(5828):1153–1158, 2007.

[11] J. Gardner, M. Marable, G. Welch, and J. Thomas. Suboptical wavelength position measurement of moving atoms using optical fields, 1993.

[12] J E Thomas. Uncertainty-limited position measurement of moving atoms using optical fields. *Optics letters*, 14(21):1186–1188, 1989.

[13] U. Dürig, D. W. Pohl, and F. Rohner. Near-field optical-scanning microscopy. *Journal of Applied Physics*, 59(10):3318–3327, 1986.

[14] D. W. Pohl, W. Denk, and M. Lanz. Optical stethoscopy: Image recording with resolution $\lambda/20$. *Applied Physics Letters*, 44(7):651, 1984.

[15] K Bergmann, H Theuer, and B W Shore. Coherent population transfer among quantum states of atoms and molecules. *Rev. Mod. Phys.*, 70:1003–1023, 1998.

[16] Lene Vestergaard Hau, S. E. Harris, Zachary Dutton, and Cyrus H. Behroozi. Light speed reduction to 17 metres per second in an ultracold atomic gas. *Nature*, 397(6720):594–598, 1999.

[17] A. Kasapi, Maneesh Jain, G. Yin, and S. Harris. Electromagnetically Induced Transparency: Propagation Dynamics, 1995.

[18] Min Xiao, Yong-qing Li, Shao-zheng Jin, and Julio Gea-Banacloche. Measurement of Dispersive Properties of Electromagnetically Induced Transparency in Rubidium Atoms, 1995.

[19] Michael M. Kash, Vladimir A. Sautenkov, Alexander S. Zibrov, L. Hollberg, George R. Welch, Mikhail D. Lukin, Yuri Rostovtsev, Edward S. Fry, and Marlan O. Scully. Ultraslow Group Velocity and Enhanced Nonlinear Optical Effects in a Coherently Driven Hot Atomic Gas. *Physical Review Letters*, 82(26):5229–5232, June 1999.

[20] Julio Gea-Banacloche, Yong-qing Li, Shao-zheng Jin, and Min Xiao. Electromagnetically induced transparency in ladder-type inhomogeneously broadened media: Theory and experiment, 1995.

[21] Nathaniel B. Phillips, Alexey V. Gorshkov, and Irina Novikova. Optimal light storage in atomic vapor. *Physical Review A - Atomic, Molecular, and Optical Physics*, 78(2), 2008.

[22] Irina Novikova, Alexey V. Gorshkov, David F. Phillips, Anders S. Sø rensen, Mikhail D. Lukin, and Ronald L. Walsworth. Optimal control of light pulse storage and retrieval. *Physical Review Letters*, 98(24), 2007.

[23] George M Gehring, Aaron Schweinsberg, Christopher Barsi, Natalie Kostinski, and Robert W Boyd. Observation of backward pulse propagation through a medium with a negative group velocity. *Science (New York, N.Y.)*, 312(5775):895–897, 2006.

[24] M. Fleischhauer and M. Lukin. Quantum memory for photons: Dark-state polaritons, 2002.

[25] D. F. Phillips, A. Fleischhauer, A. Mair, R. L. Walsworth, and M. D. Lukin. Storage of light in atomic vapor. *Physical Review Letters*, 86(5):783–786, 2001.

[26] C Liu, Z Dutton, C H Behroozi, and L V Hau. Observation of coherent optical information storage in an atomic medium using halted light pulses. *Nature*, 409(6819):490–493, 2001.

[27] H Schmidt and A Imamogdlu. Giant Kerr nonlinearities obtained by electromagnetically induced transparency. *Optics letters*, 21(23):1936–1938, 1996.

[28] a. Imamolu, a. Imamolu, H. Schmidt, H. Schmidt, G. Woods, G. Woods, M. Deutsch, and M. Deutsch. Strongly Interacting Photons in a Nonlinear Cavity. *Physical Review Letters*, 79(8):1467–1470, 1997.

[29] S. Harris and Y. Yamamoto. Photon Switching by Quantum Interference, 1998.

[30] M. D. Lukin and A. Imamolu. Nonlinear Optics and Quantum Entanglement of Ultraslow Single Photons. *Physical Review Letters*, 84(7):1419–1422, February 2000.

[31] Hai Wang, David Goorskey, and Min Xiao. Enhanced Kerr Nonlinearity via Atomic Coherence in a Three-Level Atomic System. *Physical Review Letters*, 87(7):073601, July 2001.

[32] Hoonsoo Kang and Yifu Zhu. Observation of Large Kerr Nonlinearity at Low Light Intensities. *Physical Review Letters*, 91(9):093601, August 2003.

[33] Z. J. Simmons, N. A. Proite, J. Miles, D. E. Sikes, and D. D. Yavuz. Refractive index enhancement with vanishing absorption in short, high-density vapor cells. *Physical Review A*, 85(5):053810, May 2012.

[34] N. A. Proite, B. E. Unks, J. T. Green, and D. D. Yavuz. Refractive Index Enhancement with Vanishing Absorption in an Atomic Vapor. *Physical Review Letters*, 101(14):147401, September 2008.

[35] N. A. Proite, Z. J. Simmons, and D. D. Yavuz. Observation of atomic localization using electromagnetically induced transparency. *Physical Review A*, 83(4):041803, April 2011.

[36] P. Metcalf, H.J. and Van der Straten. *Laser Cooling and Trapping*. Springer, New York, 1999.

[37] C. J. Hawthorn, K. P. Weber, and R. E. Scholten. Littrow configuration tunable external cavity diode laser with fixed direction output beam. *Review of Scientific Instruments*, 72(12):4477–4479, 2001.

[38] Daryl W. Preston. Doppler-free saturated absorption: Laser spectroscopy. *American Journal of Physics*, 64(11):1432, 1996.

[39] Daniel A. Steck. Rubidium 87 D Line Data. available here: http://steck.us/alkalidata/rubidium87numbers.1.6.pdf.

[40] R Newell, J Sebby, and T G Walker. Dense atom clouds in a holographic atom trap. *Optics letters*, 28(14):1266–1268, 2003.

[41] M. D. Barrett, J. A. Sauer, and M. S. Chapman. All-Optical Formation of an Atomic Bose-Einstein Condensate. *Physical Review Letters*, 87(1):010404, June 2001.

[42] J. Dalibard and C. Cohen-Tannoudji. Laser cooling below the Doppler limit by polarization gradients: simple theoretical models, 1989.

[43] Paul D. Lett, Richard N. Watts, Christoph I. Westbrook, William D. Phillips, Phillip L. Gould, and Harold J. Metcalf. Observation of atoms laser cooled below the doppler limit. *Physical Review Letters*, 61(2):169–172, 1988.

[44] M. Drewsen, Ph Laurent, A. Nadir, G. Santarelli, A. Clairon, Y. Castin, D. Grison, and C. Salomon. Investigation of sub-Doppler cooling effects in a cesium magneto-optical trap. *Applied Physics B Lasers and Optics*, 59(3):283–298, 1994.

[45] S. J. M. Kuppens, K. L. Corwin, K. W. Miller, T. E. Chupp, and C. E. Wieman. Loading an optical dipole trap, 2000.

[46] B E Unks, N A Proite, and D D Yavuz. Generation of high-power laser light with Gigahertz splitting. *The Review of scientific instruments*, 78(8):083108, August 2007.

[47] E. A. Donley, T. P. Heavner, F. Levi, M. O. Tataw, and S. R. Jefferts. Double-pass acousto-optic modulator system. *Review of Scientific Instruments*, 76(6):063112, 2005.

[48] Girish S. Agarwal and Kishore T. Kapale. Sub-wavelength atom localization via coherent population trapping. *J. Phys. B: At. Mol. Opt. Phys.*, 3437(39):6, 2006.

[49] D. D. Yavuz and N. A. Proite. Nanoscale resolution fluorescence microscopy using electromagnetically induced transparency. *Physical Review A*, 76(4):041802, October 2007.

[50] Alexey V. Gorshkov, Liang Jiang, Markus Greiner, Peter Zoller, and Mikhail D. Lukin. Coherent Quantum Optical Control with Subwavelength Resolution. *Physical Review Letters*, 100(9):093005, March 2008.

[51] J. Choi and D. S. Elliott. Influence of interaction time and population redistribution on the localization of atomic excitation through electromagnetically induced transparency. *Physical Review A*, 89(1):013414, January 2014.

[52] Wolfgang Alt, Dominik Schrader, Stefan Kuhr, Martin Müller, Victor Gomer, and Dieter Meschede. Single atoms in a standing-wave dipole trap. *Physical Review A*, 67(3):033403, March 2003.

[53] J. A. Armstrong. Measurement of picosecond laser pulse widths. *Applied Physics Letters*, 10(1):16–18, 1967.

[54] Andrejs Vorozcovs, Matthew Weel, Scott Beattie, Saviour Cauchi, and A. Kumarakrishnan. Measurements of temperature scaling laws in an optically dense magneto-optical trap, 2005.

[55] Wolfgang Ketterle and N.J. Van Druten. Evaporative cooling of trapped atoms. *Advances In Atomic, Molecular, and Optical Physics*, 37:181–236, 1996.

[56] K Bergmann, H Theuer, and B W Shore. Coherent population transfer among quantum states of atoms and molecules. *Rev. Mod. Phys.*, 70:1003–1023, 1998.

[57] Daniel A. Steck. Quantum and Atom Optics. a, available online at http://steck.us/teaching (revision 0.10.1, 30 April 2015).

[58] R Grimm, M Weidemüller, and Y Ovchinnikov. Optical dipole trap for neutral atoms. *Adv. At. Mol. Opt. Phys.*, 42:95, 2000.

[59] D. D. Yavuz, N. R. Brewer, J. A. Miles, and Z. J. Simmons. Suppression of inhomogeneous broadening using the ac Stark shift. *Physical Review A*, 88(6):063836, December 2013.

[60] S. S. Hodgman, R. G. Dall, L. J. Byron, K. G H Baldwin, S. J. Buckman, and A. G. Truscott. Metastable helium: A new determination of the longest atomic excited-state lifetime. *Physical Review Letters*, 103(5), 2009.

[61] I A Sulai, Qixue Wu, M Bishof, G W F Drake, Z-T Lu, P Mueller, and R Santra. Hyperfine suppression of 2 3 S 1–3 3 P J transitions in 3He. *Physical review letters*, 101(17):173001, 2008.

[62] R P Bertram, M SUGANUMA, H Merimeche, P J J Tol, M Mutzel, T KONDOW, H Metcalf, N Herschbach, D Haubrich, U MIZUTANI, D Meschede, E A Hessels, P Rosenbusch, P Verkerk, E A Hinds, and D Hennequin. Large numbers of cold metastable helium atoms in a magneto-optical trap. *arXiv*, 60(2):R761–R764, 1999.

[63] Michael Keller, Mateusz Kotyrba, Florian Leupold, Mandip Singh, Maximilian Ebner, and Anton Zeilinger. A Bose-Einstein condensate of metastable helium for quantum correlation experiments. *arXiv*, (Dld):9, 2014.

[64] J. C. J. Koelemeij, R. J. W. Stas, W. Hogervorst, and W. Vassen. Magneto-optical trap for metastable helium at 389 nm. *Physical Review A*, 67(5):053406, May 2003.

[65] J. C J Koelemeij, W. Hogervorst, and W. Vassen. High-power frequency-stabilized laser for laser cooling of metastable helium at 389 nm. *Review of Scientific Instruments*, 76(3), 2005.

Appendix A: Solve Hamiltonian

I'll go through in more detail how we go from equation 3.11 to equation 3.13. We use a unitary matrix to transform the original Hamiltonian in to one with no oscillating terms. Using the Schrodinger equation and notes from Steck [57] we define the transformed Hamiltonian as

$$H_{transform} = UHU^{\dagger} + i\hbar U\frac{\partial U^{\dagger}}{\partial t} \tag{A.1}$$

where U is the arbitrary unitary matrix

$$U = \begin{bmatrix} e^{-i\omega_x t} & 0 & 0 \\ 0 & e^{-i\omega_y t} & 0 \\ 0 & 0 & e^{-i\omega_z t} \end{bmatrix} \tag{A.2}$$

and the Hamiltonian before transformation is

$$H = \begin{bmatrix} \hbar\omega_1 & 0 & -\frac{\mu_{1e}E_p}{2}(e^{i\omega_p t} + e^{-i\omega_p t}) \\ 0 & \hbar\omega_2 & -\frac{\mu_{2e}E_p}{2}(e^{i\omega_c t} + e^{-i\omega_c t}) \\ -\frac{\mu_{e1}E_p}{2}(e^{i\omega_p t} + e^{-i\omega_p t}) & -\frac{\mu_{e2}E_p}{2}(e^{i\omega_c t} + e^{-i\omega_c t}) & \hbar\omega_e \end{bmatrix} \tag{A.3}$$

which is identical to 3.11 but with the electric fields written out in terms of their amplitudes and oscillating terms using Equations A.4 and A.5.

$$\vec{E_p} = E_p\frac{e^{i\omega_p t} + e^{-i\omega_p t}}{2} \tag{A.4}$$

$$\vec{E_c} = E_c\frac{e^{i\omega_c t} + e^{-i\omega_c t}}{2} \tag{A.5}$$

The first term of equation A.1 is

$$UHU^{\dagger} = \hbar\begin{bmatrix} \omega_1 & 0 & -\frac{\Omega_p}{2}e^{i(\omega_z-\omega_1)t}(e^{i\omega_p t} + e^{-i\omega_p t}) \\ 0 & \omega_2 & -\frac{\Omega_c}{2}e^{i(\omega_y-\omega_2)t}(e^{i\omega_c t} + e^{-i\omega_c t}) \\ -\frac{\Omega_p}{2}e^{i(\omega_1-\omega_z)t}(e^{i\omega_p t} + e^{-i\omega_p t}) & -\frac{\Omega_c}{2}e^{i(\omega_2-\omega_y)t}(e^{i\omega_c t} + e^{-i\omega_c t}) & \omega_e \end{bmatrix} \tag{A.6}$$

where the electric field and dipole moments are replaced with the Rabi frequency, $\Omega_{ij} = \frac{E_{ij}\mu_{ij}}{\hbar}$. The second term of equation A.1 is

$$i\hbar U\frac{\partial U^{\dagger}}{\partial t} = \begin{bmatrix} -\hbar\omega_x & 0 & 0 \\ 0 & -\hbar\omega_y & 0 \\ 0 & 0 & -\hbar\omega_z \end{bmatrix} \tag{A.7}$$

Adding equations A.7 and A.6 gives

$$H_{transform} = \hbar\begin{bmatrix} \omega_1 - \omega_x & 0 & -\frac{\Omega_p}{2}e^{i(\omega_z-\omega_x)t}\left(e^{i\omega_p t} + e^{-i\omega_p t}\right) \\ 0 & \omega_2 - \omega_y & -\frac{\Omega_c}{2}e^{i(\omega_z-\omega_y)t}\left(e^{i\omega_c t} + e^{-i\omega_c t}\right) \\ -\frac{\Omega_p}{2}e^{i(\omega_x-\omega_z)t}\left(e^{i\omega_p t} + e^{-i\omega_p t}\right) & -\frac{\Omega_c}{2}e^{i(\omega_y-\omega_z)t}\left(e^{i\omega_c t} + e^{-i\omega_c t}\right) & \omega_e - \omega_z \end{bmatrix} \tag{A.8}$$

The three phases we picked in the unitary matrix are arbitrary and can be selected to simplify equation A.8. We make the following changes to simplify the Hamiltonian.

$$\omega_x = \omega_1$$

$$\omega_y = \omega_2 - \delta\omega$$

$$\omega_z = \omega_2 - \Delta\omega_p$$

where $\delta\omega = (\omega_2 - \omega_1) - (\omega_p - \omega_c)$ and $\Delta\omega_p = (\omega_3 - \omega_1) - \omega_p$. Substituting these into equation A.8 simplifies the exponential terms.

$$e^{i(\omega_x-\omega_z)t} = e^{i(\omega_p)t}$$

$$e^{i(\omega_y-\omega_z)t} = -e^{i(\omega_c)t}$$

With these exponentials written in terms of the probe and coupling frequencies, $H_{transform}$ now equals

$$\hbar \begin{bmatrix} 0 & 0 & -\frac{\Omega_p}{2}e^{i\omega_p t}(e^{i\omega_p t}+e^{-i\omega_p t}) \\ 0 & \delta\omega & -\frac{\Omega_c}{2}e^{i\omega_c t}(e^{i\omega_c t}+e^{-i\omega_c t}) \\ -\frac{\Omega_p}{2}e^{i\omega_p t}(e^{i\omega_p t}+e^{-i\omega_p t}) & -\frac{\Omega_c}{2}e^{i\omega_c t}(e^{i\omega_c t}+e^{-i\omega_c t}) & \Delta\omega_p \end{bmatrix} \tag{A.9}$$

$$\hbar \begin{bmatrix} 0 & 0 & -\frac{\Omega_p}{2}(e^{2i\omega_p t}+1) \\ 0 & \delta\omega & -\frac{\Omega_c}{2}(e^{2i\omega_c t}+1) \\ -\frac{\Omega_p}{2}(e^{-2i\omega_p t}+1) & -\frac{\Omega_c}{2}(e^{-2i\omega_c t}+1) & \Delta\omega_p \end{bmatrix} \tag{A.10}$$

Now we use the rotating wave approximation to get rid of the last oscillating terms. Since $2\omega_c$ and $2\omega_p$ oscillate much faster than the other terms in the equation, they average out over longer time scales. In this work the frequencies of each laser are around 380 THz while the detuning $\delta\omega$ and $\Delta\omega_p$ are on the MHz level. This they oscillate so quickly we can equate them to 1 which leaves us with the Hamiltonian in equation 3.13

$$H_{transform} = \hbar \begin{bmatrix} 0 & 0 & -\frac{\Omega_p}{2} \\ 0 & \delta\omega & -\frac{\Omega_c}{2} \\ -\frac{\Omega_p}{2} & -\frac{\Omega_c}{2} & \Delta\omega_p \end{bmatrix} \tag{A.11}$$

This Hamiltonian is much simpler to numerically integrate and was used for the simulations in this thesis. We put this Hamiltonian in the Liouville equation

$$\frac{\partial\rho}{\partial t} = \frac{1}{i\hbar}[H,\rho] \tag{A.12}$$

to solver for the density matrix components. So far I've ignored the decay rate, Γ_e, from the excited state. We can add it to equation A.11 after the performing the Hamiltonian transformation. The final Hamiltonian becomes

$$H_{transform} = \hbar \begin{bmatrix} 0 & 0 & -\frac{\Omega_p}{2} \\ 0 & \delta\omega & -\frac{\Omega_c}{2} \\ -\frac{\Omega_p}{2} & -\frac{\Omega_c}{2} & \Delta\omega_p - i\frac{\Gamma_e}{2} \end{bmatrix} \tag{A.13}$$

This will give us the correct off diagonal density matrix elements that were not experimentally measured. The above Hamiltonian assumes that decay occurs, but does not tell us that the population decays back into the lower two levels. I add this into the density matrix during the simulation. By adding values to the lower to states equal to that which decays from the excited state, I can be assured that the total population is always equal to 1 (*i.e.* no atoms are lost in the simulation and the total number of atoms is conserved).

Appendix B: Energy Diagram for ^{87}Rb

The relevant energy levels we use for the data in this thesis are the D_2 and D_1 lines in ^{87}Rb. The ground state has the one valence electron in the 5s level. At this point the electron has S=1/2 and L= 0, making J=1/2. We denote this state as $5^2S_{1/2}$. The first excited state corresponds to the electron being excited into the 5p level. The electron spin S can couple to the angular momentum L to create J=1/2 or J=3/2. These two configurations are called the D_1 ($5^2P_{1/2}$) and D_2 ($5^2P_{1/2}$) lines.

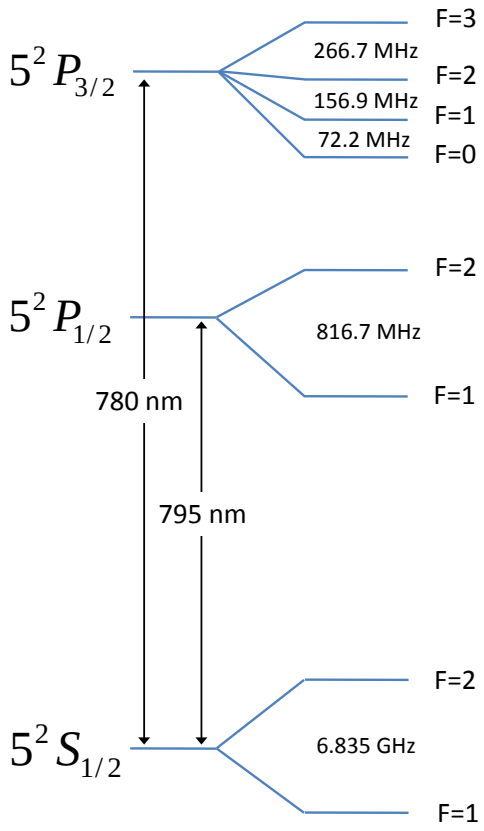

Figure B.1 Energy level diagram of the ^{87}Rb D_1 and D_2 lines. Each hyperfine level can be split into 2F+1 levels by a magnetic field. The hyperfine splitting between the ground state levels is much larger than the excited levels.

Appendix C: Fluorescence Measurement

Fig. C.1 depicts the energy diagram used in the fluorescence measurement for imaging the atoms. We use the cycling transition in the D_2 line to image the atoms. On resonant light is absorbed by the F=2 atoms and then spontaneously decays back to F=2, emitting light in all directions. A 2 inch diameter, 20 cm focal length, doublet lens images the a portion of this light onto an Andor Camera. Atoms in F=1 need to be pumped into F=2 before being imaged. We first pump the F=1 atoms into F=2 using an additional laser. After pumping for $\sim 100\mu$s (plenty of time considering the 25 ns decay rate) the imaging beam is turned on along with the camera, thus imaging the total number of atoms.

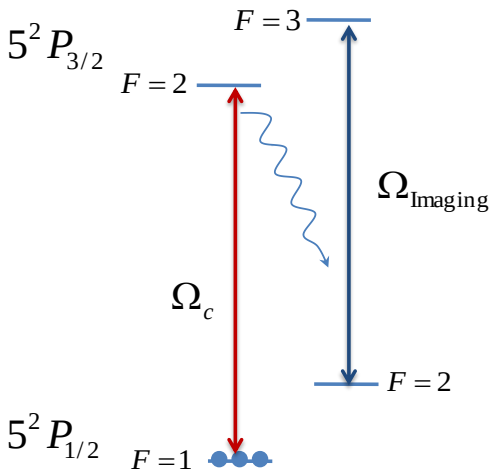

Figure C.1 Atoms in the F=1 ground state are pumped into F=2 before being fluoresced by a laser on resonant to the F=2→F′=3 cycling transition.

The imaging beam heats the atoms, while the atom continually absorbs and emits photons. The atoms eventually becomes so heated, that it leaves the viewing area of the camera. We can remedy this by using retro-reflected beams for the imaging. For our work in the D_2 line, we used the MOT beams as the imaging beam by shifting them on resonance to the F=2→F′=3 transition. This works well because the atom is effectively being heated in all 3 directions, and that way stays in the

camera viewing area for a longer amount of time. We would image for around 1 ms. One problem with this for our experimental set-up was that our MOT beams were very large and increased the background signal on the camera. To get around this we used the blow-away beam as the imaging beam. We used this configuration for our work in the D_1 line. This would heat the atoms in one direction, which reduced the amount of time we could image them from 1 ms to 200 μs. Later we used an additional laser as the imaging beam. This beam was overlapped with itself, creating a standing wave in one direction. This increased the signal, and we could image for around 300 μs. For longer imaging times the atoms would leave the camera viewing area due to heating.

Appendix D: Standing Wave

For some of the data the standing wave was offset from zero. In these cases the minimum coupling beam power coincided with a large amount of transfer to F=2. To do this, we carefully choose the two coupling beam powers to establish a standing with the desired minimum and maximum. Here I will go through the math to determine what laser powers are needed to create a standing wave with the desired minimum and maximum values. The sum of two counter propagating electric fields (in our experiment the two counter propagating coupling beams) is given by

$$E_{total}(x) = E_1 e^{ikx} + E_2 e^{-ikx} \tag{D.1}$$

where E_{total} is the total electric field and $k = 2\pi/\lambda$. It is easier for us to work with intensity to easily compare to the measured power of the lasers. In intensity, the equation becomes,

$$I_{total}(x) = \left| \sqrt{I_1} e^{ikx} + \sqrt{I_2} e^{-ikx} \right|^2 \tag{D.2}$$

The max coupling intensity from equation D.2 is $I_{max} = (\sqrt{I_1} + \sqrt{I_2})^2$ while the minimum is $I_{min} = (\sqrt{I_1} - \sqrt{I_2})^2$. By choosing these two values we solve for I_1 and I_2. Experimentally, we change the intensity by adjusting the laser power. Assuming the sizes of both beams are the same, we can replace all of the intensity terms (I) with power (P) to determine what power each laser needs to be set at. As an example, consider a standing wave that varied from 3 mW to 15 mW. I solve the following matrix equation forP_{min}=3 mW and P_{max}=15 mW.

$$\begin{bmatrix} 1 & -1 \\ 1 & 1 \end{bmatrix} \begin{bmatrix} \sqrt{P_1} \\ \sqrt{P_2} \end{bmatrix} = \begin{bmatrix} \sqrt{P_{min}} \\ \sqrt{P_{max}} \end{bmatrix} \tag{D.3}$$

Solving the above matrix we obtain P_1=7.8541 mW and P_2=1.1459 mW. We don't have the means to measure the laser power to this accuracy due to small power fluctuations through the optical fibers and temperature drifts. I usually try to make it accurate to less than 2% of the calculated values. If the lasers powers each off by $\pm 2\%$, the resulting standing wave would range

from 3.00 ± 0.06 mW to 15.00 $\pm .30$ mW. Although changes in power will affect the standing wave, these changes are small enough to have a large effect on the data. The power drifts slowly over time and remains constant during the EIT pulses. The autocorrelation experiment is performed in a few μs, and none of the fluctuations that cause the small error in power measurement fluctuate at that level. I do not adjust any of the simulations to include for the small drift, since most of the data would require changes more than 10% to see a noticeable effect.

To simulate the standing wave and how the intensity varies with x, $I(x)$, I use the following equation.

$$I_{total}(x) = I_{min} + (I_{max} - I_{min}) \sin^2(kx) \tag{D.4}$$

This accurately depicts the intensity as it varies over x and is equivalent to equation D.2. The peak intensity of a Gaussian beam is related to the power by

$$I = \frac{2P}{\pi\omega^2} \tag{D.5}$$

where ω is the radius of the beam, measured when the intensity drops to $1/e^2$ (13%) of its peak intensity. The factor of 2 comes from the shape of the beam. ω is experimentally measured with a Newport or Thorlabs camera, each giving very similar values. Using power in equation D.4 instead of intensity, and making the beam sizes equal give

$$P_{total}(x) = P_{min} + (P_{max} - P_{min}) \sin^2(kx) \tag{D.6}$$

For the simulations I calculate $P_{total}(x)$ and then use equation D.5 to determine I_x. From the intensity, I can find the electric field for the Rabi frequencies used in the density matrix discussed in section 3.6.

Appendix E: D_1 Line Improvements

E.1 Data Acquisition Improvements

For the standing wave data taken in Chapter 8, we made improvements in how we collected the remaining atoms. In Chapter 6 we averaged over 150 points to get a data point for one value of δf. Then we changed δf and collected data for another 150 points and so no, until we had data for every point of δf. The problem with this method is that long term fluctuations can effect the loading of the FORT atoms. As an example, Fig. E.1 shows 3000 data points of the FORT with no EIT beams. Each data point took about 1 second to take, so the data was taken over $\sim$ 50 minutes. The FORT parameters are the same for each data point, and ideally we would get the same number of atoms trapped in the FORT. The camera signal (and therefore number of trapped atoms) shows variations of up to 30% from the average value of the data. The FORT loading also varied on longer time scales of 10's of minutes.

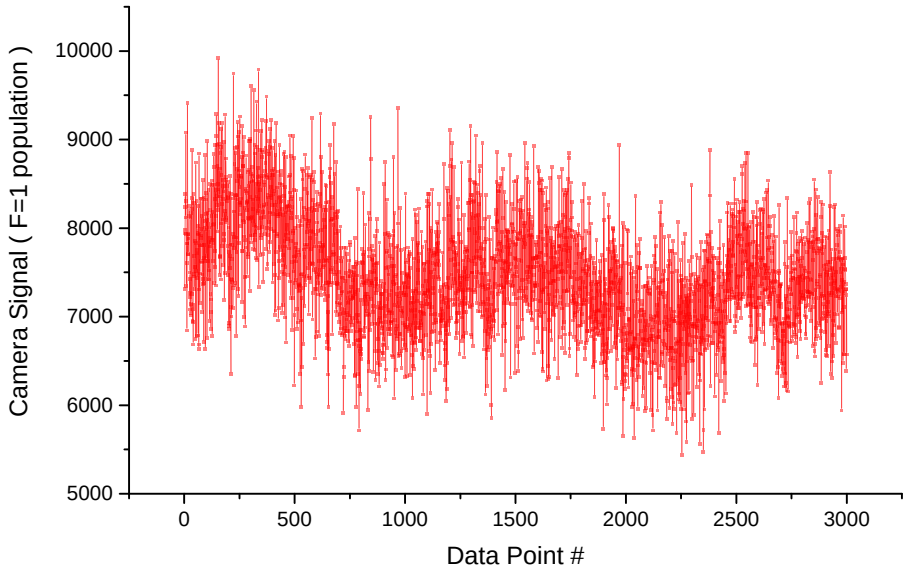

Figure E.1 Camera signal from 3000 fort loadings, performed over a period of about 50 minutes. No EIT beams were on for this data.

Fig. E.2 shows the average data using the previously described technique. The averaged data fluctuates up to 20% between the min and max values. Experimentally, we need to be able to detect contrast to about 2-3% to be confident with our results. To fix this issue we periodically take points for different data sets. Fig. E.3 shows data using this technique, where the average camera signal for averaged data point 1 has 150 data points, but were taken at different times during the 3000 data acquisition sequence. This gets rid of the larger oscillations that can occur during the FORT loading. In this data the max and min point differ by only 2%.

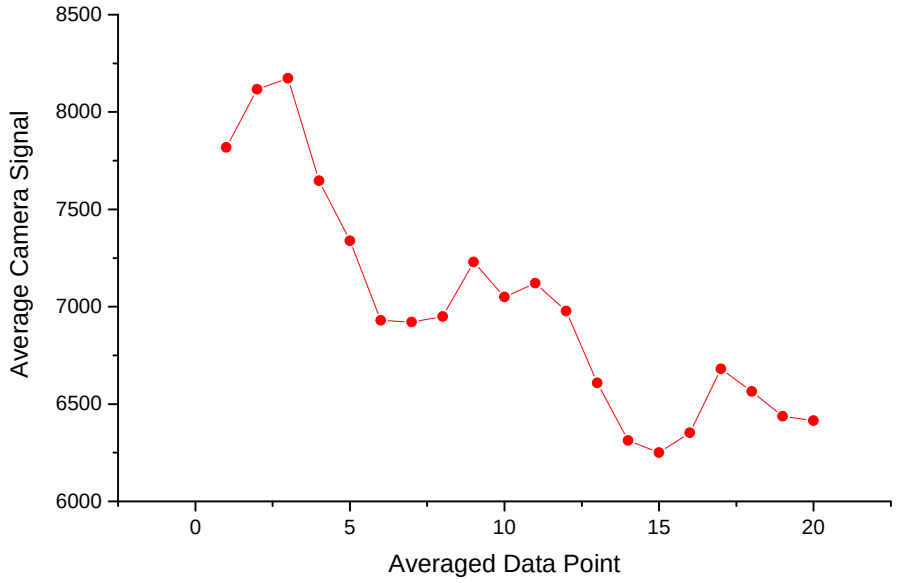

Figure E.2 The average signal plotted against Averaged Data Point 1 is th average of the first 150 data points in Fig. E.1. The second point is the average of data points 151 to 300, and so on.

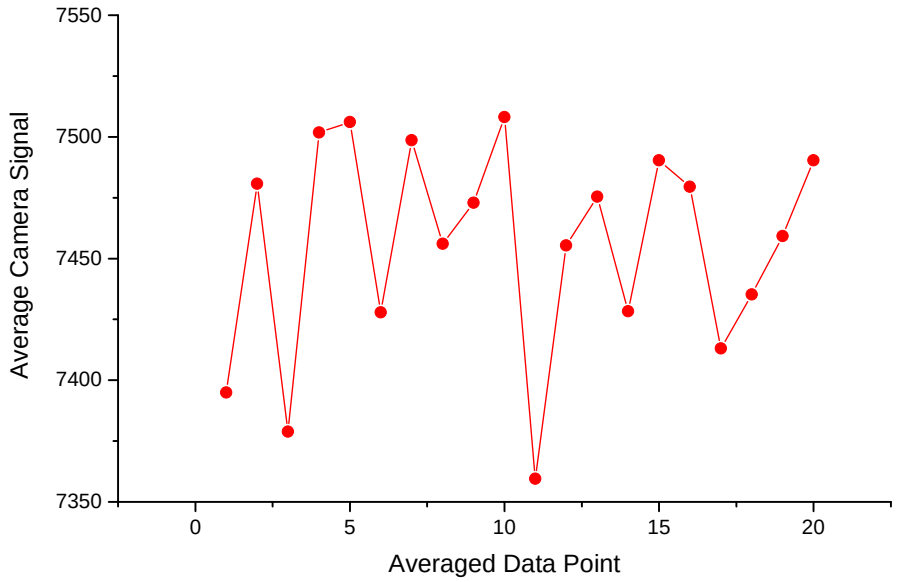

Figure E.3 Average by taking every 20^{th} point from Fig. E.1 and averaging them together. This gets rid of the longer time scale oscillations.

Appendix F: FPGATimings

F.1 General information on switching lasers on and off

All of the laser switching was done through RF switches with a TTL pulse synced with a national instruments field-programmable gate array (FPGA). Our FPGA provided accurate switch times to a 1 μs with a jitter around 10 ns. For faster switching we used an 8 channel delay generator with nanosecond resolution and femtosecond jitter. The delay generator switched the 100 ns EIT pulses and the blow away beam pulses. These timings needed to be the most accurate so that the pulses were correctly overlapped. A TTL pulse from the FPGA triggered the delay generator. After an EIT pulse took place, the camera would image remaining atoms in the FORT. A Matlab program using Andor software would record the camera image every time the FPGA triggered the camera. Since the camera only took a picture about every second, the program could easily record the data.

The probe and coupling beam pulse widths had to be measured on an oscilloscope, and the timings displayed on the delay generator were not always accurate in relationship to the measured pulse width. Alignment to the AOMs greatly effected the pulse width and could add delay to the pulses. The beams needed to be focused to about the same size through the AOMs to get the same rise times. Although the limit of the AOMs were rise times of ¡10 ns, the spot sizes we used would get to rise times of about 20 ns. Because of the sensitivity of the pulses to the AOMs, when these AOMs were re aligned the timings would be need to be re-checked.

For the D_1 experiment we increased the rise times to about 50 ns, by doubling the size of the beam through each of the AOMs. Although it worked, we suffered in efficiency and had less power through the fibers.

F.2 Experimental Procedure for Autocorrelation Experiment

Here I'll go through some of the standard techniques and timings to that we went through for the experiment. Fig. F.1 and F.2 show the timings of the procedure. The pulses in Fig. F.1 were

all done with the FPGA since their resolution wasn't as critical as the EIT beams. The 8 pulses in Fig. F.2 were each created from a separate channel from the delay generator. This allowed very accurate timing of each pulse.

1. MOT beams, MOT repumper and Anti Helmholtz coil magnetic field are turned ON. A shutter in front of the camera is also turned on to block the relatively bright light from the MOT from saturating the camera sensor.

2. MOT is switched to CMOT while repumper is simultaneously reduced in power. At this time the FORT beam is turned on, and stays at high power during the $\sim$ 40 ms loading process.

3. CMOT beams, repumper beam, and Anti Helmholtz coil magnetic field are turned OFF. Beam block is turned on to prevent any ASE from MOT tapered amplifier from heating FORT atoms.

4. FORT power is slowly reduced by an RF attenuation circuit using an arbitrary waveform generator (AWG).

5. Magnetic field is turned on to raise the degeneracy of the m levels.

6. Atoms are pumped from m=$\pm$1 to m=0 with a laser resonant between F=1 to F=2. The coupling laser that resonants between F=2 and F=2 is also turned on. The net effect is that most of the atoms are pumped to the F=1 m=0 level.

7. The blow-away beam is turned on to get rid of any remaining atoms in F=2. The number is very small the previous step, but this assures that the atoms we use for the autocorrelation experiment are only in F=1.

8. FORT beam is switched off, at this point no lasers are on and there are cold F=1 m=0 atoms where the FORT laser was focused

9. Autocorrelation experiment is performed with standing wave. The timing diagram is shown in Fig. F.2

10. FORT beam is turned on, trapping any cold atoms remaining.

11. Atoms are imaged by turning on the repumper and imaging laser with the ECCD camera. The imaging is done ∼30 ms after the FORT re-traps the atoms to make sure any heated atoms are away from the focus of the camera.

Some of these steps may have been in omitted during certain stages of the experiment discussed in the paper. For example, we did not always pump atoms into the m=0 level.

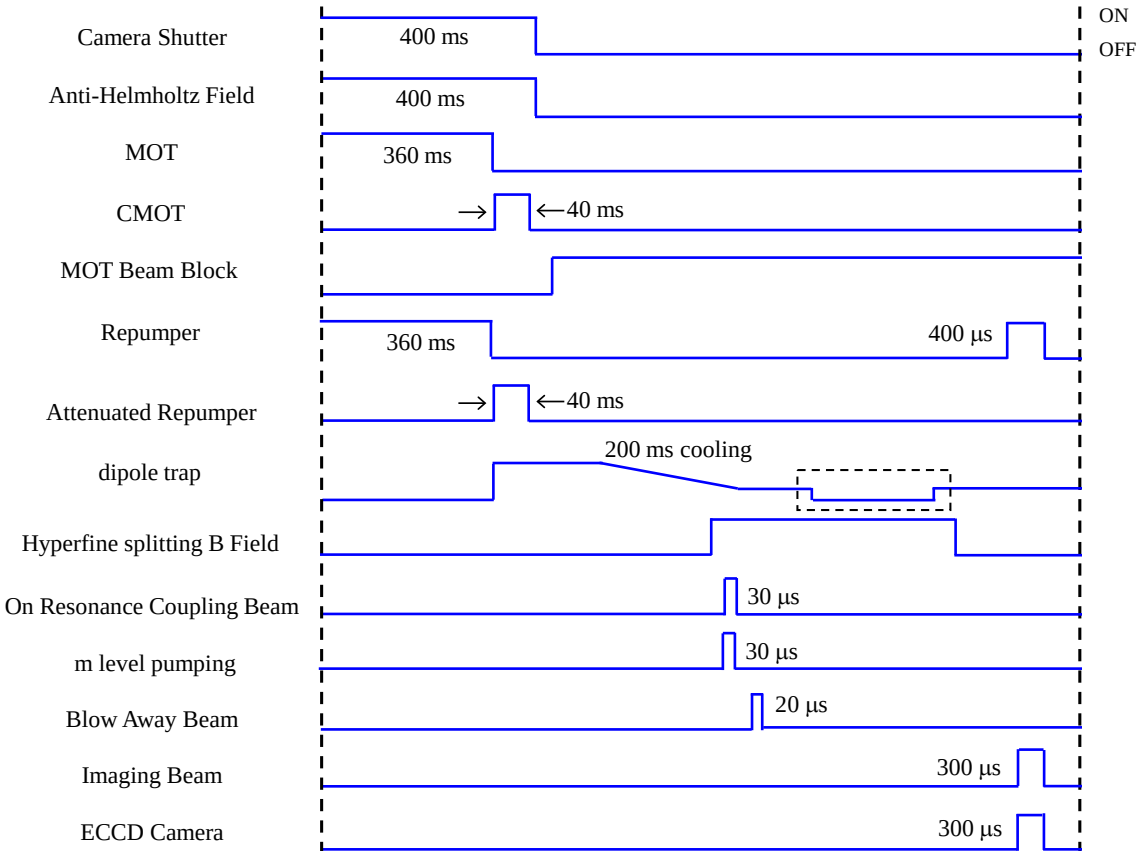

Figure F.1 Diagram for the FPGA timings for the On resonance data in chapter **??**. The diagram is not to scale, but shows when things are turned on and off relative to each other. The EIT pulses sequences are done within the dotted box when the dipole trap laser is off. These timings are in Fig. F.2.

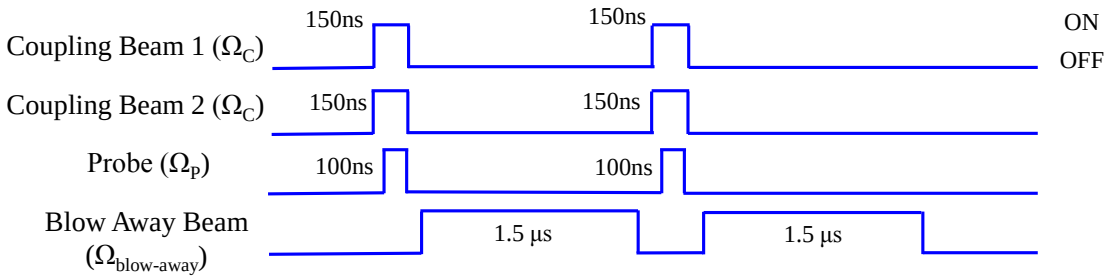

Figure F.2 Diagram for the EIT puse sequence timings done with the delay generator. These are done when the dipole trap laser is off.

All of the atoms were initialized to F=1 before turning on the probe and coupling beams. One of the coupling beams is switched to be on resonance with the excited F=2 state and turned on for approximately 20 μs at very low power to pump atoms in F=1. If the power was too high, a few milliwatts, atoms would not be fully pumped to F=1 and a large portion would be left in F=2. At higher intensities, rabi flopping move the atoms between F=2 and F′=2, and are not given a chance to decay into F=1.

F.3 Probe and Coupling Beam Alignment

Although we can be fairly certain that the coupling beams are well overlapped by passing one through the other's fiber, we roughly align the coupling beam to the FORT using a standard Newport mirror mount. We turn a 1/4 100 screw to align to the FORT atoms in the x and y direction. Considering the beam travels over a meter after the last mirror in the alignment set up, any small change in angle on the mirror greatly changes the position on small scales. For the mounts we used, 1.75 inches between the screw and pivot point, an eighth of a turn moved the beam 0.36 mm, on order of the $1/e^2$ radius of the beam, 0.6 mm. The probe beam was larger, with a radius of 1.1 mm, and would have been less affected by the sensitivity.

Appendix G: D_1 Line Experiment Issues

G.1 ASE from M2K laser

The M2K lasers would produce a large amount of ASE when not seeded. The 2 Watt amplifier would output ∼400 mW of power when unseeded and 1.5 W with a seed laser. Once seeded, the ASE by a factor of 10. We could check the amount of ASE before and after seeding using a spectrum analyzer. If the seeding to the TA was poor, a majority

G.2 m level pumping

To selectively pump the m=$\pm$1 levels, the electric field of the pump laser must be perpendicular to applied magnetic field. The power was of the pump laser was very low, around 20 μW, with a beam size of approximately 1 mm. It was on for 20 μs. It's fixed to the F=1 F′=1 transition and prohibits excitation from m_F=0 to m'_F=1 because of its orientation to the magnetic field. After being pumped to F′=1 , the atoms will decay to any of the F=1 or F=2 levels, as shown in Fig. G.2. Some of the atoms will decay to F=1 m_F=0, where we want the atoms to end up, but other will decay to F=2 m levels. We pump these with the coupling beam on resonant with the F=2 to F=2 transition. This laser pumps any atoms that are in the F=2 level back to F=1. While both beams are on, the atoms in F=1 m_F=0 are not affected by either electric field, and we end up with many of the atoms in the F=1 m_F=0 level.

After m level pumping, we can get a rough idea of how well the pumping worked by looking for transfer via EIT at different coupling frequencies. By splitting the m levels with an external magnetic field, the two photon detuning ($\delta\omega$) should change. Fig. G.2 shows an enhancement at $\delta\omega$=0 when the pumping beam is turned on. If there is no pumping beam, there is transfer due to EIT at $\delta\omega$=6 MHz via the m_F=-1 level. If we leave the pump beam on longer, it begin to pump out the m=0 level, leaving less atoms in the FORT. Even a small component of the pumping electric field not parallel to the magnetic field will excite the F=1 m=0 atoms into the F=2 level, so

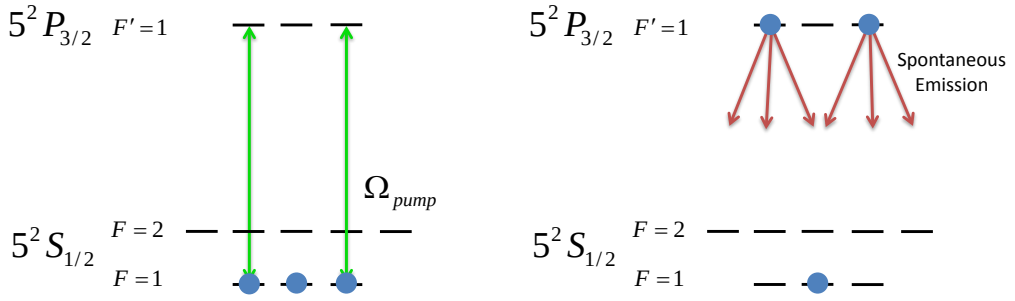

Figure G.1 M level pumping by linearly polarized light. The F=1 m_F=0 to F′=1 m_F=0 is a forbidden transition. After pumping the excited atoms can decay to either of the F=2 or F=1 ground state levels.

this result is not surprising for our set up. The signal decreases to due to heating from repeatedly pumping atoms between states.

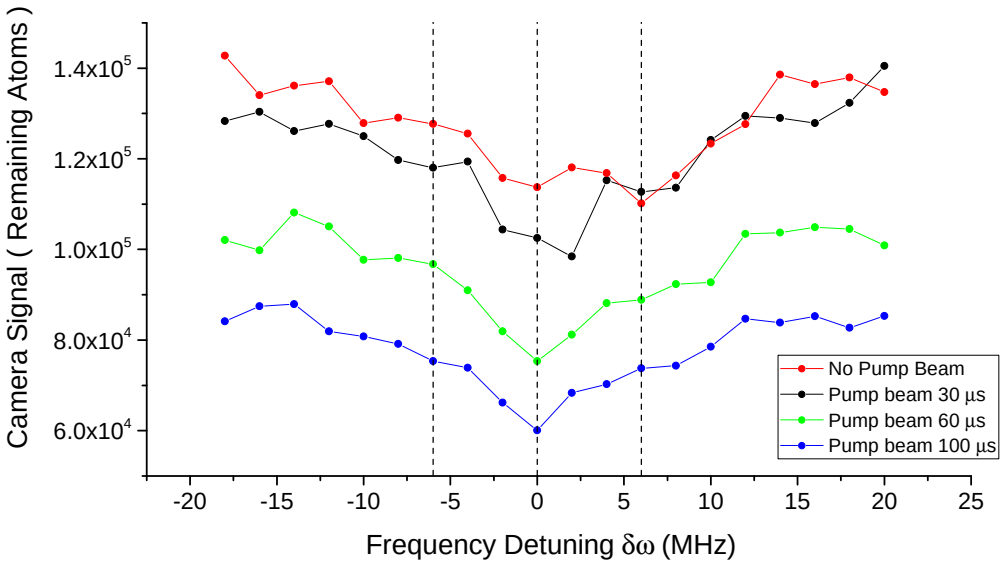

Figure G.2 M level pumping by 20 μW off linearly polarized light for different pulse times. The 3 dotted lines represent what detuning should result in transfer from EIT, relative to m_F=0. m=-1 at 6 MHz. m_F=1 at -6 MHz. We saw very little evidence of population at m_F=1. With the pump beam on, we saw a larger effect at $\delta\omega$=0, indicating that a larger portion of the atoms were in the m=0 level. Leaving the pump beam on too long resulted in reduced atomic population.

G.3 Shift from δx=0

An odd feature that would sometimes occur was an shift from 0 MHz for the standing wave. The peak signal in the autocorrelation data would be slightly off from zero when the standing was traveling in a certain direction. The simulations predict that the peak signal should occur at δf=0 and decrease to the same value at δf=$\pm$50 kHz. The two auto correlation data sets in figure G.3 show patterns with similar feature sizes but offset from 0 kHz. The only experimental difference between the two was which coupling beam was changed to create δf. In either case, the standing wave was moving in the same direction relative to other lasers used in the experiment (*i.e.* the wave was traveling toward the source of the probe beam). This shift would come up if the data was not taken at the center of the FORT, and seemed to go away when the FORT was optimized. We considered recoil energy from the probe to be the problem. Each atom absorbs a photon to transfer energy levels, until it reaches the dark state. Since the probe beam is in the direction parallel to the coupling beams, this could have a preferential effect depending the direction the standing wave is moving. We performed the experiment with the probe beam parallel to the coupling beam but could still see this shift.

G.4 On Resonant D_1 Line Improvements

G.4.1 FORT Laser

We made a few changes to take the experiment for the on resonance data. The DPSS 1064 nm diople trap laser was replaced with a 2 Watt 1064 nm TA. We could get about 150 μW of power out of a single mode fiber from this new set up to produce a FORT. Although the laser was much weaker, we could focus it to a smaller spot size, and achieve similar intensities. We found that the intensity was more consistent than the DPSS laser. This laser trapped a similar number of atoms at the same temperature as the DPSS laser system. It was also easier to use because it did not require a large water chiller.

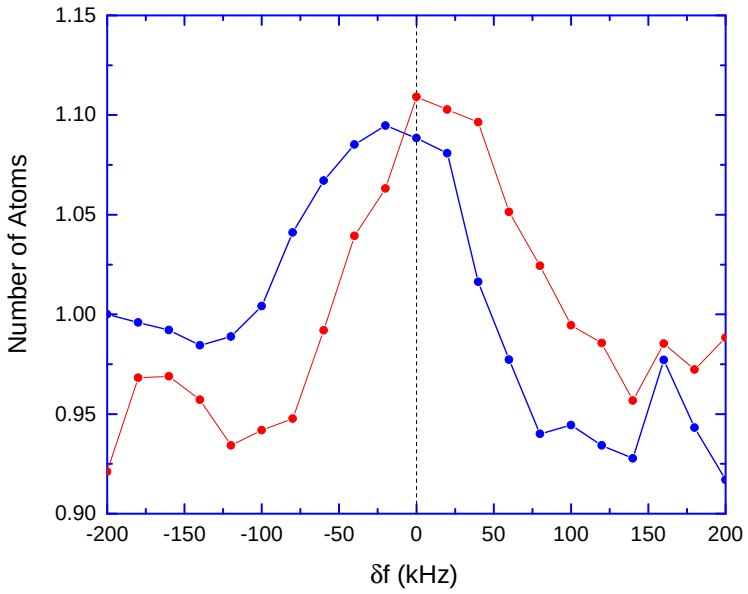

Figure G.3 Correlation data plotted over δf. The frequency difference is between the shifted beam and the unshifted beam. For either set of data, the standing wave is moving toward the probe beam.

G.4.2 Data Acquisition

We tried to further improve our data acquisition with a physical shutter in front of the CCD camera. The camera was very sensitive to any incident light, even when the detector was off. During the MOT loading stage, the MOT fluorescence can be very bright, and this would saturate the camera detector. When we looked at the fluorescence from the FORT atoms (about 300 ms after the MOT is turned off) there were still remnants of the strong MOT fluorescence visible on the camera. To prevent this, we added a shutter in front of the camera. While the MOT was being formed, the shutter was closed, preventing any of the MOT fluorescence from reaching the camera.

We also increased the Fluorescence signal from the FORT atoms by adding an additional laser we called the "imaging beam". This is on resonance with cycling transition in the D_2 line. We overlap it with itself to create a standing wave that is overlapped with the FORT atoms. The atoms

are heated in both directions, and thus the atoms stay in the camera viewing area for longer. We increase the FORT signal with this additional laser.

Appendix H: Convultion Details

Here I will go through the convolution measurement in more detail. The steps are

1. Simulate remaining population in F=1 after 1 EIT pulse sequence
2. Simulate the spread of atoms due to temperature of the atoms
3. Take the convolution of step 1 and step 2
4. Convolute the convolution of step 3 with step 1
5. This resulting Convolution is compared to the experimentally taken autocorrelation data

H.1 Transfer for 1 EIT pulse sequence

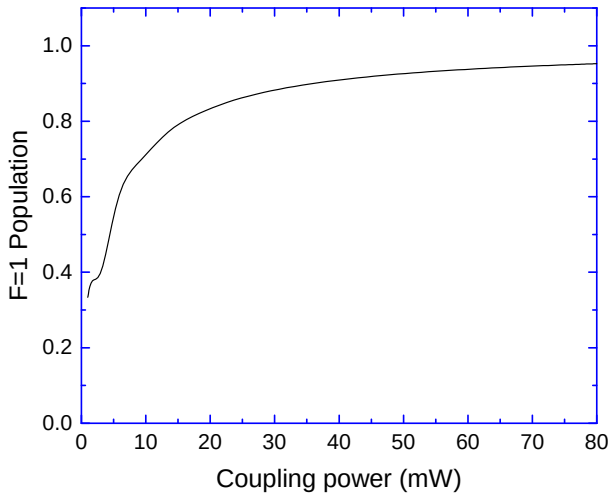

Figure H.1 Simulated population in F=1 after 1 EIT pulse sequence

I will use the example for the 1 to 80 mW standing wave case discussed in section 8.3 since it most closely followed the solution of the dark state. Fig. H.1 is the population of F=1 from 1 mW to 80 mW for the on resonance parameters discussed in section 8.3 after 1 EIT pulse sequence.

The data is directly used to find the population in F=2 at points along the standing wave. Fig. H.2 shows the simulated standing with a period of 397.5 nm (half the wavelength of the coupling laser) ranging from 1 mW to 80 mW. Also plotted is the population of F=1 at each location of the standing wave. We used the population in F=1 to perform the convolution because it represents what is done experimentally. We get rid of any F=2 atoms, and are a left with a fraction of the total atoms after 1 EIT pulse sequence.

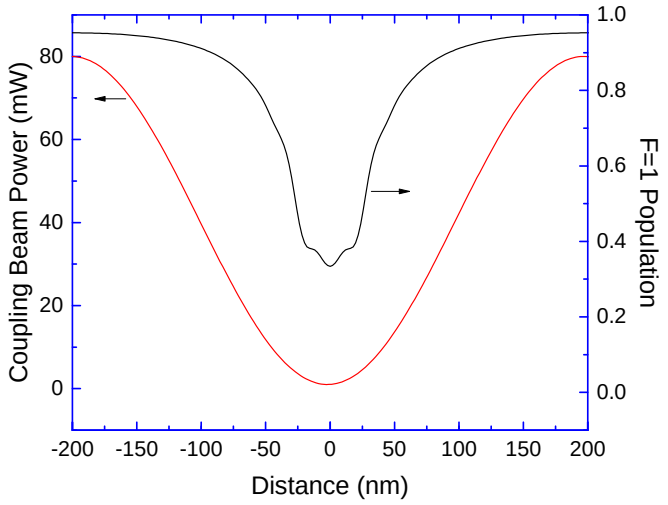

Figure H.2 The red line is the power of coupling beam across the standing wave for once period. The black line is the simulated population in F=1 for different locations in the standing wave.

H.2 Atomic Velocity

The TOF measurements I showed earlier found the mean velocity of the atoms assuming a Maxwell-Boltzmann distribution. The velocity was measured in only one direction of the FORT, and assumed to be the same for all three dimensions. The velocity distribution in one direction for a Maxwell-Boltzmann distribution is defined as

$$f(v_x) = \left(\frac{m}{2\pi k_b T}\right)^{1/2} exp\left[\frac{m v_x^2}{2kT}\right] \tag{H.1}$$

where the most probably velocity is

$$v_p = \sqrt{\frac{2k_bT}{m}} \tag{H.2}$$

We used v_p=12 nm/μs for the D_1 line simulations, slightly lower than the measured value of v_p=17 nm/μs, that measurement was an upper bound of the temperature. The atoms travel for 1.6 μs, and we can convert the velocity distribution into a position distribution. Substituting in the most probably velocity, we get

$$f(x) = \left(\frac{1}{\pi v_p}\right)^{1/2} exp\left[\frac{-x^2}{v_p^2\tau^2}\right] \tag{H.3}$$

where τ is the time between EIT pulses.

H.3 Convolutions

The transfer data in Fig. H.2 is convoluted with the distribution position in equation H.3 to simulate the motion of the atoms after the first EIT pulse sequence, but before the second EIT pulse sequence.

The convolution equation for discrete values is

$$(f * g)(x) = \sum_{-\lambda/2}^{\lambda/2} f(x')g(x - x')\delta x' \tag{H.4}$$

where in our case g(x) is the population in F=1 plotted in Fig. H.2. We perform the convolution over 1 standing wave period to simulate the experiment. The convolution is periodic, which simulates the actual experiment. In the FORT, the standing wave oscillates multiple times, creating multiple features. The resulting convolution is plotted in Fig. H.3.

We plot it along the same distance, and see that the original features is slightly broadened due to the atomic temperature, as expected. This data is then convoluted with the original transfer data in Fig. H.2to simulate the effect the second EIT pulse. Using the convolution again, we get

$$(g * (f * g))(x) = \sum_{-\lambda/2}^{\lambda/2} (f * g)(x')g(x - x')\delta x' \tag{H.5}$$

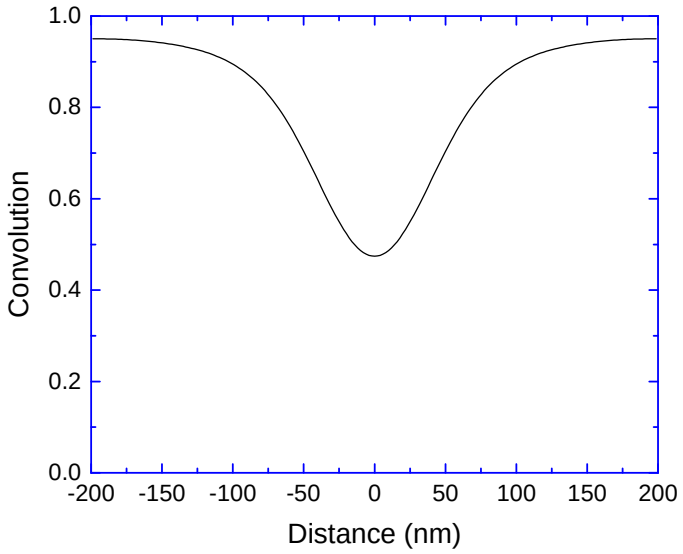

Figure H.3 The convolution of the population in F=1 after 1 EIT pulse sequence with the standing wave convoluted with the Maxwell Boltzmann distribution from equation H.3

Fig. H.4 shows the final convolution this plot is compared to the autocorrelation data. Since the two plots are similar, we deduce that the original function g(x) accurately represents what happens during one EIT pulse sequence.

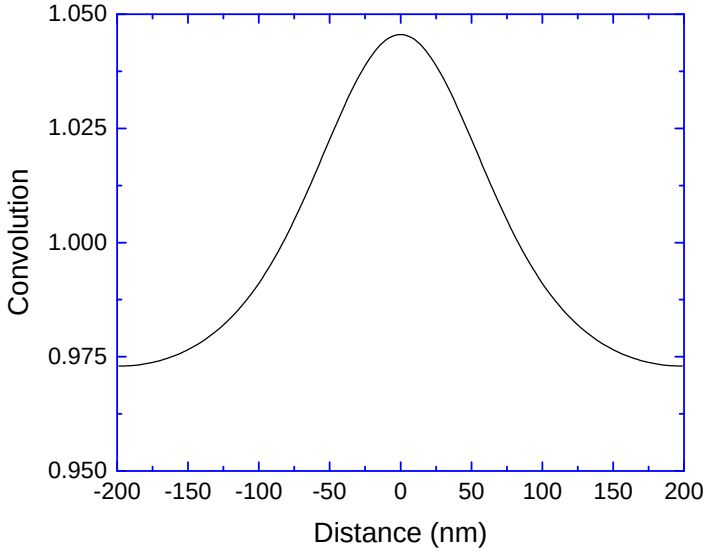

Figure H.4 The convolution of the data in Fig. H.3 with the transfer of one EIT pulse. This should be same as the experimentally taken autocorrelation data.

Appendix I: EIT Comments

I.1 Changes in Intenisty

When EIT occurs probe photons are used to transfer population until it reaches steady state. If a large amount of photons are absorbed before reaching the dark state, the final intensity would be different than the initial intensity. We use laser powers that contain many more photons than number of FORT atoms. Because of this, the small change in intensity is negligible, and the final and initial intensities are equal.

I.2 Polarization

The polarization of the two EIT pulses detemine what excited level EIT is performed through. We consistently used 2 linearly polarized lasers that were orthogonal to one another as our coupling and probe beam. We set the quantization axis parrallel to the dipole trap laser, in the z direction of figur

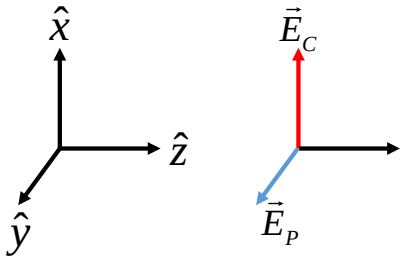

Figure I.1 Electric field of coupling and probe beam used in the experiments

The polarization of the light determines what m levels of the hyperfine levels are coupled between excited states. An electrif field can impose a $\Delta m_F = 0$ for and electric field oscillating along z, and $\Delta m_F = \pm 1$ for an electric field oscillating perpendicular to z. Cicular polarized light is defined as

$$\sigma_+ = \frac{E_x + iE_y}{\sqrt{2}} \tag{I.1}$$

$$\sigma_- = \frac{E_x - iE_y}{\sqrt{2}} \tag{I.2}$$

where the quantization axis is in the z direction. Since both lasers are perpendicular, the set up only induces $\Delta m_F = \pm 1$ changes in the atomic system.